Journal of Computational Physics 314 (2016) 824–862

Contents lists available at ScienceDirect

Journal of Computational Physics

www.elsevier.com/locate/jcp

High order ADER schemes for a unified first order hyperbolic formulation of continuum mechanics: Viscous heat-conducting fluids and elastic solids

Michael Dumbser [a,*], Ilya Peshkov [b,1], Evgeniy Romenski [c,d], Olindo Zanotti [a]

[a] Department of Civil, Environmental and Mechanical Engineering, University of Trento, Via Mesiano 77, 38123 Trento, Italy
[b] Open and Experimental Center for Heavy Oil, Université de Pau et des Pays de l'Adour, Avenue de l'Université, 64012 Pau, France
[c] Sobolev Institute of Mathematics, 4 Acad. Koptyug Avenue, 630090 Novosibirsk, Russia
[d] Novosibirsk State University, 2 Pirogova Str., 630090 Novosibirsk, Russia

ARTICLE INFO

Article history:
Received 27 November 2015
Received in revised form 1 February 2016
Accepted 3 February 2016
Available online 8 February 2016

Keywords:
ADER–WENO finite volume schemes
Arbitrary high-order discontinuous Galerkin schemes
Path-conservative methods and stiff source terms
Unified first order hyperbolic formulation of nonlinear continuum mechanics
Fluid mechanics and solid mechanics
Viscous compressible fluids and elastic solids

ABSTRACT

This paper is concerned with the numerical solution of the *unified* first order hyperbolic formulation of continuum mechanics recently proposed by Peshkov and Romenski [110], further denoted as *HPR model*. In that framework, the viscous stresses are computed from the so-called *distortion tensor* $\boldsymbol{A}$, which is one of the primary state variables in the proposed first order system. A very important key feature of the HPR model is its ability to describe *at the same time* the behavior of inviscid and viscous compressible Newtonian and non-Newtonian *fluids* with heat conduction, as well as the behavior of elastic and visco-plastic *solids*. Actually, the model treats viscous and inviscid fluids as generalized visco-plastic solids. This is achieved via a stiff source term that accounts for strain relaxation in the evolution equations of $\boldsymbol{A}$. Also heat conduction is included via a first order hyperbolic system for the thermal impulse, from which the heat flux is computed. The governing PDE system is hyperbolic and fully consistent with the first and the second principle of thermodynamics. It is also fundamentally *different* from first order Maxwell–Cattaneo-type relaxation models based on extended irreversible thermodynamics. The HPR model represents therefore a *novel* and *unified* description of continuum mechanics, which applies at the same time to *fluid mechanics* and *solid mechanics*. In this paper, the direct connection between the HPR model and the classical hyperbolic–parabolic Navier–Stokes–Fourier theory is established for the first time via a formal asymptotic analysis in the stiff relaxation limit.

From a numerical point of view, the governing partial differential equations are very challenging, since they form a large nonlinear hyperbolic PDE system that includes stiff source terms and non-conservative products. We apply the successful family of one-step ADER–WENO finite volume (FV) and ADER discontinuous Galerkin (DG) finite element schemes to the HPR model in the stiff relaxation limit, and compare the numerical results with exact or numerical reference solutions obtained for the Euler and Navier–Stokes equations. Numerical convergence results are also provided. To show the universality of the HPR model, the paper is rounded-off with an application to wave propagation in elastic solids, for which one only needs to switch off the strain relaxation source term in the governing PDE system.

* Corresponding author.
E-mail addresses: michael.dumbser@unitn.it (M. Dumbser), peshkov@math.nsc.ru (I. Peshkov), evrom@math.nsc.ru (E. Romenski), olindo.zanotti@unitn.it (O. Zanotti).

[1] Ilya Peshkov is on leave from Sobolev Institute of Mathematics, 4 Acad. Koptyug Avenue, 630090 Novosibirsk, Russia.

http://dx.doi.org/10.1016/j.jcp.2016.02.015

We provide various examples showing that for the purpose of *flow visualization*, the distortion tensor $\boldsymbol{A}$ seems to be particularly useful.

1. Introduction

1.1. A unified first order hyperbolic approach to continuum mechanics

An attempt to build a unified formulation of continuum mechanics in first order hyperbolic form that includes fluid mechanics as well as solid mechanics has been very recently described by Peshkov and Romenski in [110]. The proposed model, hereafter the Hyperbolic Peshkov–Romenski (HPR) model, can potentially cover the entire spectrum of viscous flows ranging from non-equilibrium gas dynamics to Newtonian and non-Newtonian fluids, and even elastic and plastic deformation in solids, provided that the continuum description is applicable. In order to make this possible, the *material element*[2] view point is employed and the very essence of any macroscopic flow, *i.e.* the process of material element rearrangements, is explicitly described in the mathematical model. We note that the term *material element* should be understood in the conventional meaning of continuum mechanics, *i.e.* as an *ensemble* of a *sufficiently large number* of molecules or atoms.

An important difference between the HPR model and the classical continuum models is that the material elements not only have a finite size, but they also have an internal structure, which is subject to rearrangements, and which can be macroscopically described after introducing suitable quantities. Thus, in order to describe the deformability of material elements, a tensorial field[3] $\boldsymbol{A}(\mathbf{x},t)=[A_{ij}]$ is used. It maps the material elements from a current deformed state to the undeformed state, and it contains the information about deformation and rotation of material elements. While this approach is standard in the framework of solid mechanics, it is much less obvious for fluid dynamics. Because of the rearrangements of material elements, the field $\boldsymbol{A}$ is not integrable in the sense that it does not relate Eulerian and Lagrangian coordinates of the continuum. As a result, the field $\boldsymbol{A}$ is *local*, see [110,70,77,78]. This is also the reason why we *cannot* call $\boldsymbol{A}$ the *deformation gradient*, (or more precisely, the inverse deformation gradient), and thus, following [70,77,78], we shall instead refer to it as the *material distortion field*, or simply the *distortion tensor*.

In addition to the distortion field $\boldsymbol{A}$, another important information is required to describe rearrangements in a system of material elements of finite size. This information should characterize how easy or how hard it is for material elements to rearrange (fluidity). In the kinetic theory of liquids, Frenkel [60] proposed to use the average time τ_{F} between two solid-like vibration states of an atom to describe the ability of a liquid to flow.[4] Following this idea of Frenkel, it was proposed in [110] to use a continuum analog τ of Frenkel's time τ_{F}. Thus, in our continuum approach, the time τ is the time taken by a given material element to "escape" from the *cage* composed of its neighbor elements, i.e. the time taken to *rearrange* with one of its neighbors. The more viscous a fluid is, the larger the time τ, *i.e.* the longer the fluid elements stay in contact with each other. The limiting cases, inviscid fluids and elastic solids, are recovered when $\tau=0$ and $\tau=\infty$, respectively, while for viscous fluids, the time τ is finite with $0<\tau<\infty$ (see the discussion in [110]). We shall call τ the *strain dissipation time*, because, in the mathematical formulation of the HPR model the inverse time τ^{-1} defines the rate at which shear strains dissipate during the rearrangement process.

Our material element point of view allows to formulate the system of governing partial differential equations (PDE) with rather convenient mathematical properties:

- First, the model is described by a system of first order PDEs. We recall that first order systems are less sensitive to the quality of the computational mesh and in general they allow to get a numerical scheme of higher order of accuracy than for a second order model on the same discrete stencil.
- Second, the model is *hyperbolic* if the total energy potential is a *convex* function of the state variables, see [110]. In other words, the model is based on a *wave* formulation. Indeed, from the point of view of the physics of wave propagation and because of the causality principle, any macroscopic transport phenomenon should be considered as a wave propagation process. In particular, the momentum transfer in a viscous fluid in the transverse direction to the mean flow is nothing but a wave propagation process. These waves are known as the shear waves, which are very dissipative waves propagating over a distance that equals just a few wave lengths. Nevertheless, such waves give rise to very important phenomena known as boundary layers. Thus, one may expect that a physically based boundary layer theory has to be based on such a transverse wave dynamics. In full agreement with the above discussion, there are two types of waves in our hyperbolic model, *longitudinal waves* and *shear waves*, which transfer momentum in the transverse flow directions.

[2] In fluid mechanics, the terms fluid elements, fluid particles and fluid parcels are also used.

[3] Rigorously speaking, $\boldsymbol{A}$ is not a tensor field of rank 2, since it transforms like a tensor of rank 1 with respect to a change of coordinates.

[4] Frenkel's ideas have been discussed, used and extended during the last 20 years to compute the thermodynamic and dynamic properties of liquids, see [142,30,23,18,19] and references therein.

- Third, the dissipative process of material element rearrangements is modeled by a stiff algebraic source term, *i.e.* this term does not depend on the space derivatives, which automatically implies that the characteristic speeds of the corresponding hyperbolic system are always *finite* (as they should), whatever the time τ is. One may recall that in hyperbolic Maxwell–Cattaneo-type models some characteristic speeds tend to infinity if the relaxation parameter tends to zero.

We also note that the system of the governing equations discussed in [110] has already been derived by Godunov and Romenski in the 1970s [74,70] in the context of elasto-plastic deformation of metals, for which it has been used by several authors over the years [116,64,9,73,7]. On the contrary, the idea that the same model could also describe the dynamics of any continuum, including inviscid fluids, viscous Newtonian and non-Newtonian fluids, elastic and visco-plastic solids was discussed in [110] for the first time. In fact, a very similar idea was proposed by Besseling in [16], but unfortunately it has never been appreciated in the fluid dynamics context. In order to allow a quantitative comparison also with the Fourier heat conduction theory, in this paper we extend the model proposed by Peshkov and Romenski in [110] by including also hyperbolic heat conduction equations, as proposed by Romenski in [96,116,115,114]. The essential difference of our hyperbolic heat conduction model from that proposed by Cattaneo [28] is that the speed of the heat propagation front is always *finite*, whatever the heat flux relaxation parameter is.

We emphasize that it is not our aim to provide a link with kinetic theory, although this could be very illuminating, but rather to verify the capabilities of the HPR model to account for a wide variety of dynamical systems.

1.2. High order ADER–WENO finite volume and ADER discontinuous Galerkin finite element schemes

The resulting governing partial differential equations of the HPR model, introduced in [110] and presented later in Section 2, are rather challenging from a numerical point of view, since they constitute a *large system* of nonlinear hyperbolic conservation laws that also includes *non-conservative products* and *stiff source terms*. To the best knowledge of the authors, the complete first order HPR model presented in [110] has never been solved so far by any numerical method in multiple space dimensions and including all terms, hence one of the main goals of this paper is to thoroughly investigate the behavior of the HPR model in a large number of different standard benchmark problems of computational fluid mechanics and computational solid mechanics.

It is important to mention that exactly for such a general class of nonlinear time-dependent hyperbolic PDEs, the families of ADER finite volume (FV) and ADER discontinuous Galerkin (DG) finite element methods have been developed in the past decade. The starting point of the original ADER (arbitrary high order derivatives) schemes of Toro and Titarev et al. for hyperbolic conservation laws [137,122,131,140,132,134,49,24,135] was the approximate solution of the generalized Riemann problem (GRP) [59,15] that arises naturally in the context of high order finite volume and DG schemes, due to their piecewise high order polynomial data representation, for which the vector of conserved variables and all its spatial derivatives are known at a given time level. The ADER approach has been successfully extended also to hyperbolic PDEs with stiff source terms [43,52,82,139], to hyperbolic PDEs with non-conservative products [41,45] and to parabolic problems [63,136,37]. Recent developments include space–time adaptive meshes [53,46,146], moving meshes [40,21], ADER–WENO finite volume schemes for divergence-free magnetohydrodynamics [4,6,5] and *a posteriori* limiting of high order ADER-DG and ADER-FV schemes [93,54,149,148]. In the context of ADER schemes, first order hyperbolic reformulations of parabolic viscous problems have been tackled by Toro and Montecinos in [100,99,138], while a series of interesting previous work on first order hyperbolic reformulations of advection–diffusion equations was proposed by Nishikawa in [106,107]. Although not directly related to viscous problems, we also would like to refer to the well-known relaxation system of Jin and Xin [120], which allows to reformulate any nonlinear hyperbolic conservation law as an augmented linear first order system with stiff relaxation source terms.

In this paper, we concentrate our attention on compressible viscous Newtonian fluids, which in the classical continuum theory can be described by the hyperbolic–parabolic Navier–Stokes–Fourier (NSF) theory, as well as on elastic solids. It should also be noted that there are several advantages of a first order hyperbolic formulation of viscous fluids: first, the use of explicit Godunov-type shock-capturing finite volume schemes and, even more, the use of high order discontinuous Galerkin finite element methods is – at least in principle – *straightforward* for first order systems, while DG schemes need some special care in the presence of parabolic and higher order derivative terms, see the very interesting discussions in the well-known papers of Bassi and Rebay [10], Baumann and Oden [11,12], Cockburn and Shu [31,32], Yan and Shu [144,145,92] and others [1,80,81,86,29,63,44]. Second, the use of a parabolic theory can lead to a severe time step size restriction, if explicit time stepping schemes are used, since the infinite propagation speed of perturbations that is intrinsically inherent in parabolic PDEs is reflected in explicit numerical methods by a stability condition on the time step that scales with the square of the mesh size, while it scales only linearly with the mesh size for first order hyperbolic systems due to the classical CFL condition [34]. The situation is even worse for high order discontinuous Galerkin finite element schemes, where the explicit time step size scales not only quadratically with the mesh size, but where it decreases even quadratically with the order of the method. In Section 4 we will show one numerical example with an explicit time stepping scheme, where the use of the first order HPR model is clearly more convenient in terms of time step size and CPU time compared to the classical parabolic Navier–Stokes theory. As a third and last advantage of a first order hyperbolic model, we would like to emphasize that, by avoiding the presence of *infinite wave speeds* even in the Newtonian framework, the new formulation suggests that its extension to *relativistic continuum mechanics* should also be possible.

1.3. Outline of the paper

The rest of this paper is organized as follows: in Section 2 we recall and discuss the extended hyperbolic Peshkov–Romenski model, denoted by HPR model in the following, including also a hyperbolic formulation of heat conduction. In particular, we show that the system is thermodynamically consistent and symmetric hyperbolic. A sketch of the analysis of the characteristics of the model is provided, together with a dispersion analysis of the wave speeds for relaxation times ranging from zero to infinity. We also carry out a formal asymptotic analysis of the system in the stiff relaxation limit, which reveals the direct connection of the first order HPR model with the well-established hyperbolic–parabolic Navier–Stokes–Fourier equations of viscous heat conducting fluids. In Section 3 we briefly summarize the numerical methods used to solve the HPR model in this paper, namely ADER–WENO finite volume schemes and ADER discontinuous Galerkin finite element methods, making use of the unified $P_N P_M$ framework established in [38], which contains FV schemes and DG methods as two special cases of a more general class of numerical methods. In Section 4 we present computational results for a large set of different multi-dimensional test problems from computational fluid mechanics and also one example from computational solid mechanics, ranging from viscous low Mach number flows over viscous and inviscid compressible flows to the simulation of wave propagation in elastic solids. The paper is rounded-off by some concluding remarks and an outlook to future research in Section 5.

2. Presentation and discussion of the mathematical model

2.1. Formulation of the model

The unified first order hyperbolic model for continuum mechanics proposed by Peshkov and Romenski in [110], including a hyperbolic formulation of heat conduction, reads:

$$\frac{\partial \rho}{\partial t} + \frac{\partial \rho v_k}{\partial x_k} = 0, \tag{1a}$$

$$\frac{\partial \rho v_i}{\partial t} + \frac{\partial \left(\rho v_i v_k + p\delta_{ik} - \sigma_{ik}\right)}{\partial x_k} = 0, \tag{1b}$$

$$\frac{\partial A_{ik}}{\partial t} + \frac{\partial A_{im} v_m}{\partial x_k} + v_j \left(\frac{\partial A_{ik}}{\partial x_j} - \frac{\partial A_{ij}}{\partial x_k} \right) = -\frac{\psi_{ik}}{\theta_1(\tau_1)}, \tag{1c}$$

$$\frac{\partial \rho J_i}{\partial t} + \frac{\partial \left(\rho J_i v_k + T\delta_{ik}\right)}{\partial x_k} = -\frac{\rho H_i}{\theta_2(\tau_2)}, \tag{1d}$$

$$\frac{\partial \rho s}{\partial t} + \frac{\partial \left(\rho s v_k + H_k\right)}{\partial x_k} = \frac{\rho}{\theta_1(\tau_1) T} \psi_{ik}\psi_{ik} + \frac{\rho}{\theta_2(\tau_2) T} H_i H_i \geq 0, \tag{1e}$$

The solutions of the above PDE system fulfill also the additional conservation law

$$\frac{\partial \rho E}{\partial t} + \frac{\partial \left(v_k \rho E + v_i (p\delta_{ik} - \sigma_{ik}) + q_k\right)}{\partial x_k} = 0, \tag{2}$$

which is the conservation of total energy. We emphasize that in the numerical computations shown later in Section 4 of this paper, we solve the energy equation (2) instead of the entropy equation (1e), but from the point of view of the model formulation, the entropy should be considered among the vector of unknowns (see Section 2.2.1 for a discussion).

Here we use the following notation: ρ is the mass density, $[v_i] = \mathbf{v} = (u, v, w)$ is the velocity vector, $[A_{ik}] = \boldsymbol{A}$ is the distortion tensor, $[J_i] = \mathbf{J}$ is the thermal impulse vector, s is the entropy, $E = E(\rho, s, \mathbf{v}, \boldsymbol{A}, \mathbf{J})$ is the total energy, $p = \rho^2 E_\rho$ is the pressure, δ_{ik} is the Kronecker delta, $[\sigma_{ik}] = \boldsymbol{\sigma} = -[\rho A_{mi} E_{A_{mk}}]$ is the symmetric viscous shear stress tensor, $T = E_s$ is the temperature, $[q_k] = \mathbf{q} = [E_s E_{J_k}]$ is the heat flux vector and $\theta_1 = \theta_1(\tau_1) > 0$ and $\theta_2 = \theta_2(\tau_2) > 0$ are positive scalar functions, which will be specified below, depending on the strain dissipation time $\tau_1 > 0$ and the thermal impulse relaxation time $\tau_2 > 0$, respectively. The dissipative terms ψ_{ik} and H_i on the right hand side of the evolution equations for $\boldsymbol{A}$, $\mathbf{J}$ and s are defined as $[\psi_{ik}] = \boldsymbol{\psi} = [E_{A_{ik}}]$ and $[H_i] = \mathbf{H} = [E_{J_i}]$, respectively. Hence, the viscous stress tensor and the heat flux vector are directly related to the dissipative terms on the right hand side via $\boldsymbol{\sigma} = -\rho \boldsymbol{A}^T \boldsymbol{\psi}$ and $\mathbf{q} = T\,\mathbf{H}$. Note that E_ρ, E_s, $E_{A_{ik}}$ and E_{J_i} should be understood as the partial derivatives $\partial E/\partial \rho$, $\partial E/\partial s$, $\partial E/\partial A_{ik}$ and $\partial E/\partial J_i$; they are the so-called *energy gradients in the state space* or the *thermodynamic forces*. The Einstein summation convention over repeated indices is implied.

These equations are the mass conservation (1a), the momentum conservation (1b), the time evolution for the distortion (1c), the time evolution for the thermal impulse (1d), the entropy time evolution (1e), and the total energy conservation (2). The PDE governing the time evolution of the thermal impulse (1d) looks formally very similar to the momentum equation (1b), where the temperature T takes the role of the pressure p. Due to this similarity, it will also be called the *thermal momentum equation* in the following.

One can clearly see that in order to close the system, it is necessary to specify the total energy potential $E(\rho, s, \mathbf{v}, \boldsymbol{A}, \mathbf{J})$. This potential then generates all the constitutive fluxes (*i.e.* non-advective fluxes) and source terms by means of its partial derivatives with respect to the state variables. Hence, the energy specification is one of the key steps in the model formulation.

In order to specify E, we note that there are three scales involved in the continuum model formulation described in the introduction. Namely, the molecular scale, or the *microscale*; the scale of the material elements, called here *mesoscale*; and the flow scale, or the *macroscale*. It is therefore assumed that the total energy E is the sum of three terms, each of which represents the energy distributed in its corresponding scale. Thus, we assume that

$$E(\rho, s, \mathbf{v}, \boldsymbol{A}, \mathbf{J}) = E_1(\rho, s) + E_2(\boldsymbol{A}, \mathbf{J}) + E_3(\mathbf{v}). \tag{3}$$

The terms E_3 and E_1 are conventional. They are the specific kinetic energy per unit mass $E_3(\mathbf{v}) = \frac{1}{2} v_i v_i$, which represents the macroscale part of the total energy, and the *internal energy* $E_1(\rho, s)$, which is related to the kinetic energy of the molecular motion. $E_1(\rho, s)$ is the only energy which does not disappear in the thermodynamic equilibrium where any meso- and macroscopic dynamics are absent, and only molecular dynamics is present. For this reason, it is sometimes referred to as the *equilibrium energy*. In this paper, for E_1, we shall use either the *ideal gas equation of state*

$$E_1(\rho, s) = \frac{c_0^2}{\gamma(\gamma - 1)}, \quad c_0^2 = \gamma \rho^{\gamma - 1} e^{s/c_V}, \tag{4}$$

or the *stiffened gas equation of state*

$$E_1(\rho, s) = \frac{c_0^2}{\gamma(\gamma - 1)} \left(\frac{\rho}{\rho_0} \right)^{\gamma - 1} e^{s/c_V} + \frac{\rho_0 c_0^2 - \gamma p_0}{\gamma \rho}, \quad c_0^2 = const. \tag{5}$$

In both cases, c_0 has the meaning of the adiabatic sound speed; c_V and c_p are the specific heat capacities at constant volume and at constant pressure, respectively, which are related by the ratio of specific heats $\gamma = c_p / c_V$. In (5), ρ_0 is the reference mass density and p_0 is the reference (atmospheric) pressure.

For the mesoscopic, or *non-equilibrium*, part of the total energy, we shall use a quadratic form

$$E_2(\boldsymbol{A}, \mathbf{J}) = \frac{c_s^2}{4} G_{ij}^{\mathrm{TF}} G_{ij}^{\mathrm{TF}} + \frac{\alpha^2}{2} J_i J_i, \tag{6}$$

with

$$[G_{ij}^{\mathrm{TF}}] = \mathrm{dev}(\mathbf{G}) = \mathbf{G} - \frac{1}{3} \mathrm{tr}(\mathbf{G}) \mathbf{I}, \qquad \text{and} \qquad \mathbf{G} = \boldsymbol{A}^{\mathsf{T}} \boldsymbol{A}. \tag{7}$$

Here, $[G_{ij}^{\mathrm{TF}}] = \mathrm{dev}(\mathbf{G})$ is the deviator, or the *trace-free* part, of the tensor $\mathbf{G} = \boldsymbol{A}^{\mathsf{T}} \boldsymbol{A}$ and $\mathrm{tr}(\mathbf{G}) = G_{ii}$ is its trace, $\mathbf{I}$ is the unit tensor and c_s is the characteristic velocity of propagation of transverse perturbations. In the following we shall refer to it as the *shear sound velocity*. The characteristic velocity of heat wave propagation c_h is related to α,[5] as discussed later in Section 2.2.2. We stress that $E_2(\boldsymbol{A}, \mathbf{J})$ is a simple *quadratic form* in terms of G_{ij}^{TF} and $\mathbf{J}$.

We also note that, because of the frame invariance principle, or *objectivity principle*, the total energy can depend on vectors and tensors by means of their invariants only. By a direct calculation, one can see that

$$G_{ij}^{\mathrm{TF}} G_{ij}^{\mathrm{TF}} \equiv I_2 - I_1^2 / 3,$$

where $I_1 = \mathrm{tr}(\mathbf{G})$ and $I_2 = \mathrm{tr}(\mathbf{G}^2)$, and therefore E_2, as well as the total energy E, are a function of invariants of $\boldsymbol{A}$ and $\mathbf{J}$.

In general, the mesoscopic energy $E_2(\boldsymbol{A}, \mathbf{J})$ can also be a function of ρ and s in addition to $\boldsymbol{A}$ and $\mathbf{J}$. This would correspond to a coupling between the molecular scale and the scale of material elements. Such a dependence on ρ and s should be introduced in the velocities c_s and α, *i.e.* $c_s = c_s(\rho, s)$, $\alpha = \alpha(\rho, s)$. The dependencies $c_s(\rho, s)$ and $\alpha(\rho, s)$ should be taken into account when strongly non-equilibrium flows are considered. This would affect the computation of the pressure and of the temperature through the partial derivatives E_ρ and E_s and give rise to a so-called *non-equilibrium pressure* and a *non-equilibrium temperature*. For simplicity, however, in this paper we do *not* consider such a possibility, and c_s and α are assumed to be *constant*.

The algebraic source term on the right-hand side of equation (1c) describes the shear strain dissipation due to material element rearrangements, and the source term on the right-hand side of (1d) describes the relaxation of the thermal impulse due to heat exchange between material elements.

After the total energy potential has been specified, one can write all fluxes and source terms in an explicit form. Thus, for the energy $E_2(\boldsymbol{A}, \mathbf{J})$ given by (6), we have $\boldsymbol{\psi} = E_{\boldsymbol{A}} = c_s^2 \boldsymbol{A}\, \mathrm{dev}(\mathbf{G})$, hence the shear stresses are

$$\boldsymbol{\sigma} = -\rho \boldsymbol{A}^{\mathsf{T}} \boldsymbol{\psi} = -\rho \boldsymbol{A}^{\mathsf{T}} E_{\boldsymbol{A}} = -\rho c_s^2 \mathbf{G}\, \mathrm{dev}(\mathbf{G}), \qquad \mathrm{tr}(\boldsymbol{\sigma}) = 0, \tag{8}$$

and the strain dissipation source term is

[5] The physical units of α are $\mathrm{kg}/(\mathrm{K\,m\,s}^2)$.

$$-\frac{\boldsymbol{\psi}}{\theta_1(\tau_1)} = -\frac{E_{\boldsymbol{A}}}{\theta_1(\tau_1)} = -\frac{3}{\tau_1}\,|\boldsymbol{A}|^{\frac{5}{3}}\,\boldsymbol{A}\,\mathrm{dev}(\mathbf{G}), \tag{9}$$

where we have chosen $\theta_1(\tau_1) = \tau_1 c_s^2/3\,|\boldsymbol{A}|^{-\frac{5}{3}}$, with $|\boldsymbol{A}| = \det(\boldsymbol{A}) > 0$ the determinant of $\boldsymbol{A}$ and τ_1 being the strain relaxation time, or, in other words, the time scale that characterizes how long a material element is connected with its neighbor elements before rearrangement.[6] Note, that the determinant of $\boldsymbol{A}$ must satisfy the *constraint*

$$|\boldsymbol{A}| = \frac{\rho}{\rho_0}, \tag{10}$$

where ρ_0 is the density at a reference configuration, see [110]. Furthermore, from the energy potential $E_2(\boldsymbol{A}, \mathbf{J})$ the heat flux vector follows with $E_{\mathbf{J}} = \alpha^2 \mathbf{J}$ directly as

$$\mathbf{q} = T\,\mathbf{H} = E_s E_{\mathbf{J}} = \alpha^2 T \mathbf{J}. \tag{11}$$

For the thermal impulse relaxation source term, we choose $\theta_2 = \tau_2 \alpha^2 \frac{\rho}{\rho_0}\frac{T_0}{T}$, and hence

$$-\frac{\rho\mathbf{H}}{\theta_2(\tau_2)} = -\frac{\rho E_{\mathbf{J}}}{\theta_2(\tau_2)} = -\frac{T}{T_0}\frac{\rho_0}{\rho}\frac{\rho\mathbf{J}}{\tau_2}. \tag{12}$$

It contains another characteristic relaxation time τ_2 that is associated to heat conduction.

The motivation for this particular choice of θ_1 and θ_2 can be found later in Section 2.3, where a formal asymptotic analysis of the model is presented, and where the connection with classical Navier–Stokes–Fourier theory is established in the stiff limit $\tau_1 \to 0$ and $\tau_2 \to 0$.

2.2. Discussion

In this section, we discuss a few additional important properties of the HPR model. We first illustrate the relation of the HPR model to the laws of thermodynamics and the important role played by the total energy potential. In particular, we demonstrate that the HPR model is compatible with the first and second law of thermodynamics, and that this automatically implies that the HPR model is a *hyperbolic* system of PDEs, *i.e.* the Cauchy problem for the system (1) is well-posed. We complete this section by unveiling the characteristic structure of the HPR model.

2.2.1. Thermodynamically compatible systems of hyperbolic conservation laws and well-posedness

Overdetermined system of PDEs and the first law of thermodynamics. As many other models of continuum mechanics, the system (1)–(2) is an *overdetermined* system of PDEs. It consists of 18 PDEs for just 17 unknowns, and hence the natural question arises of whether it is *consistent*, *i.e.* whether it has at least one solution satisfying all the PDEs. This is in general not guaranteed and one needs to provide evidences that a solution satisfying all the PDEs of the system does exist.

In 1961, after discovering the mutual relations between thermodynamics, well-posedness of the initial value problem for systems of conservation laws and stability of numerical schemes, Godunov [68,67] concluded that an overdetermined system of conservation laws representing a continuum mechanics model is consistent if it is compatible with the first law of thermodynamics, i.e. with the total energy conservation. In order to illustrate Godunov's idea, let us consider equations (1)–(2) and let's also assume that it is an abstract system of PDEs, not necessarily related to the subject of this paper. Following Godunov [68,67,69], we now show that if the unknown function $E(t, \mathbf{x})$ is in fact not an unknown but a *potential*, depending on all other unknowns, *i.e.* $E = E(\rho, \mathbf{v}, \boldsymbol{A}, \mathbf{J}, s)$, then, if a solution of system (1) exists, it also satisfies equation (2), *i.e.* the system (1)–(2) is consistent. In fact, we have to use the so-called *conservative variables*, *i.e.* we should consider the potential ρE as a function of ρ, $\rho\mathbf{v}$, $\boldsymbol{A}$, $\rho\mathbf{J}$, ρs. After this remark, one can see that equation (2) can be obtained as a linear combination of equations (1) multiplied by the factors[7] $E - V E_V - s E_s - v_i E_{v_i} - J_i E_{J_i}$, $(\rho E)_{\rho v_i}$, $(\rho E)_{A_{ik}}$, $(\rho E)_{\rho J_i}$, and $(\rho E)_{\rho s}$, *i.e.*

$$(E - V E_V - s E_s - v_i E_{v_i} - J_i E_{J_i}) \cdot (1) + (\rho E)_{\rho v_i} \cdot (1b) + (\rho E)_{A_{ik}} \cdot (1c) + (\rho E)_{\rho J_i} \cdot (1d) + (\rho E)_{\rho s} \cdot (1e) \equiv (2). \tag{13}$$

Here, the notation $V = \rho^{-1}$ was used. Because of the Gibbs identity

$$\mathrm{d}(\rho E) \equiv (E - V E_V - s E_s - v_i E_{v_i} - J_i E_{J_i})\mathrm{d}\rho + (\rho E)_{\rho v_i}\mathrm{d}\rho v_i + (\rho E)_{A_{ik}}\mathrm{d}A_{ik} + (\rho E)_{\rho J_i}\mathrm{d}\rho J_i + (\rho E)_{\rho s}\mathrm{d}\rho s, \tag{14}$$

it is obvious that (13) indeed holds for the time derivatives, as well as it holds for the right-hand sides, but it is less obvious that it is true for the space derivatives. In fact, the constitutive terms in the fluxes, *i.e.* $\rho^2 E_\rho$, $\rho A_{mi} E_{mk}$, E_s, and E_{J_k} are chosen in these forms on purpose, because otherwise it is impossible to get fully conservative fluxes in the energy conservation, but some non-conservative products would appear (details can be found in [69,70,78], see also appendix in [109]), which apparently violates energy conservation.

[6] Following Frenkel [60], this relaxation time was called particle-settled-life (PSL) time in [110].

[7] We recall that these factors should be understood as the partial derivatives, *e.g.* $(\rho E)_{\rho v_i} = \partial(\rho E)/\partial(\rho v_i)$.

Thus, identity (13) shows that if equations (1) are fulfilled, then equation (2) is also automatically fulfilled. We stress once more that in order to have the property that the *overdetermined* system (1)–(2) of 18 PDEs for 17 unknowns is a *consistent* system, the following constraints should hold

- the function $E(t,\mathbf{x})$ is *not* an unknown but rather a *potential*, depending on the remaining unknowns, i.e. $E = E(\rho,\mathbf{v},\boldsymbol{A},\mathbf{J},s)$;
- all the constitutive terms in the fluxes and the dissipative source terms of the HPR model (1) are directly generated by the total energy potential by means of its gradients E_ρ, $E_{A_{ij}}$, E_{J_i}, E_s in the state space and they must have this particular form in order to guarantee total energy conservation.

In other words, these two requirements form the *closure* for the overdetermined system (1)–(2), making it consistent.

Well-posedness of the Cauchy problem. It is not sufficient to propose a new continuum model that respects only some fundamental physical principles, but it is also required that the Cauchy problem for the proposed system of governing PDEs be *well-posed*, *i.e.* the solution of the system with initial data at time $t = 0$ exists, at least locally, it is unique and stable. Otherwise, the practical value of the model would be questionable. In this context, hyperbolic conservation laws are very desirable for modeling dynamical phenomena, because hyperbolicity implies that the model is *causal* (finite speed of perturbation propagation) and that the Cauchy problem for the nonlinear PDE system under consideration is *well-posed* (hence, suitable for numerical treatment), see *e.g.* see [71,66,35,89].

From the discussion of the previous paragraph, it is obvious that the total energy potential plays a central role in the formulation of the HPR model. Moreover, we shall demonstrate that the convexity of the energy potential also guarantees that system (1) is *symmetric hyperbolic*, *i.e.* the initial value problem for (1) is well-posed.

As noted by Godunov [68,67,69], an interesting parametrization of overdetermined systems of conservation laws is possible. This parametrization allows to rewrite the original system in a symmetric quasilinear form. If, in addition, the total energy E is a *convex function* of the state variables, then the system is symmetric hyperbolic. After a careful analysis of a large number of models in continuum mechanics, the original observation of Godunov was later extended to a wide class of thermodynamically consistent systems of hyperbolic conservation laws in a series of papers [75,76,72,77,117,118] by Godunov and Romenski. All models belonging to this class of conservation laws are automatically symmetric hyperbolic. In particular, the system (1)–(2) belongs to this class, see [72,117,118]. Therefore, in order to demonstrate that system (1) is symmetric hyperbolic, we introduce the so-called *thermodynamically conjugate*, or dual, state variables, which are in fact the factors in (13):

$$r = E - VE_V - sE_s - v_iE_{v_i} - J_iE_{J_i},\quad v_i = (\rho E)_{\rho v_i},\quad \alpha_{ik} = (\rho E)_{A_{ik}},\quad \Theta_i = (\rho E)_{\rho J_i},\quad \sigma = (\rho E)_{\rho s}, \tag{15}$$

and the new thermodynamic potential L as the Legendre transform of ρE, *i.e.*

$$L(r, v_i, \alpha_{ik}, \Theta_i, \sigma) = r\rho + v_i\rho v_i + \alpha_{ik}A_{ik} + \Theta_i\rho J_i + \sigma\rho s - \rho E = \rho^2 E_\rho + \rho A_{ij}E_{A_{ij}}. \tag{16}$$

Now, the left hand side of (1) can be rewritten as follows[8] (details can be found in [75–77,117,118,109])

$$\frac{\partial L_r}{\partial t} + \frac{\partial (v_kL)_r}{\partial x_k} = 0, \tag{17a}$$

$$\frac{\partial L_{v_i}}{\partial t} + \frac{\partial (v_kL)_{v_i}}{\partial x_k} + L_{\alpha_{im}}\frac{\partial \alpha_{km}}{\partial x_k} - L_{\alpha_{mk}}\frac{\partial \alpha_{mk}}{\partial x_i} = 0, \tag{17b}$$

$$\frac{\partial L_{\alpha_{il}}}{\partial t} + \frac{\partial (v_kL)_{\alpha_{il}}}{\partial x_k} + L_{\alpha_{ml}}\frac{\partial v_m}{\partial x_i} - L_{\alpha_{il}}\frac{\partial v_k}{\partial x_k} = 0, \tag{17c}$$

$$\frac{\partial L_{\Theta_i}}{\partial t} + \frac{\partial (v_kL)_{\Theta_i}}{\partial x_k} + \frac{\partial \sigma\delta_{ik}}{\partial x_k} = 0, \tag{17d}$$

$$\frac{\partial L_\sigma}{\partial t} + \frac{\partial (v_kL)_\sigma}{\partial x_k} + \frac{\partial \Theta_k}{\partial x_k} = 0, \tag{17e}$$

and then in the quasilinear form

$$\boldsymbol{\mathcal{M}}(\mathbf{P})\frac{\partial \mathbf{P}}{\partial t} + \boldsymbol{\mathcal{H}}_k(\mathbf{P})\frac{\partial \mathbf{P}}{\partial x_k} = 0, \tag{18}$$

where $\mathbf{P} = (r, v_i, \alpha_{ik}, \Theta_i, \sigma)$, and matrices $\boldsymbol{\mathcal{M}}^T = \boldsymbol{\mathcal{M}}$ and $\boldsymbol{\mathcal{H}}_k^T = \boldsymbol{\mathcal{H}}_k$ are symmetric, and moreover $\boldsymbol{\mathcal{M}} > 0$ if the potential $L(r, v_i, \alpha_{ik}, \Theta_i, \sigma)$ is a convex function. We recall, that because of the properties of the Legendre transformation, the convexity of $L(r, v_i, \alpha_{ik}, \Theta_i, \sigma)$ is equivalent to the convexity of ρE with respect to the conservative variable. In other words,

[8] We restrict the demonstration by considering only the left-hand side of (1) because the type of a system of PDEs is defined by the leading terms.

the system (18), as well as (1), is *symmetric hyperbolic* if ρE is a convex potential of the conservative state variables, and the solution to the initial value problem exists locally. In turn, we note that via a direct calculation one can verify that the convexity of ρE with respect to the conservative state variables is equivalent to the convexity of E with respect to the primitive state variables ρ, v_i, A_{ij}, J_i and s.

However, as it is well-known in the nonlinear elasticity theory, e.g. [35,105], the question of convexity of the energy E with respect to all nine components A_{ij} of the distortion is not a trivial one. More precisely, there is no isotropic convex function $E(\mathbf{A})$ satisfying the stress free condition $E_{A_{ij}} = 0$ at the rest state, e.g. see [78,73] for the convexity criteria. In practice however, and in particular for the ADER approach used in this paper, this was never a problem (see also the multi-dimensional numerical examples for nonlinear elastic deformation in [73,57]), and a weaker condition for hyperbolicity is used. Namely, due to the Galilean invariance of equations (1), (2) [105], it is sufficient to require that E is a convex function with respect to three components A_{ik} of each three columns $k = 1, 2, 3$ of $\boldsymbol{A}$, i.e. that the three 3×3-matrices $E_{A_{ik}A_{jk}}$, with $k = 1, 2, 3$, are positive definite. For example, the simple choice (6) gives us an energy which is convex with respect to each triplet A_{ik}, $k = 1, 2, 3$ [110]. See also [105] for rigorous hyperbolicity criteria for a specific choice of the energy potential.

Energy transformation and the second law. The energy is the only quantity that is allowed to be transferred among all the three scales involved, namely the micro-, meso-, and macroscales. Therefore, the scales can interact only through an energy exchange, and the total energy potential has to be involved in some way in the mathematical formulation of this interaction. Indeed, the energy transfer from meso- to macroscale, $E_2(\boldsymbol{A}, \mathbf{J}) \rightarrow E_3(\mathbf{v})$, is known as *reversible* energy transformation, and is controlled by the momentum fluxes, and as we have seen in the previous paragraph, these fluxes are given by the gradients E_ρ and $E_{A_{ij}}$. The energy transfer from meso- to microscale, $E_1(\rho, s) \leftarrow E_2(\boldsymbol{A}, \mathbf{J})$, is an *irreversible* transformation, which is controlled by the dissipative source terms in the governing equations for the distortion tensor, the thermal impulse, and the entropy. Thus, it is natural to expect that these dissipative source terms in the HPR model are also generated by the energy potential, via its partial derivatives with respect to the state variables. Indeed, the total energy conservation principle holds regardless of whether dissipation is present, or not. Thus, even if the dissipative source terms are present, we anyway have to have zero on the right-hand side of the total energy conservation law. Since the HPR model is an overdetermined system of PDEs, we require that the summation identity (13) holds. Hence, each dissipative source term is multiplied by the corresponding factor (conjugate state variables (15)) and the sum must vanish. Let us denote the source terms in equations (1c) and (1d) by $S^A_{ik} = -\psi_{ik}/\theta_1$ and $S^{\rho J}_i = -\rho H_i/\theta_2$, respectively, while the source term in the entropy equation (1e) is denoted by $S^{\rho s}$. In the summation identity (13), they are multiplied by $(\rho E)_{A_{ik}} = \rho E_{A_{ik}}$, $(\rho E)_{\rho J_i} = E_{J_i}$ and $(\rho E)_{\rho s} = E_s = T$, respectively. Total energy conservation requires that the right hand side of (13) vanishes, i.e.

$$\rho E_{A_{ik}} S^A_{ik} + E_{J_i} S^{\rho J}_i + E_s S^{\rho s} = 0. \tag{19}$$

The only freedom we have to satisfy the total energy conservation law is to set

$$S^{\rho s} = -\frac{1}{E_s}\left(\rho E_{A_{ik}} S^A_{ik} + E_{J_i} S^{\rho J}_i\right) = \frac{1}{E_s}\left(\rho E_{A_{ik}} \frac{\psi_{ik}}{\theta_1} + E_{J_i} \frac{\rho H_i}{\theta_2}\right). \tag{20}$$

At that point, we recall that the thermodynamics of dissipative processes requires that the entropy cannot decrease, and hence the entropy production (20) has to be nonnegative. A simple possibility to guarantee this is to assume that the terms ψ_{ik} and H_i are proportional to the gradients $E_{A_{ik}}$ and E_{J_i}, respectively, with some positive coefficients. This makes the entropy source term a positive definite quadratic form, which guarantees that the entropy does not decrease. Since the functions $\theta_1 > 0$ and $\theta_2 > 0$ are positive, in this paper we have simply chosen

$$\psi_{ik} = E_{A_{ik}} \qquad \text{and} \qquad H_i = E_{J_i}. \tag{21}$$

2.2.2. Characteristic speeds and sound speeds

Understanding the *characteristic* structure of a hyperbolic system is an important step in studying the solution properties, because the solution of a hyperbolic model is a combination of waves propagating along the *characteristic lines*, *e.g.* see [71, 35]. In this section we study the characteristic structure of the HPR model. First we shall present the characteristic structure of the viscous part of the HPR model (equations (1a), (1b), (1c) and (2)), then we discuss the characteristic structure of the heat conducting part (equations (1d) and (1e)), and eventually we close this section by presenting the structure of the entire model (1). It is also important to recall that the characteristic speeds of a hyperbolic model with stiff dissipative source terms are not the true sound speeds in the media, because these apparent sound speeds are strongly influenced by the dissipative processes giving rise to the phenomena called sound dispersion. In fact, the characteristic speeds of a hyperbolic system with stiff dissipative source terms are the high frequency limits for sound speeds [104].

We also note that the HPR model is fundamentally different from the classical parabolic NSF theory in the way it treats viscous and heat conducting phenomena. In the classical NSF theory, the transport phenomena are treated by means of phenomenological transport relations such as, for example, Newton's law of viscosity and Fourier's law of heat conduction, while in the HPR model all transport phenomena are treated from the wave propagation point of view. Thus, as it will be shown below, there are four types of sound waves in the HPR model, one for the transport of longitudinal (or pressure) perturbations, two for shear perturbations, and one for heat transfer, in contrast to only one pressure wave in the NSF model.

Viscous subsystem. Let us consider system (1) in the one-dimensional case. If a direction x_k is chosen, then in terms of the vector of primitive state variables

$$\mathbf{V} = (\rho, p, v_1, v_2, v_3, A_{1k}, A_{2k}, A_{3k})^{\mathsf{T}}, \tag{22}$$

PDEs (1a), (2), (1b) and (1c) can be written in the quasilinear form

$$\frac{\partial \mathbf{V}}{\partial t} + \mathcal{C}_k(\mathbf{V}) \frac{\partial \mathbf{V}}{\partial x_k} = \mathbf{S}_k(\mathbf{V}) \tag{23}$$

with the source vector

$$\mathbf{S}_k(\mathbf{V}) = (0, 0, 0, 0, 0, -E_{A_{1k}}/\theta_1, -E_{A_{2k}}/\theta_1, -E_{A_{3k}}/\theta_1)^{\mathsf{T}},$$

and matrix $\mathcal{C}_k(\mathbf{V})$ given in Appendix A as well as the formulas of the eigenvalues for $\mathcal{C}_k$. The full basis consisting of eigenvectors of the matrix $\mathcal{C}_k$ can be also obtained in the same way as it is done in [8,9]. We note that in [8,9], the time evolution equation for $\boldsymbol{A}^{-1}$ was used instead of equation (1c).

In order to illustrate the characteristic structure of (23) we restrict ourselves to the consideration of a fluid (or solid) at the rest state $\mathbf{V}_0$, *i.e.* $\mathbf{v} = 0$, $\boldsymbol{A} = \mathbf{I}$, $\rho = \rho_0$. If the internal energy $E_1(\rho, s)$ is considered in the form (4), or (5), and $E_2(\boldsymbol{A})$ in the form (6) then matrix $\mathcal{C}_k$, $k = 1$, looks as follows

$$\mathcal{C}_1 = \begin{pmatrix} 0 & 0 & \rho & 0 & 0 & 0 & 0 & 0 \\ 0 & 0 & c_0^2 & 0 & 0 & 0 & 0 & 0 \\ 0 & \rho^{-1} & 0 & 0 & 0 & \frac{4}{3}c_s^2 & 0 & 0 \\ 0 & 0 & 0 & 0 & 0 & 0 & c_s^2 & 0 \\ 0 & 0 & 0 & 0 & 0 & 0 & 0 & c_s^2 \\ 0 & 0 & 1 & 0 & 0 & 0 & 0 & 0 \\ 0 & 0 & 0 & 1 & 0 & 0 & 0 & 0 \\ 0 & 0 & 0 & 0 & 1 & 0 & 0 & 0 \end{pmatrix}.$$

Its non-zero eigenvalues are $\lambda_{1,2,3,4} = \pm c_s$, $\lambda_{5,6} = \pm\sqrt{c_0^2 + \frac{4}{3}c_s^2}$. Thus, the eigenvalues $\lambda_{1,2,3,4}$ are (in general, they are distinct if shear flow is present) transverse, or shear, characteristic speeds, while $\lambda_{5,6}$ is the longitudinal characteristic speed. In the framework of solid mechanics, the existence of two types of waves comes with no surprise, but this is much less obvious for fluid mechanics. However, this fact is in full agreement with the causality principle and the wave propagation point of view on the transport phenomena, as it was already mentioned above.

Yet another point has to be explained. One may note that the characteristic velocity corresponding to the propagation of pressure perturbations in fluids modeled by EOS (4) or (5) is c_0, while we get $\sqrt{c_0^2 + \frac{4}{3}c_s^2} \neq c_0$ for $c_s \neq 0$. In fact, this is not a paradox. It is necessary to recall that for the hyperbolic PDEs with stiff dissipative source terms like system (23), the characteristic speeds are not the *true sound speeds*, but the true sound speeds are the result of a coupling of the non-dissipative waves modeled by the left hand side of (23) and the dissipative processes modeled by the algebraic source terms, and therefore the true sound speeds can be obtained only via a *dispersion analysis*. However, such an analysis is outside the scopes of this paper, some details of it are given just to demonstrate that there is no controversy between the sound speeds predicted by the HPR model and experimental observations on sound propagation in fluids.

The dispersion relation for a hyperbolic system of PDEs of the form (23) with algebraic dissipative source terms is [104]

$$\det\left(\mathbf{I} - z\mathcal{C}_k + \frac{i}{\omega}\mathcal{E}\right) = 0, \tag{24}$$

where $\omega = 2\pi f$ is the angular frequency, f is the wave frequency, $z = k/\omega$, k is the complex wave number, i is the imaginary unit, matrices $\mathcal{C}_k = \mathcal{C}_k(\mathbf{V}_0)$ and $\mathcal{E}(\mathbf{V}_0) = \partial\mathbf{S}/\partial\mathbf{V}$ are taken at the rest state $\mathbf{V}_0$, and $\mathbf{I}$ is the identity matrix of the same size as $\mathcal{C}_k$ and $\mathcal{E}$. Once the solution z to (24) is found, the phase velocity, V, and the attenuation factor, a, of a harmonic sound wave of frequency ω are given by

$$V = \frac{1}{\mathrm{Re}(z)}, \quad a = -\omega\,\mathrm{Im}(z). \tag{25}$$

Equation (24) has six nontrivial solutions, four corresponding to the transverse waves

$$z_{1,2} = -\sqrt{\frac{\Omega - 3i}{\Omega c_s^2}}, \quad z_{3,4} = \sqrt{\frac{\Omega - 3i}{\Omega c_s^2}}, \tag{26}$$

and two corresponding to the longitudinal waves

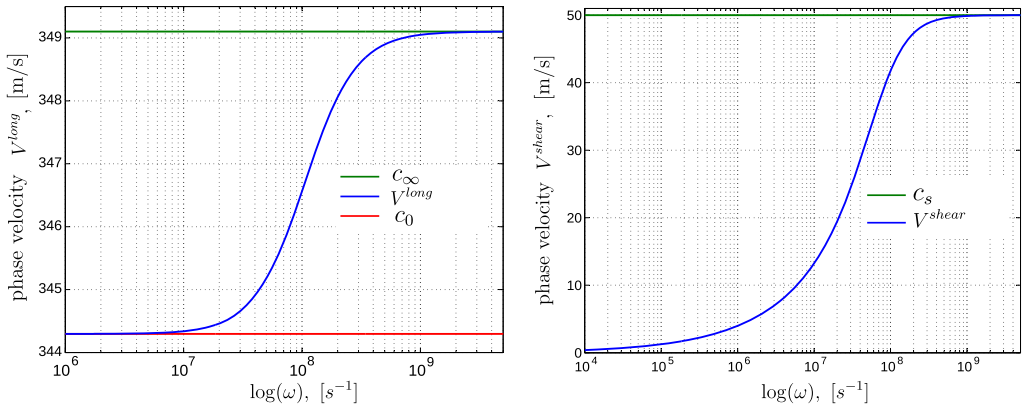

Fig. 1. Phase velocity of the longitudinal wave (left) and shear wave (right) versus $\log(\omega)$ propagating in a viscous gas with parameters $\rho = 1.177$ kg/m^3, $\gamma = 1.4$, $c_v = 718$ J/(kg K), $s = 8100$, $c_0 = 344.3$ m/s, $c_s = 50$ m/s, $\mu = 1.846 \cdot 10^{-5}$ Pa s, $\tau_1 = 3.76 \cdot 10^{-8}$ s.

$$z_{5,6} = \pm\sqrt{\frac{3(\Omega - 2i)}{3c_0^2(\Omega - 2i) + 4\Omega c_s^2}}, \tag{27}$$

where $\Omega = \tau_1\omega$. Thus, for the *longitudinal sound waves* the phase velocity and the attenuation factor are

$$V^{long} = \frac{c_\infty}{2X}\left(\sqrt{(X-\Omega)(Y-\Omega)} + \sqrt{(X+\Omega)(Y+\Omega)}\right), \tag{28}$$

$$a^{long} = \frac{\omega}{2c_\infty Y}\left(\sqrt{(X-\Omega)(Y+\Omega)} - \sqrt{(X+\Omega)(Y-\Omega)}\right), \tag{29}$$

$$c_\infty = \sqrt{c_0^2 + \frac{4}{3}c_s^2}, \quad X = \sqrt{\Omega^2 + 16}, \quad Y = \sqrt{\Omega^2 + 16\left(\frac{c_0}{c_\infty}\right)^4},$$

and for *shear sound waves* they are

$$V^{shear} = c_t\sqrt{\frac{\Omega(Z+\Omega)}{2Z^2}}, \quad a^{shear} = \frac{\omega}{c_s\sqrt{2\Omega}}\sqrt{Z-\Omega}, \quad Z = \sqrt{\Omega^2+9}. \tag{30}$$

By a direct verification, one can see that the low ($\Omega \to 0$) and high ($\Omega \to \infty$) frequency limits of V^{long} are c_0 and c_∞, accordingly, while for V^{shear} they are 0 and c_s. This clearly indicates that (i) perturbations of any frequency propagate at finite speeds in contrast to the classical NSF theory and that (ii) the low frequency sound waves propagate at velocities $\approx c_0$ what we in fact use to call the sound speed in fluids. Fig. 1 shows the longitudinal and shear sound speeds as a function of the angular frequency ω.

Heat conducting subsystem. For convenience, we rewrite the heat conduction equations (1d) and (1e) in the form

$$\rho\frac{\mathrm{d}J_k}{\mathrm{d}t} + \frac{\partial E_s}{\partial x_k} = -\frac{\rho E_{J_k}}{\theta_2}, \tag{31a}$$

$$\rho\frac{\mathrm{d}s}{\mathrm{d}t} + \frac{\partial E_{J_k}}{\partial x_k} = \frac{\rho}{\theta_2 E_s}E_{J_i}E_{J_i} \geq 0, \tag{31b}$$

where $\mathrm{d}/\mathrm{d}t = \partial/\partial t + v_k\partial/\partial x_k$ is the material time derivative, and the energy potential E is taken to be $E = E_1(\rho, s) + \alpha^2 J_k J_k/2$, while the ideal gas EOS (4) is used for $E_1(\rho, s)$. Let us consider this system in the direction x_1, then it can be rewritten in a quasilinear form

$$\frac{\mathrm{d}}{\mathrm{d}t}\begin{pmatrix} J_1 \\ s \end{pmatrix} + \begin{pmatrix} 0 & \frac{T}{\rho c_V} \\ \frac{\alpha^2}{\rho} & 0 \end{pmatrix}\frac{\partial}{\partial x_1}\begin{pmatrix} J_1 \\ s \end{pmatrix} = \frac{\rho_0}{\rho T_0 \tau_2}\begin{pmatrix} -TJ_1 \\ +\alpha^2 J_1^2 \end{pmatrix}. \tag{32}$$

The eigenvalues of the homogeneous part of the system (32) are $\lambda_{1,2} = \mp\alpha\sqrt{T}/(\rho\sqrt{c_V})$, and in the following we shall use the notation

$$c_h = \frac{\alpha}{\rho}\sqrt{\frac{T}{c_V}} \tag{33}$$

for the velocity of the heat characteristic. The dispersion relation (24) for the heat conducting subsystem (32) can also be treated analytically. Thus, the phase velocity for harmonic heat waves of angular frequency ω is

$$V^{heat} = 2\frac{\alpha\sqrt{T\Omega}}{\rho\sqrt{c_V}}\left(\frac{\sqrt{X+\rho}+\sqrt{X-\rho}}{\sqrt{X+\rho}-\sqrt{X-\rho}+2X+2\Omega}\right), \quad X=\sqrt{\rho^2+\Omega^2}, \quad \Omega=\tau_2\omega. \tag{34}$$

In particular, one can see that the low frequency limit ($\Omega=\tau_2\omega\to 0$) and the high frequency limit ($\Omega=\tau_2\omega\to\infty$) of the phase velocity are 0 and c_h, respectively.

The full system. We shall now consider the full HPR system and study its characteristic structure assuming that the space coordinate x_1 is chosen as the direction of wave propagation. We choose the following vector of primitive state variables

$$\mathbf{V}=(\rho,\, p,\, J_1,\, v_1,\, v_2,\, v_3,\, A_{11},\, A_{21},\, A_{31})^{\mathsf{T}}. \tag{35}$$

To discuss the characteristic structure, it is again sufficient to consider wave propagation near the rest state $\mathbf{V}_0$ characterized by $\mathbf{v}=0$, $\boldsymbol{A}=\mathbf{I}$, $\mathbf{J}=0$. If the ideal gas EOS is used for the $E_1(\rho,s)$, the system matrix $\boldsymbol{\mathcal{C}}_1(\mathbf{V}_0)$ of the quasi-linear system reads as

$$\boldsymbol{\mathcal{C}}_1(\mathbf{V}_0)=\begin{pmatrix} 0 & 0 & 0 & \rho & 0 & 0 & 0 & 0 & 0\\ 0 & 0 & \beta c_h^2 & \rho c_0^2 & 0 & 0 & 0 & 0 & 0\\ -\frac{T}{\rho} & \beta^{-1} & 0 & 0 & 0 & 0 & 0 & 0 & 0\\ 0 & \rho^{-1} & 0 & 0 & 0 & 0 & \frac{4}{3}c_s^2 & 0 & 0\\ 0 & 0 & 0 & 0 & 0 & 0 & 0 & c_s^2 & 0\\ 0 & 0 & 0 & 0 & 0 & 0 & 0 & 0 & c_s^2\\ 0 & 0 & 0 & 1 & 0 & 0 & 0 & 0 & 0\\ 0 & 0 & 0 & 0 & 1 & 0 & 0 & 0 & 0\\ 0 & 0 & 0 & 0 & 0 & 1 & 0 & 0 & 0 \end{pmatrix}, \tag{36}$$

where $\beta=c_V(\gamma-1)\rho^2$, $T=E_s$. This matrix has eight non-zero eigenvalues; four eigenvalues $\lambda_{1,2,3,4}=\mp c_s$ corresponding to two shear waves, two eigenvalues

$$\lambda_{5,6}=\mp\frac{1}{\sqrt{2}}\sqrt{C-\frac{\sqrt{C^2-4\rho c_h^2(\beta T+\frac{4}{3}\rho c_s^2)}}{\rho}}, \quad C=c_0^2+c_h^2+\frac{4}{3}c_s^2 \tag{37}$$

corresponding to heat waves, and two eigenvalues

$$\lambda_{7,8}=\mp\frac{1}{\sqrt{2}}\sqrt{C+\frac{\sqrt{C^2-4\rho c_h^2(\beta T+\frac{4}{3}\rho c_s^2)}}{\rho}}, \quad C=c_0^2+c_h^2+\frac{4}{3}c_s^2 \tag{38}$$

corresponding to longitudinal pressure waves. The same dispersion analysis as above can be performed for the viscous heat conducting case, but we do not enter such details here, as they would distract us from the main purpose of the present work.

2.3. Formal asymptotic analysis, Newton's viscous law and Fourier's law of heat conduction

In this section we show how to establish a link between the HPR model (1)–(2) and the classical Navier–Stokes–Fourier (NSF) theory in the stiff relaxation limit[9] $\tau_1\ll 1$ and $\tau_2\ll 1$.

2.3.1. Asymptotic limit of the viscous stress tensor

We first concentrate on the relaxation limit of the viscous stress tensor $\boldsymbol{\sigma}$. For that purpose, we can ignore the rotational degree of freedom contained in the distortion tensor $\boldsymbol{A}$, since $\boldsymbol{\sigma}$ is only a function of the symmetric tensor $\mathbf{G}=\mathbf{A}^{\mathsf{T}}\boldsymbol{A}$, which contains only the information about the deformation of the material elements. The temporal evolution equation of $\mathbf{G}$ can be obtained from Eqn. (1c) as[10]

$$\dot{\mathbf{G}}=-\left(\mathbf{G}\nabla\mathbf{v}+\nabla\mathbf{v}^{\mathsf{T}}\mathbf{G}\right)+\frac{2}{\rho\,\theta_1}\boldsymbol{\sigma}, \tag{39}$$

where $\dot{\mathbf{G}}=\partial\mathbf{G}/\partial t+\mathbf{v}\cdot\nabla\mathbf{G}$ is the material time derivative of $\mathbf{G}$ and $\nabla\mathbf{v}$ is the velocity gradient.

We now proceed with a *formal* asymptotic expansion[11] of the tensor $\mathbf{G}$ in a series of the small relaxation parameter τ_1,

$$\mathbf{G}=\mathbf{G}_0+\tau_1\mathbf{G}_1+\tau_1^2\mathbf{G}_2+\dots \tag{40}$$

[9] Also called the long wavelength limit.

[10] To obtain this PDE, it is necessary to sum up equation (1c) multiplied by $\mathbf{A}^{\mathsf{T}}$ from the left and transpose equation (1c) multiplied by $\boldsymbol{A}$ from the right, since $\dot{\mathbf{G}}=\mathbf{A}^{\mathsf{T}}\dot{\mathbf{A}}+\dot{\mathbf{A}}^{\mathsf{T}}\mathbf{A}$. We also use here that $\boldsymbol{\sigma}=-\rho\mathbf{A}^{\mathsf{T}}E_{\mathbf{A}}=-\rho(E_{\mathbf{A}})^{\mathsf{T}}\boldsymbol{A}=\boldsymbol{\sigma}^{\mathsf{T}}$.

[11] The so-called Chapman–Enskog expansion.

Furthermore, we have to specify θ_1. In this paper, we choose $\theta_1 = \tau_1 |\mathbf{A}|^{-\frac{5}{3}} c_s^2/3 = \tau_1 |\mathbf{G}|^{-\frac{5}{6}} c_s^2/3$. Now, inserting (40) into (39) and collecting terms of the same power in τ_1 yields:

$$\frac{\mathrm{d}}{\mathrm{d}t}(\mathbf{G}_0 + \tau_1 \mathbf{G}_1 + \ldots) = -\left((\mathbf{G}_0 + \tau_1 \mathbf{G}_1 + \ldots)\nabla \mathbf{v} + \nabla \mathbf{v}^{\mathsf{T}} (\mathbf{G}_0 + \tau_1 \mathbf{G}_1 + \ldots)\right) - \frac{6}{\tau_1} |\mathbf{G}_0 + \tau_1 \mathbf{G}_1 + \ldots|^{\frac{5}{6}} (\mathbf{G}_0 + \tau_1 \mathbf{G}_1 + \ldots) \operatorname{dev}(\mathbf{G}_0 + \tau_1 \mathbf{G}_1 + \ldots), \tag{41}$$

and then

$$\tau_1^{-1} \underbrace{\left(6|\mathbf{G}_0|^{\frac{5}{6}} \mathbf{G}_0 \operatorname{dev}(\mathbf{G}_0)\right)}_{0} + \tau_1^0 \underbrace{\left(\frac{\mathrm{d}\mathbf{G}_0}{\mathrm{d}t} + \ldots\right)}_{0} + \ldots = 0. \tag{42}$$

Inviscid fluid as a zeroth order approximation. Since (42) is valid for any τ_1, the coefficients multiplying powers of τ_1 must all vanish. Furthermore, density positivity $\rho = \rho_0 |\mathbf{A}| = \rho_0 |\mathbf{G}|^{\frac{1}{2}} > 0$ implies that $|\mathbf{G}| > 0$, hence $\mathbf{G}$ is invertible. Therefore, from the first term in (42), it follows that

$$\operatorname{dev}(\mathbf{G}_0) = 0, \quad \Rightarrow \quad \mathbf{G}_0 - \frac{1}{3} \operatorname{tr}(\mathbf{G}_0) \mathbf{I} = 0, \quad \Rightarrow \quad \mathbf{G}_0 = \frac{1}{3} \operatorname{tr}(\mathbf{G}_0) \mathbf{I}. \tag{43}$$

Setting $g := \frac{1}{3} \operatorname{tr}(\mathbf{G}_0)$ and neglecting higher order terms in τ_1, we get the first important result:

$$\mathbf{G} = g\mathbf{I} + \tau_1 \mathbf{G}_1 = \boldsymbol{A}^{\mathsf{T}} \boldsymbol{A}, \tag{44}$$

which means that the distortion tensor $\boldsymbol{A}$ tends towards an *orthogonal matrix* in the stiff limit $\tau_1 \ll 1$.

To obtain the unknown coefficient g from known quantities, we compute the determinant of $\mathbf{G}$ from (44), neglecting small terms of the order $\mathcal{O}(\tau_1)$. Hence,

$$|\mathbf{G}| = g^3 = |\boldsymbol{A}|^2, \qquad \Rightarrow \qquad g = |\mathbf{G}|^{\frac{1}{3}} = |\boldsymbol{A}|^{\frac{2}{3}} = \left(\frac{\rho}{\rho_0}\right)^{\frac{2}{3}}. \tag{45}$$

If we retain only the leading zeroth order term $\mathbf{G}_0$ of the expansion (40), then $\mathbf{G} = \mathbf{G}_0 = g\mathbf{I}$ and thus $\sigma = -\rho c_s^2 \mathbf{G}_0 \operatorname{dev}(\mathbf{G}_0) = 0$, *i.e.* viscous stresses vanish and we retrieve the *inviscid* case (compressible Euler equations) as a zeroth order approximation of the HPR model in the stiff limit $\tau_1 \ll 1$. The relations (44) and (45) above also imply that in the inviscid limit, the *shape* of the material elements does not change, but only their *volume*.

Newton's viscous law as a first order approximation. We are now interested in a first order approximation of the viscous stress tensor $\boldsymbol{\sigma}$ that results in the stiff relaxation limit $\tau_1 \ll 1$. For that purpose, we expand the stress tensor (8) in a series of τ_1. Here, we will use that $\mathbf{G} = g\mathbf{I} + \tau_1 \mathbf{G}_1$, which results in $\rho = \rho_0 |\mathbf{A}| = \rho_0 |g\mathbf{I} + \tau_1 \mathbf{G}_1|^{\frac{1}{2}} = \rho_0 (g^{3/2} + \frac{\tau_1}{2} g^{1/2} \operatorname{tr}(\mathbf{G}_1) + \mathcal{O}(\tau_1^2))$ and $\operatorname{dev}(\mathbf{G}) = \operatorname{dev}(g\mathbf{I} + \tau_1 \mathbf{G}_1) = \tau_1 \operatorname{dev}(\mathbf{G}_1)$:

$$\boldsymbol{\sigma} = -\rho c_s^2 \mathbf{G} \operatorname{dev}(\mathbf{G}) = -\rho_0 c_s^2 \left(g^{3/2} + \frac{\tau_1}{2} g^{1/2} \operatorname{tr}(\mathbf{G}_1)\right) (g\mathbf{I} + \tau_1 \mathbf{G}_1)\, \tau_1 \operatorname{dev}(\mathbf{G}_1). \tag{46}$$

Thus, ignoring higher order terms in τ_1 yields

$$\boldsymbol{\sigma} = -\tau_1 \rho_0 c_s^2 g^{5/2} \operatorname{dev}(\mathbf{G}_1). \tag{47}$$

The evolution equation for $\operatorname{dev}(\mathbf{G})$, which is obtained by applying the "dev" operator to (39), reads:

$$\frac{\mathrm{d}}{\mathrm{d}t} \operatorname{dev}(\mathbf{G}) + \mathbf{G}\nabla \mathbf{v} + \nabla \mathbf{v}^{\mathsf{T}} \mathbf{G} - \frac{1}{3} \operatorname{tr}(\mathbf{G}\nabla \mathbf{v} + \nabla \mathbf{v}^{\mathsf{T}} \mathbf{G}) \mathbf{I} = -\frac{6}{\tau_1} |\mathbf{G}|^{5/6} \operatorname{dev}(\mathbf{G} \operatorname{dev}(\mathbf{G})). \tag{48}$$

Inserting the expansion (40) into (48), collecting terms of the same power of τ_1 and recalling from (43) that $\operatorname{dev} \mathbf{G}_0 = 0$, one gets for the leading order terms (τ_1^0):

$$\mathbf{G}_0 \nabla \mathbf{v} + \nabla \mathbf{v}^{\mathsf{T}} \mathbf{G}_0 - \frac{2}{3} \operatorname{tr}(\mathbf{G}_0 \nabla \mathbf{v}) \mathbf{I} = -6 |\mathbf{G}_0|^{7/6} \operatorname{dev}(\mathbf{G}_1).$$

Since $\mathbf{G}_0 = g\mathbf{I}$, the last equality can be rewritten as

$$g \left(\nabla \mathbf{v} + \nabla \mathbf{v}^{\mathsf{T}} - \frac{2}{3} \operatorname{tr}(\nabla \mathbf{v}) \mathbf{I}\right) = -6\, g^{7/2} \operatorname{dev}(\mathbf{G}_1). \tag{49}$$

By inserting (49) into (47), we conclude that

$$\boldsymbol{\sigma} = \frac{1}{6}\tau_1 \rho_0 c_s^2 \left(\nabla \mathbf{v} + \nabla \mathbf{v}^T - \frac{2}{3} \operatorname{tr}(\nabla \mathbf{v}) \mathbf{I} \right) := \mu \left(\nabla \mathbf{v} + \nabla \mathbf{v}^T - \frac{2}{3} (\nabla \cdot \mathbf{v}) \mathbf{I} \right), \tag{50}$$

which is the classical stress tensor known from the compressible Navier–Stokes equations based on Stokes' hypothesis, with the dynamic viscosity coefficient

$$\mu = \frac{1}{6}\tau_1 \rho_0 c_s^2, \tag{51}$$

as already given in [110].[12] This completes the formal asymptotic analysis, establishing a direct connection of the stress tensor $\boldsymbol{\sigma}$ of the HPR model with the known viscous stress tensor of the compressible Navier–Stokes equations, which is automatically recovered by the HPR model for small relaxation times $\tau_1 \ll 1$. At this point it is very important to highlight that in the HPR model, the viscous stress tensor $\boldsymbol{\sigma}$ obtained in the stiff relaxation limit (50) is a *result* of the choice of a simple quadratic form for the contribution $E_2(\boldsymbol{A}, \mathbf{J})$ to the total energy potential E, see Eqn. (6). In contrast, in classical Navier–Stokes theory, the stress tensor $\boldsymbol{\sigma}$ is postulated as a constitutive relation right from the beginning.

Our particular choice of θ_1 has been made only in order to obtain a *constant* viscosity coefficient μ. In order to obtain a variable viscosity coefficient that depends, for example, on the temperature, like in Sutherland's law, it is sufficient to modify the function $\theta_1(\tau_1)$ accordingly.

2.3.2. Asymptotic limit of the heat flux

Next, we proceed with a similar formal asymptotic analysis of the heat flux $\mathbf{q} = \alpha^2 T \mathbf{J}$, which is, however, much simpler than the previous analysis of the stress tensor $\boldsymbol{\sigma}$. We recall the governing PDE (1d) for the vector $\mathbf{J}$ with the choice $\theta_2 = \tau_2 \alpha^2 \frac{\rho}{\rho_0} \frac{T_0}{T}$:

$$\frac{\partial \rho \mathbf{J}}{\partial t} + \nabla \cdot (\rho \mathbf{J} \otimes \mathbf{u}) + \nabla T = -\frac{1}{\tau_2} \frac{T}{T_0} \frac{\rho_0}{\rho} \rho \mathbf{J}. \tag{52}$$

The Chapman–Enskog expansion of $\mathbf{J}$ in terms of the small parameter $\tau_2 \ll 1$ reads

$$\mathbf{J} = \mathbf{J}_0 + \tau_2 \mathbf{J}_1 + \tau_2^2 \mathbf{J}_2 + \dots, \tag{53}$$

which can be directly inserted into (52). Collecting terms of equal powers in τ_2 and setting all the individual coefficients to zero, like in the previous section, yields:

$$\tau_2^{-1} \underbrace{\left(\frac{T}{T_0} \frac{\rho_0}{\rho} \rho \mathbf{J}_0 \right)}_{0} + \tau_2^0 \underbrace{\left(\frac{\partial \rho \mathbf{J}_0}{\partial t} + \nabla \cdot (\rho \mathbf{J}_0 \otimes \mathbf{u}) + \nabla T + \frac{T}{T_0} \frac{\rho_0}{\rho} \rho \mathbf{J}_1 \right)}_{0} + \dots = 0, \tag{54}$$

hence, the leading zeroth order term and the first order term of the expansion are given by

$$\mathbf{J}_0 = 0, \qquad \text{and} \qquad \mathbf{J}_1 = -\frac{T_0}{T \rho_0} \nabla T, \tag{55}$$

so that the expansion (53) up to first order terms becomes

$$\mathbf{J} = -\tau_2 \frac{T_0}{\rho_0} \frac{\nabla T}{T}. \tag{56}$$

Inserting (56) into the heat flux $\mathbf{q} = \alpha^2 T \mathbf{J}$ present in the energy equation (2) yields

$$\mathbf{q} = \alpha^2 T \mathbf{J} = -\alpha^2 \tau_2 \frac{T_0}{\rho_0} \nabla T := -\kappa \nabla T, \tag{57}$$

which is the familiar form of the Fourier heat flux with heat conduction coefficient

$$\kappa = \alpha^2 \tau_2 \frac{T_0}{\rho_0} \tag{58}$$

that is recovered for small relaxation times $\tau_2 \ll 1$.

[12] Please note that for obtaining a constant viscosity coefficient μ as given in (51), in [110] there was a factor $|A|^{\frac{8}{3}}$ missing in front of the relaxation source term $\boldsymbol{\psi}$.

2.3.3. On the experimental measurement of the model parameters

As we have seen in the previous section, the relation between the conventional transport coefficients, the viscosity coefficient μ and heat conductivity κ, are given by (51) and (58), respectively. From these relations, however, it is impossible to recover both parameters, τ_1 and c_s or τ_2 and α, of the HPR model, and an experimental way to do that has to be pointed out. So far, we see a possibility to make measurements of the HPR model parameters using experiments on high frequency sound propagation. For example, experimental results from [123] show that for the vapor of methyl-chloride (CH_3Cl) at temperature 30 °C the low (adiabatic sound speed) and high frequency limits of the longitudinal phase velocity V^{long} are (for simplicity, we ignore here the heat conducting effect)

$$c_0 \approx 250 \text{ m/s}, \quad c_\infty \approx 258 \text{ m/s}.$$

Using these data and that $c_\infty = \sqrt{c_0^2 + \frac{4}{3}c_s^2}$ in the HPR model, we get that $c_s \approx 55.21$ m/s, and the dissipation time is $\tau_1 = 6\mu/(\rho_0 c_s^2) \approx 1.545 \cdot 10^{-7}$ s, where $\mu = 1.57 \cdot 10^{-4}$ Pa s and $\rho_0 = 2$ kg/m^3. In general, the heat conducting effect cannot be ignored, and some extra high frequency heat wave propagation experiments should be conducted in order to measure the characteristic heat wave velocity c_h.

3. ADER finite volume and ADER discontinuous Galerkin finite element schemes

The equations (1)–(2) of the HPR model described above can be written in the following general form of a nonlinear system of hyperbolic PDEs with non-conservative products and stiff source terms:

$$\frac{\partial \mathbf{Q}}{\partial t} + \nabla \cdot \mathbf{F}(\mathbf{Q}) + \mathcal{B}(\mathbf{Q}) \cdot \nabla \mathbf{Q} = \mathbf{S}(\mathbf{Q}), \tag{59}$$

where $\mathbf{Q} = \mathbf{Q}(\mathbf{x}, t)$ is the state vector; $\mathbf{x} = (x, y, z) \in \Omega \subset \mathbb{R}^d$ is the vector of spatial coordinates and Ω denotes the computational domain in d space dimensions; $\mathbf{F}(\mathbf{Q}) = (\mathbf{f}, \mathbf{g}, \mathbf{h})$ is the nonlinear flux tensor that contains the conservative part of the PDE system and $\mathcal{B}(\mathbf{Q}) \cdot \nabla \mathbf{Q}$ is a genuinely non-conservative term. When written in quasilinear form, the system (59) becomes

$$\frac{\partial \mathbf{Q}}{\partial t} + \mathcal{A}(\mathbf{Q}) \cdot \nabla \mathbf{Q} = \mathbf{S}(\mathbf{Q}), \tag{60}$$

where the matrix $\mathcal{A}(\mathbf{Q}) = \partial \mathbf{F}(\mathbf{Q})/\partial \mathbf{Q} + \mathcal{B}(\mathbf{Q})$ includes both the Jacobian of the conservative flux, as well as the non-conservative product. The hyperbolicity of system (60) has been discussed in [110]. However, for the practical implementation of the numerical schemes used in this paper, the eigenvectors $\mathbf{R}_n$ of the matrix $\mathcal{A}_n = \mathcal{A}(\mathbf{Q}) \cdot \mathbf{n}$ ($\mathbf{n}$ is a unit-normal vector) will not be needed, even if they were in principle available.

The PDE system (59) is solved by resorting to a high order one-step ADER-FV and ADER-DG method [112,38,41], which provides at the same time high order of accuracy in both space and time in one single step, hence completely avoiding the Runge–Kutta sub-stages that are typically used in Runge–Kutta DG and Runge–Kutta WENO schemes. The method will be presented in the *unified* framework of $P_N P_M$ methods introduced in [38], which contains both, DG schemes and FV schemes as special cases of a more general class of methods. For related work on $P_N P_M$ schemes, the reader is referred to [94,95]. The construction of fully-discrete high order one-step schemes is typical of the ADER approach [132]. In the following we only summarize the main steps, while for more details the reader is referred to [38,52,82,61,6,54,149,148].

3.1. Data representation and reconstruction

The computational domain Ω is discretized by a computational mesh (structured or unstructured), composed of conforming elements denoted by T_i, where the index i ranges from 1 to the total number of elements N_E. We will further denote the volume (area) of an individual cell by $|T_i| = \int_{T_i} d\mathbf{x}$. The discrete solution of PDE (59) is denoted by $\mathbf{u}_h(\mathbf{x}, t^n)$ and is represented by piecewise polynomials of maximum degree $N \geq 0$. Within each cell T_i we have

$$\mathbf{u}_h(\mathbf{x}, t^n) = \sum_{l}^{\mathcal{N}} \Phi_l(\mathbf{x}) \hat{\mathbf{u}}_{l,i}^n := \Phi_l(\mathbf{x})\, \hat{\mathbf{u}}_{l,i}^n, \quad \mathbf{x} \in T_i, \tag{61}$$

where we have introduced the classical Einstein summation convention over two repeated indices. The discrete solution $\mathbf{u}_h(\mathbf{x}, t^n)$ is defined in the space of piecewise polynomials up to degree N, spanned by a set of basis functions $\Phi_l = \Phi_l(\mathbf{x})$. Throughout this paper we use the orthogonal Dubiner-type basis for simplex elements, which is a so-called *modal basis*, detailed in [36,84], while we use a tensor-product-type *nodal basis* for quadrilateral elements [54]. The nodal basis is given by the Lagrange interpolation polynomials passing through the Gauss–Legendre quadrature nodes on the unit square [126]. The symbol $\mathcal{N}$ denotes the number of degrees of freedom per element and is given by $\mathcal{N} = (N+1)(N+2)/2$ for simplex elements and by $\mathcal{N} = (N+1)^2$ for quadrilateral elements in two space dimensions. In the framework of $P_N P_N$ methods, the discrete solution $\mathbf{u}_h$ is now *reconstructed* in order to obtain for each element a piecewise polynomial $\mathbf{w}_h(\mathbf{x}, t)$ of degree

$M \geq N$, with a total number of $\mathcal{M}$ degrees of freedom. Details on the nonlinear WENO reconstruction and on the $P_N P_M$ reconstruction can be found in [47,48,38] and are not repeated here. The number of degrees of freedom $\mathcal{M}$ is again $\mathcal{M} = (M+1)(M+2)/2$ for simplex elements and $\mathcal{M} = (M+1)^2$ for quadrilateral elements in 2D, respectively. The reconstruction step is simply abbreviated by $\mathbf{w}_h(\mathbf{x},t) = \mathcal{R}(\mathbf{u}_h(\mathbf{x},t))$, and the reconstruction polynomial $\mathbf{w}_h(\mathbf{x},t)$ is written as

$$\mathbf{w}_h(\mathbf{x},t^n) = \sum_{l}^{\mathcal{M}} \Psi_l(\mathbf{x}) \hat{\mathbf{w}}_{l,i}^n := \Psi_l(\mathbf{x})\, \hat{\mathbf{w}}_{l,i}^n, \quad \mathbf{x} \in T_i. \tag{62}$$

Note that for $N = M$ the $P_N P_M$ method reduces to a classical discontinuous Galerkin finite element scheme, with the reconstruction operator equal to the identity operator, $\mathcal{R} = \mathcal{I}$, or, equivalently, $\mathbf{w}_h(\mathbf{x},t^n) = \mathbf{u}_h(\mathbf{x},t^n)$, while for the case $N = 0$ the method reduces to a standard high order WENO finite volume scheme if a WENO reconstruction operator is adopted.

For WENO schemes on structured meshes we have found that it is particularly convenient to adopt one-dimensional stencils, each composed by $n_e = M + 1$ cells, which are subsequently oriented along each spatial direction. The resulting reconstruction is still multidimensional, but implemented in a dimension-by-dimension strategy. A complete description of this approach can be found in [53,146]. For unstructured meshes, on the contrary, intrinsically multidimensional stencils are built, with $n_e = d\mathcal{M}$, where d is the number of space dimensions. Moreover, the total number of stencils is seven, i.e. one central stencil, three primary sector stencils and three reverse sector stencils. Further details can be found in [48,47,133,141].

In this paper, however, we will only use these two special limits of the general $P_N P_M$ approach, i.e. either $N = 0$ (pure FV) or $N = M$ (pure DG).

3.2. Local space–time predictor

The discrete solution $\mathbf{w}_h(\mathbf{x},t^n)$ is now evolved in time according to an element-local weak formulation of the governing PDE in space–time, see [43,38,82,52,61,6,54,149,148]. The local space–time Galerkin method is only used for the construction of an element-local predictor solution of the PDE *in the small*, hence neglecting the influence of neighbor elements. This predictor will subsequently be inserted into the corrector step described in the next section, which then provides the appropriate coupling between neighbor elements via a numerical flux function (Riemann solver) and a path-conservative jump term for the discretization of the non-conservative product. To simplify notation, we define

$$\langle f, g \rangle = \int_{t^n}^{t^{n+1}} \int_{T_i} f(\mathbf{x},t) g(\mathbf{x},t)\, d\mathbf{x}\, dt, \qquad [f,g]^t = \int_{T_i} f(\mathbf{x},t) g(\mathbf{x},t)\, d\mathbf{x}, \tag{63}$$

which denote the scalar products of two functions f and g over the space–time element $T_i \times \left[t^n; t^{n+1}\right]$ and over the spatial element T_i at time t, respectively. Within the local space–time predictor, the discrete solution of equation (59) is denoted by $\mathbf{q}_h = \mathbf{q}_h(\mathbf{x},t)$. We then multiply (59) with a space–time test function $\theta_k = \theta_k(\mathbf{x},t)$ and subsequently integrate over the space–time control volume $T_i \times \left[t^n; t^{n+1}\right]$. Inserting $\mathbf{q}_h$, the following weak formulation of the PDE is obtained:

$$\left\langle \theta_k, \frac{\partial \mathbf{q}_h}{\partial t} \right\rangle + \langle \theta_k, \nabla \cdot \mathbf{F}(\mathbf{q}_h) + \mathcal{B}(\mathbf{q}_h) \cdot \nabla \mathbf{q}_h \rangle = \langle \theta_k, \mathbf{S}(\mathbf{q}_h) \rangle . \tag{64}$$

The discrete representation of $\mathbf{q}_h$ in element $T_i \times [t^n, t^{n+1}]$ is assumed to have the following form

$$\mathbf{q}_h = \mathbf{q}_h(\mathbf{x},t) = \sum_l \theta_l(\mathbf{x},t) \hat{\mathbf{q}}_{l,i}^n := \theta_l \hat{\mathbf{q}}_{l,i}^n, \tag{65}$$

where $\theta_l(\mathbf{x},t)$ is a space–time basis function of maximum degree M. For the basis functions θ_l we use the nodal basis given in [38] on simplex elements, while we use a tensor-product of 1D nodal basis functions given by the Lagrange interpolation polynomials of the Gauss–Legendre quadrature points for quadrilateral elements. After integration by parts in time of the first term, eqn. (64) reads

$$[\theta_k, \mathbf{q}_h]^{t^{n+1}} - \left[\theta_k, \mathbf{w}_h(\mathbf{x},t^n)\right]^{t^n} - \left\langle \frac{\partial}{\partial t}\theta_k, \mathbf{q}_h \right\rangle + \langle \theta_k, \nabla \cdot \mathbf{F}(\mathbf{q}_h) + \mathcal{B}(\mathbf{q}_h) \cdot \nabla \mathbf{q}_h \rangle = \langle \theta_k, \mathbf{S}(\mathbf{q}_h) \rangle . \tag{66}$$

Note that the high order polynomial reconstruction of the $P_N P_M$ scheme $\mathbf{w}_h(\mathbf{x},t^n)$ is taken into account in (66) in a *weak sense* by the term $[\theta_k, \mathbf{w}_h(\mathbf{x},t^n)]^{t^n}$. This corresponds to the choice of a numerical flux in time direction, which is nothing else than *upwinding in time*, according to the causality principle.

Note further that due to the DG approximation in space–time, we may have $\mathbf{q}_h(\mathbf{x},t^n) \neq \mathbf{w}_h(\mathbf{x},t^n)$ in general, hence the choice of a numerical flux in time direction is necessary. Note further that in (66) we have *not* used integration by parts in space, nor any other coupling to spatial neighbor elements. The integrals appearing in the weak form (66), as well as

the space–time test and basis functions involved are conveniently written by making use of a space–time reference element $T_e \times [0;1]$.

The solution of (66) yields the unknown space–time degrees of freedom $\hat{\mathbf{q}}_{l,i}^n$ for each space–time element $T_i \times [t^n; t^{n+1}]$ and is easily achieved with a fast converging iterative scheme, see [38,82,52] for more details. The above space–time Galerkin predictor has replaced the cumbersome Cauchy–Kovalewski procedure that has been initially employed in the original version of ADER finite volume and ADER discontinuous Galerkin schemes [122,131,140,132,49,127,48]. Note that very recently, a new reformulation of the ADER method has been proposed where reconstruction and time evolution are performed in terms of the vector of *primitive variables* $\mathbf{V}$ instead of using the vector $\mathbf{Q}$ of conserved quantities, see [147].

3.3. Fully discrete one-step finite volume and discontinuous Galerkin schemes

At the aid of the local space–time predictor $\mathbf{q}_h$, a fully discrete one-step $P_N P_M$ scheme can now be simply obtained by multiplication of the governing PDE system (59) by test functions Φ_k from the space of piecewise polynomials up to degree N, which are identical with the spatial basis functions of the original data representation before reconstruction, and subsequent integration over the space–time control volume $T_i \times [t^n; t^{n+1}]$. Due to the presence of non-conservative products, the jumps of $\mathbf{q}_h$ across element boundaries are taken into account in the framework of path-conservative schemes put forward by Castro and Parés in the finite volume context [26,108] and subsequently extended to DG schemes in [113] and [41,45], where also a generalization to the unified $P_N P_M$ framework has been provided. All these approaches are based on the theory of Dal Maso, Le Floch and Murat [97], which gives a definition of weak solutions in the context of non-conservative hyperbolic PDE. For open problems concerning path-conservative schemes, the reader is referred to [27].

If $\mathbf{n}$ is the outward pointing unit normal vector on the surface ∂T_i of element T_i and the path-conservative jump term in normal direction is denoted by $\mathcal{D}_h^- \left(\mathbf{q}_h^-, \mathbf{q}_h^+\right) \cdot \mathbf{n}$, which is a function of the left and right boundary-extrapolated data, $\mathbf{q}_h^-$ and $\mathbf{q}_h^+$, respectively, then we obtain the following path-conservative one-step $P_N P_M$ scheme, see [41]:

$$\left(\int_{T_i} \Phi_k \Phi_l d\mathbf{x} \right) \left(\hat{\mathbf{u}}_l^{n+1} - \hat{\mathbf{u}}_l^n \right) + \int_{t^n}^{t^{n+1}} \int_{\partial T_i} \Phi_k \, \mathcal{D}_h^- \left(\mathbf{q}_h^-, \mathbf{q}_h^+\right) \cdot \mathbf{n} \, dS dt$$
$$+ \int_{t^n}^{t^{n+1}} \int_{T_i \setminus \partial T_i} \Phi_k \left(\nabla \cdot \mathbf{F}(\mathbf{q}_h) + \boldsymbol{\mathcal{B}}(\mathbf{q}_h) \cdot \nabla \mathbf{q}_h \right) d\mathbf{x} dt = \int_{t^n}^{t^{n+1}} \int_{T_i} \Phi_k \mathbf{S}(\mathbf{q}_h) d\mathbf{x} dt. \tag{67}$$

The element mass matrix appears in the first integral of (67), the second term accounts for the jump in the discrete solution at element boundaries and the third term takes into account the smooth part of the non-conservative product. For general complex nonlinear hyperbolic PDE systems we use the simple Rusanov method [119] (also called the local Lax Friedrichs method), although any other kind of Riemann solver could be also used, see [135] for an overview of state-of-the-art Riemann solvers. At that point we would also like to point out the new general reformulation of the HLLEM Riemann solver of Einfeldt and Munz [55,56], within the setting of path-conservative schemes recently forwarded in [39], as well as the family of MUSTA schemes, which has been applied to the equations of nonlinear elasticity in [130].

The path-conservative Rusanov jump term reads

$$\mathcal{D}_h^- \left(\mathbf{q}_h^-, \mathbf{q}_h^+\right) \cdot \mathbf{n} = \frac{1}{2} \left(\mathbf{F}(\mathbf{q}_h^+) - \mathbf{F}(\mathbf{q}_h^-) \right) \cdot \mathbf{n} + \frac{1}{2} \left(\tilde{\boldsymbol{\mathcal{B}}} \cdot \mathbf{n} - s_{\max} \mathbf{I} \right) \left(\mathbf{q}_h^+ - \mathbf{q}_h^- \right), \tag{68}$$

with the maximum signal speed at the element interface $s_{\max} = \max\left(\left| \boldsymbol{\Lambda}(\mathbf{q}_h^+) \right|, \left| \boldsymbol{\Lambda}(\mathbf{q}_h^-) \right| \right)$ and the matrix $\tilde{\boldsymbol{\mathcal{B}}} \cdot \mathbf{n}$ given by the following path-integral along a straight line segment path ψ:

$$\tilde{\boldsymbol{\mathcal{B}}} \cdot \mathbf{n} = \int_0^1 \boldsymbol{\mathcal{B}} \left(\psi(\mathbf{q}_h^-, \mathbf{q}_h^+, s) \right) \cdot \mathbf{n} \, ds, \qquad \psi\left(\mathbf{q}_h^-, \mathbf{q}_h^+, s\right) = \mathbf{q}_h^- + s \left(\mathbf{q}_h^+ - \mathbf{q}_h^- \right). \tag{69}$$

According to the suggestions made in [41,45,50,25,51], the path-integrals can be conveniently evaluated numerically by the use of a classical Gauss–Legendre quadrature formula on the unit interval $[0;1]$. For an alternative choice of the path, see [102,103].

This completes the brief description of the $P_N P_M$ scheme used for the discretization of the governing PDE system (59). In the case of ADER–WENO finite volume schemes, we simply have $N = 0$, $\mathcal{N} = 1$, $\Phi_k = 1$, and the limiter is directly incorporated in the *nonlinear* reconstruction operator $\mathbf{w}_h(\mathbf{x}, t^n) = \mathcal{R}\left(\mathbf{u}_h(\mathbf{x}, t^n)\right)$, while for ADER-DG schemes ($N = M$, $\Phi_k = \Psi_k$) a new family of *a posteriori* sub-cell finite volume limiters has been forwarded in [54,149,148]. For alternative finite volume subcell limiters in the context of DG schemes, see the work of Sonntag and Munz [125] and Meister and Ortleb [98].

3.4. Conservation of mass, momentum and total energy

We stress that in our numerical approach, we solve the total energy conservation equation (2) instead of the entropy equation (1e), hence the numerical method is exactly locally and globally conservative for mass, momentum and energy, since for these equations it is written in flux form. Note that the only PDE of the HPR model for which there are non-conservative terms $\mathcal{B}(\mathbf{Q}) \neq 0$ is the evolution equation of the distortion tensor $\boldsymbol{A}$, see (1c). To rewrite (67) in flux form for the cell averages of the mass, momentum and total energy equation we can use the fact that for these equations the corresponding rows of $\mathcal{B}(\mathbf{Q})$ and $\mathbf{S}(\mathbf{Q})$ are zero. Then, set the test functions to $\Phi_k = 1$ in the scheme (this is possible since piecewise constant polynomials are contained in the space of piecewise polynomials up to degree N) and apply the Gauss divergence theorem to the volume integral of the flux divergence in (67). This yields

$$|T_i| \left(\bar{\mathbf{Q}}_i^{n+1} - \bar{\mathbf{Q}}_i^{n} \right) + \int_{t^n}^{t^{n+1}} \int_{\partial T_i} \mathcal{D}_h^- \left(\mathbf{q}_h^-, \mathbf{q}_h^+ \right) \cdot \mathbf{n} \, dS dt + \int_{t^n}^{t^{n+1}} \int_{\partial T_i} \mathbf{F}\left(\mathbf{q}_h^- \right) \cdot \mathbf{n} \, dS dt = 0, \tag{70}$$

with the cell volume $|T_i| = \int_{T_i} d\mathbf{x}$, the cell average of the discrete solution $\bar{\mathbf{Q}}_i^n = \frac{1}{|T_i|} \int_{T_i} \mathbf{u}_h(\mathbf{x}, t^n) d\mathbf{x}$ and the conservative numerical flux function for the Rusanov method

$$\mathcal{G}_h \left(\mathbf{q}_h^-, \mathbf{q}_h^+ \right) \cdot \mathbf{n} = \left(\mathcal{D}_h^- \left(\mathbf{q}_h^-, \mathbf{q}_h^+ \right) + \mathbf{F}\left(\mathbf{q}_h^- \right) \right) \cdot \mathbf{n} = \frac{1}{2} \left(\mathbf{F}(\mathbf{q}_h^+) + \mathbf{F}(\mathbf{q}_h^-) \right) \cdot \mathbf{n} - \frac{1}{2} s_{\max} \left(\mathbf{q}_h^+ - \mathbf{q}_h^- \right), \tag{71}$$

that is obtained by using the definition (68). Hence, for those PDE with $\mathcal{B}(\mathbf{Q}) = 0$ and $\mathbf{S}(\mathbf{Q}) = 0$, the cell averages therefore satisfy

$$|T_i| \left(\bar{\mathbf{Q}}_i^{n+1} - \bar{\mathbf{Q}}_i^{n} \right) + \int_{t^n}^{t^{n+1}} \int_{\partial T_i} \mathcal{G}_h \left(\mathbf{q}_h^-, \mathbf{q}_h^+ \right) \cdot \mathbf{n} \, dS dt = 0, \tag{72}$$

which means that the scheme is locally and globally conservative.

4. Numerical results

As already stated in Sections 2 and 3, we emphasize here again that in the numerical computations shown in this Section, we solve the total energy conservation equation (2) instead of the entropy evolution equation (1e). Such a choice is necessary, since the model (1) and (2) is an *overdetermined* PDE system.

4.1. Numerical convergence studies in the stiff inviscid limit

We first present a numerical convergence study on a smooth unsteady flow, for which an exact analytical solution is known for the compressible Euler equations, i.e. in the inviscid limit $\tau_1 \to 0$ and $\tau_2 \to 0$ of the HPR model.

The computational setup is the classical one of a convected isentropic vortex, see [3,83]. The initial condition is given in terms of primitive variables and it consists in a linear superposition of a homogeneous background field and some perturbations δ:

$$(\rho, u, v, p) = (1 + \delta\rho, 1 + \delta u, 1 + \delta v, 1 + \delta p). \tag{73}$$

We furthermore set the distortion tensor initially to $\boldsymbol{A} = \sqrt[3]{\rho}\,\mathbf{I}$, while the thermal impulse vector is initialized with $\mathbf{J} = 0$. The radial coordinate is related to the Cartesian coordinates x and y by the relation $r^2 = (x-5)^2 + (y-5)^2$. The vortex strength is chosen as $\epsilon = 5$ and the perturbation of entropy $S = \frac{p}{\rho^\gamma}$ is assumed to be zero, while the perturbations of temperature T and velocity $\mathbf{v}$ are given by

$$\begin{pmatrix} \delta u \\ \delta v \end{pmatrix} = \frac{\epsilon}{2\pi} e^{\frac{1-r^2}{2}} \begin{pmatrix} -(y-5) \\ (x-5) \end{pmatrix}, \quad \delta S = 0, \quad \delta T = -\frac{(\gamma-1)\epsilon^2}{8\gamma\pi^2} e^{1-r^2}. \tag{74}$$

From (74) it follows that the perturbations for density and pressure are given by

$$\delta\rho = (1 + \delta T)^{\frac{1}{\gamma-1}} - 1, \quad \delta p = (1 + \delta T)^{\frac{\gamma}{\gamma-1}} - 1. \tag{75}$$

The computational domain is the square $\Omega = [0; 10] \times [0; 10]$ and periodic boundary conditions are applied everywhere. The reference solution $\mathbf{Q}_e$ is given by the exact solution of the compressible Euler equations. In the inviscid case $\mathbf{Q}_e$ is simply the time-shifted initial condition $\mathbf{Q}_e(\mathbf{x}, t) = \mathbf{Q}(\mathbf{x} - \mathbf{v}_c t, 0)$, where the convective mean velocity is $\mathbf{v}_c = (1, 1)$. The test problem is run on a sequence of successively refined meshes until a final time of $t = 1.0$. The chosen physical parameters are $\gamma = 1.4$, $c_v = 2.5$, $\rho_0 = 1$, $c_s = 0.5$ and $\alpha = 1$. The resulting numerical convergence rates obtained with ADER-DG schemes

Table 1
Numerical convergence results for ADER-DG schemes applied to the HPR model ($c_s = 0.5$, $\alpha = 1$) in the low viscosity relaxation limit ($\mu \ll 1, \kappa \ll 1$). Results are shown for the density ρ at a final time of $t = 1$. The reference solution is given by the exact solution of the inviscid compressible Euler equations.

N_x	$\epsilon(L_1)$	$\epsilon(L_2)$	$\epsilon(L_\infty)$	$\mathcal{O}(L_1)$	$\mathcal{O}(L_2)$	$\mathcal{O}(L_\infty)$
ADER-DG P_2P_2 ($\mu = \kappa = 10^{-6}$)						
20	9.4367E−03	2.2020E−03	2.1633E−03			
40	1.9524E−03	4.4971E−04	4.2688E−04	2.27	2.29	2.34
60	7.5180E−04	1.7366E−04	1.4796E−04	2.35	2.35	2.61
80	3.7171E−04	8.6643E−05	7.3988E−05	2.45	2.42	2.41
ADER-DG P_3P_3 ($\mu = \kappa = 10^{-6}$)						
10	1.7126E−02	4.0215E−03	3.6125E−03			
20	6.0405E−04	1.7468E−04	2.1212E−04	4.83	4.52	4.09
30	8.3413E−05	2.5019E−05	2.7576E−05	4.88	4.79	5.03
40	2.1079E−05	6.0168E−06	7.6291E−06	4.78	4.95	4.47
ADER-DG P_4P_4 ($\mu = \kappa = 10^{-7}$)						
10	1.5539E−03	4.5965E−04	5.1665E−04			
20	4.3993E−05	1.0872E−05	1.0222E−05	5.14	5.40	5.66
25	1.8146E−05	4.4276E−06	4.1469E−06	3.97	4.03	4.04
30	8.6060E−06	2.1233E−06	1.9387E−06	4.09	4.03	4.17
ADER-DG P_5P_5 ($\mu = \kappa = 10^{-7}$)						
5	1.1638E−02	1.1638E−02	1.8898E−03			
10	3.9653E−04	9.3717E−05	6.5319E−05	4.88	6.96	4.85
15	4.4638E−05	1.2572E−05	1.9056E−05	5.39	4.95	3.04
20	9.6136E−06	3.0120E−06	3.9881E−06	5.34	4.97	5.44

using polynomial approximation degrees from $N = M = 2$ to $N = M = 5$ are listed in Table 1, together with the chosen values for the effective viscosity μ and the effective heat conductivity coefficient κ. For the higher order schemes, it was necessary to use smaller values of κ and μ, since the scheme otherwise converges to the solution of the viscous problem, while the reference solution is given by the exact solution of the inviscid problem (compressible Euler equations). From Table 1 one can observe that high order of convergence of the numerical method is achieved also in the stiff limit of the governing PDE system.

4.2. Circular explosion problem

Here, we solve a cylindrical explosion problem for the HPR model, similar to the ones proposed in [132,135]. The computational domain is given by $\Omega = [-1; 1]^2$ and the initial condition reads

$$\mathbf{Q}(\mathbf{x}, 0) = \begin{cases} \mathbf{Q}_i & \text{if} \quad r \le R, \\ \mathbf{Q}_o & \text{if} \quad r > R. \end{cases} \tag{76}$$

Here, $R = 0.5$ denotes the radius of the initial discontinuity and the radial coordinate is given by $r = \sqrt{\mathbf{x}^2}$. $\mathbf{Q}_i$ and $\mathbf{Q}_o$ are the inner and outer states, respectively. The inner density and pressure are $\rho_i = 1$ and $p_i = 1$, while the outer density and pressure are $\rho_o = 0.125$ and $p_o = 0.1$, respectively. The initial velocity and the initial thermal impulse vector are $\mathbf{v} = 0$ and $\mathbf{J} = 0$ throughout the entire computational domain, while the distortion tensor is initially set to $\boldsymbol{A} = \sqrt[3]{\rho}\,\mathbf{I}$. The parameters for the HPR model are chosen as follows: $\gamma = 1.4$, $c_v = 2.5$, $\rho_0 = 1$, $c_s = 0.5$, $\alpha = 0.5$, $\mu = \kappa = 10^{-4}$. Due to the cylindrical symmetry of the problem the solution can be compared with an equivalent one dimensional problem in radial direction r with a geometric source term, see [135]. In our case, the 1D reference solution has been computed by solving the compressible Euler equations (i.e. solving the corresponding inviscid flow problem) with a classical second order TVD finite volume scheme on a very fine mesh composed of 10 000 grid zones and using the Osher-type flux proposed in [50]. The two-dimensional simulations with the full HPR model have been carried out with a third order ADER–WENO P_0P_2 scheme on a uniform Cartesian grid with 400×400 control volumes. Fig. 2 shows a 3D plot of the density distribution obtained for this cylindrical explosion case, as well as a 1D cut through the density ρ, the velocity component u and the pressure p at a final time of $t = 0.2$.

As already shown in Eqn. (72), our numerical method is locally and globally conservative for PDE where $\mathcal{B}(\mathbf{Q}) = 0$, and $\mathbf{S} = 0$, which is true for the mass, momentum and total energy conservation equations. In Fig. 3 we provide also numerical evidence that mass, momentum and total energy are really conserved up to machine precision in our approach, by plotting the time evolution of the absolute conservation error for each of the three quantities. The conservation error of a quantity Q at a given time t^n is computed as $\epsilon(Q) = \left|\int_\Omega (Q(\mathbf{x}, t^n) - Q(\mathbf{x}, 0))d\mathbf{x}\right|$. The maximum conservation errors measured during the simulation were $\epsilon(\rho) = 2.77556 \cdot 10^{-14}$ for density, $\epsilon(\rho u) = 1.97758 \cdot 10^{-16}$ for x momentum, $\epsilon(\rho v) = 1.94289 \cdot 10^{-16}$ for y momentum and $\epsilon(\rho E) = 6.30607 \cdot 10^{-14}$ for total energy, respectively. Hence, all conservation errors were of the order of machine accuracy, as expected.

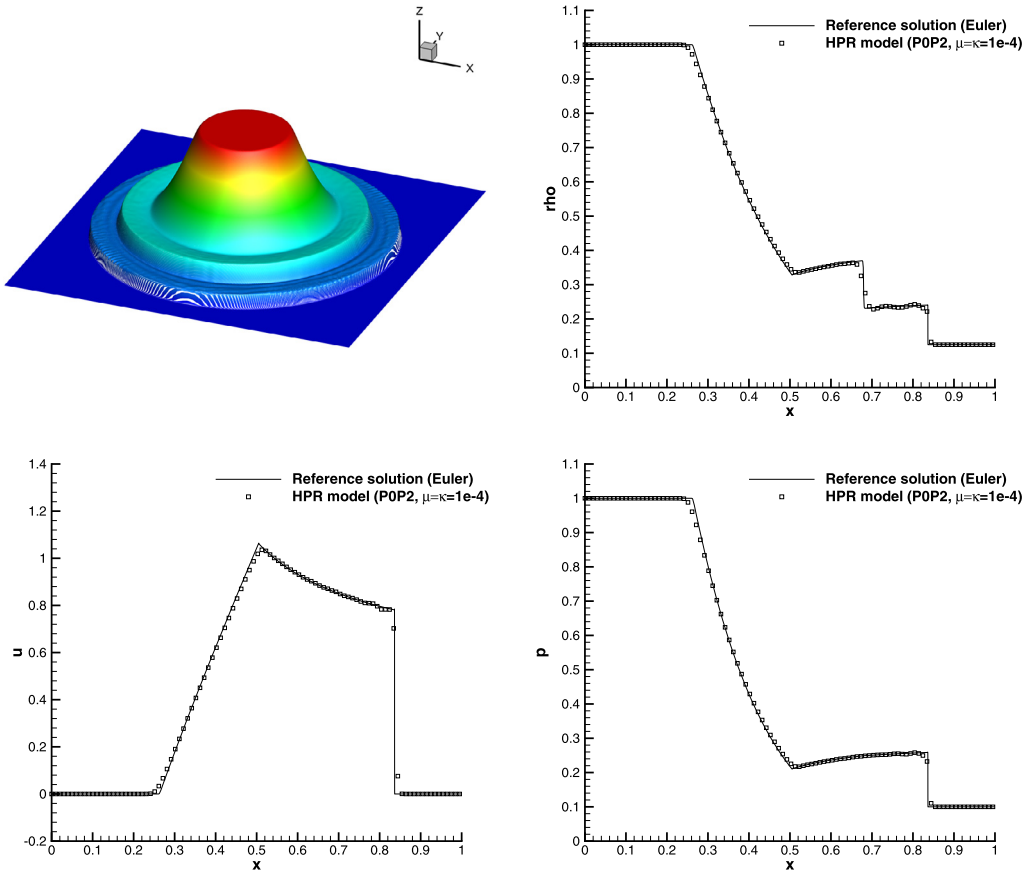

Fig. 2. Euler reference solution and numerical solution of the HPR model for the circular explosion problem obtained with an ADER–WENO finite volume scheme (P_0P_2) at a final time of $t = 0.2$ with $\mu = \kappa = 10^{-4}$. 3D view (top left), cut along the x-axis for density (top right), velocity u (bottom left) and pressure p (bottom right). (For interpretation of the colors in this figure, the reader is referred to the web version of this article.)

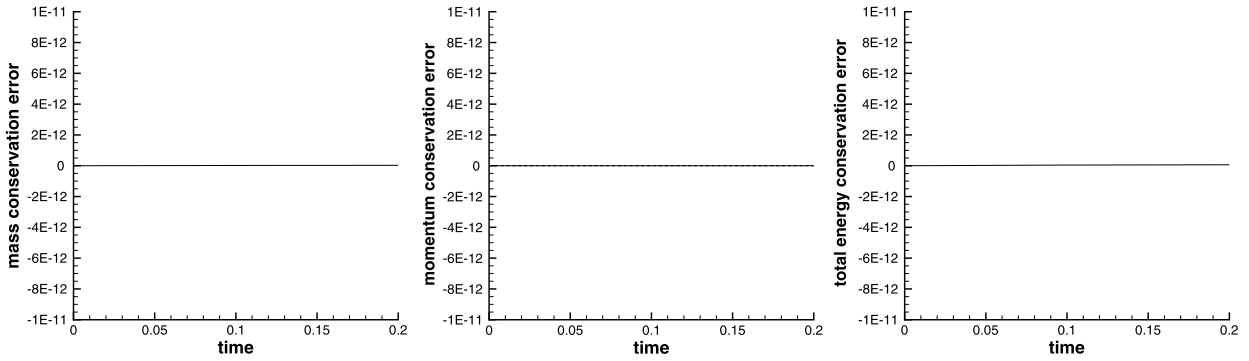

Fig. 3. Conservation error for mass (left), momentum (middle) and total energy (right) for the cylindrical explosion problem.

4.3. The first problem of Stokes

There are very few test problems for which an exact analytical solution of the unsteady Navier–Stokes equations is known. One of those is the first problem of Stokes [121], which consists of the time-evolution of an infinite incompressible shear layer. To get an almost incompressible behavior, we run the simulation at a low Mach number of $M = 0.1$. The computational domain is $\Omega = [-0.5; +0.5] \times [-0.05; +0.05]$, with periodic boundary conditions in y direction. At the boundaries in x direction the initial condition is imposed. The initial condition of the problem is given by $\rho = 1$, $u = 0$, $p = 1/\gamma$, $\boldsymbol{A} = \mathbf{I}$, $\mathbf{J} = 0$, while the velocity component v is $v = -v_0$ for $x < 0$ and $v = +v_0$ for $x \geq 0$. The physical parameters of this test problem are set to $v_0 = 0.1$, $\gamma = 1.4$, $c_v = 1$, $\rho_0 = 1$, $c_s = 1$ and $\alpha = \kappa = 0$. Simulations are performed with an ADER-DG

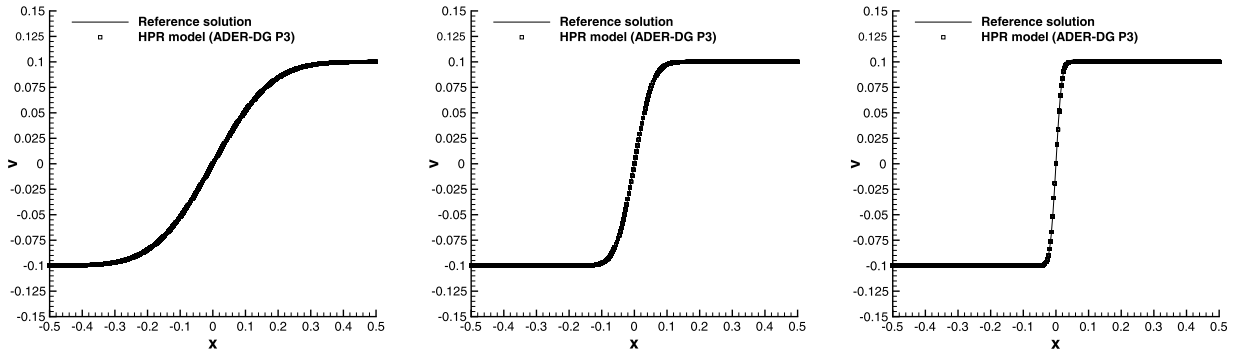

Fig. 4. Exact solution of the first problem of Stokes for the Navier–Stokes equations and numerical solution for the hyperbolic model of Peshkov and Romenski (HPR) obtained with an ADER-DG P_3P_3 scheme at a final time of $t = 1.0$ with different viscosities: $\mu = 10^{-2}$ (left), $\mu = 10^{-3}$ (middle), $\mu = 10^{-4}$ (right).

P_3P_3 scheme ($N = M = 3$) on a grid composed of 100×10 elements up to a final time of $t = 1$. The exact solution of the incompressible Navier–Stokes equations for the velocity component v is given by

$$v(x,t) = v_0 \mathrm{erf}\left(\frac{1}{2}\frac{x}{\sqrt{\mu t}}\right), \tag{77}$$

and serves as a reference solution for the HPR model. The comparison between the Navier–Stokes reference solution (77) and the numerical results obtained for the HPR model are presented in Fig. 4, where one can observe an excellent agreement between the two for various viscosities μ.

4.4. Laminar boundary layer over a flat plate

The laminar flow over a flat plate has been studied by Prandtl in his famous paper [111], where the concept of boundary layers was introduced in fluid mechanics for the first time. The boundary layer equations proposed by Prandtl were then solved for the first time in the special case of a laminar flow over a flat plate by Blasius in [17]. For an overview of boundary layer theory, the reader is referred to the well-known textbook by Schlichting and Gersten [121]. In the case of incompressible flow, the boundary layer equations take the following simple form:

$$f_{\eta\eta\eta} + f f_{\eta\eta} = 0, \qquad \text{with} \qquad f(0) = 0, \qquad f_\eta(0) = 0, \qquad \lim_{\eta\to\infty} f_\eta(\eta) = 1. \tag{78}$$

Here, $f = f(\eta)$ is the dimensionless stream function in the similarity variable $\eta = y\sqrt{\frac{U_\infty}{2\nu x}}$, while the axial flow velocity is given by $u = U_\infty f_\eta$. Nowadays, the boundary layer equation (78) can be solved by any standard ODE solver in combination with a classical shooting technique. In this paper, however, we use a shooting method based on the ODE solver proposed in [37], which is a special case of the space–time Galerkin predictor of the ADER approach, but applied to the simple case of a pure ODE.

The setup of the proposed numerical test case is as follows: the computational domain is $\Omega = [0; 1.5] \times [0; 0.4]$ and is discretized with 75×100 rectangular elements. At $y = 0$ we impose a no-slip wall boundary condition and the chosen Reynolds number of the flow is $\mathrm{Re} = 10^3$. The initial condition and the physical parameters for the computational setup are $\gamma = 1.4$, $\rho_0 = 1$, $c_v = 1$, $c_s = 8$, $\rho = 1$, $u = U_\infty = 1$, $v = V_\infty = 0$, $p = 100/\gamma$, $\boldsymbol{A} = \mathbf{I}$, $\mathbf{J} = 0$, $\alpha = \kappa = 0$ and $\mu = 10^{-3}$. The Mach number of this setup is therefore $M_\infty = 0.1$. At $x = 0$ the inflow boundary condition is given by the free stream data, i.e. by the initial condition. Simulations are run up to $t = 10$ using a third order ADER–WENO finite volume scheme ($N = 0$, $M = 2$).

In Fig. 5 the computational results obtained for the HPR model are shown, together with a 1D cut through the numerical solution at $x = 0.5$ and a comparison with the Blasius reference solution is made. A good agreement between the numerical solution of the HPR model and the Blasius solution can be noted, despite the fact that two completely different mathematical models have been used to obtain them. This confirms the validity of the HPR model in the stiff relaxation limit when $\tau_1 \to 0$, where it is able to accurately reproduce the known results from Navier–Stokes theory. For the sake of completeness, in Fig. 6 we show two of the components of the distortion tensor $\boldsymbol{A}$.

4.5. Hagen–Poiseuille flow in a duct

Here, we consider the steady flow of a viscous Newtonian fluid in a rectangular duct of length L and height h in the presence of a constant pressure gradient $\Delta p < 0$, and choosing the x-axis as the direction of motion. This test, referred to as the *Hagen–Poiseuille flow*, has a well known solution of the Navier–Stokes equations [91] with a parabolic velocity profile given by

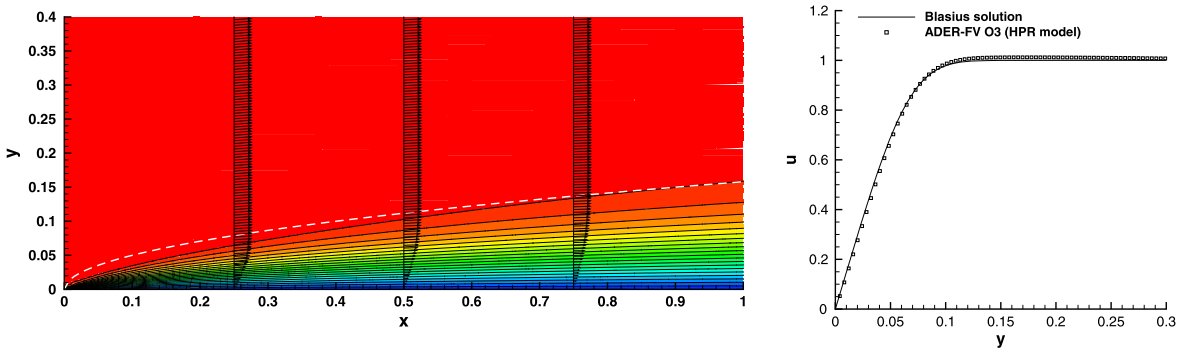

Fig. 5. Laminar boundary layer over a flat plate. Numerical solution for the hyperbolic model of Peshkov and Romenski (HPR) obtained with a third order ADER–WENO finite volume scheme at a final time of $t = 10.0$. Left: boundary layer thickness $\delta_{0.99}$ (dashed white line), velocity contours and some velocity profiles. Right: vertical cut through the velocity profile along the line $x = 0.5$ and comparison with the Blasius solution. (For interpretation of the colors in this figure, the reader is referred to the web version of this article.)

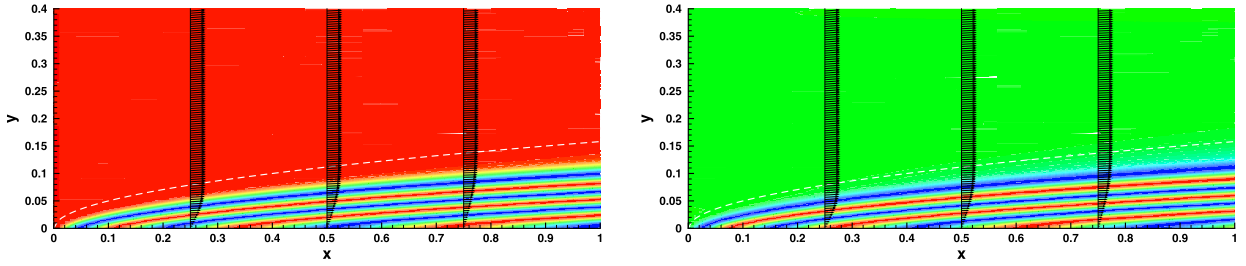

Fig. 6. Laminar boundary layer over a flat plate. Numerical solution for the hyperbolic model of Peshkov and Romenski (HPR) obtained with a third order ADER–WENO finite volume scheme at a final time of $t = 10.0$. 41 equidistant color contours in the interval $[-1, 1]$ for the distortion tensor component A_{11} (left) and A_{12} (right). (For interpretation of the references to color in this figure legend, the reader is referred to the web version of this article.)

$$v = \frac{1}{2}\frac{\Delta p}{L}\frac{\rho}{\mu} y(y-h). \tag{79}$$

Although Eqn. (79) has been derived for an incompressible fluid, we still expect to obtain a good numerical agreement with it, as long as our simulations are performed in the low Mach number regime. For that purpose, we use the following physical parameters and initial condition for our simulation: $\gamma = 1.4$, $\rho_0 = 1$, $c_v = 1$, $c_s = 8$, $p = 100/\gamma$, $u = v = 0$, $\boldsymbol{A} = \mathbf{I}$, $\mathbf{J} = 0$, $\alpha = \kappa = 0$ and $\mu = 10^{-2}$. The pressure gradient is imposed between the left inflow and the right outlet as $\Delta p = -4.8$, leading to a mean flow velocity of $\bar{u} = 1$ and a maximum flow velocity of $u_{\max} = 1.5$. We have solved the problem in the computational domain $\Omega = [0, 10] \times [0, 0.5]$ covered by 100×50 cells, applying a third order ADER–WENO finite volume scheme ($N = 0$, $M = 2$) to the HPR model. The computational results are shown at time $t = 10$ in Fig. 7, referring to a Reynolds number of $\mathrm{Re} = \frac{\bar{u}h\rho}{\mu} = 50$. In the top panel the laminar flow is very well reproduced, with only a moderate increase of the flow velocity from $x = 0$ to $x = 10$. In the bottom panel we perform a direct comparison to the Navier–Stokes reference solution, by plotting the velocity across the flow as measured at $x = 5$. We conclude that the HPR model can successfully solve this classical test of laminar, steady viscous flow in a duct.

4.6. The lid-driven cavity

The lid-driven cavity is a classical benchmark problem for numerical methods applied to the incompressible Navier–Stokes equations, see [65,128]. However, it can also be used for compressible flow solvers in the low Mach number regime, see [42]. The computational domain is the box $\Omega = [-0.5, 0.5] \times [-0.5, 0.5]$, which is initialized with a density of $\rho = 1$, a velocity of $u = v = 0$ and a pressure of $p = 100/\gamma$. The rest of the parameters is set to $\gamma = 1.4$, $c_v = 1$, $c_s = 8$, $\rho_0 = 1$, $\boldsymbol{A} = \mathbf{I}$ and $\mathbf{J} = 0$. The dynamic viscosity is chosen as $\mu = 10^{-2}$, while heat conduction is neglected, i.e. $\alpha = \kappa = 0$. The flow is driven by the upper boundary, whose velocity is set to $\mathbf{v} = (1, 0)$. On the other three boundaries, a no-slip wall boundary condition $\mathbf{v} = 0$ is imposed. We run a third order ADER–WENO finite volume scheme ($N = 0$, $M = 2$) on a grid composed of 100×100 elements until a final time of $t = 10$. The reference Mach number of this test case with respect to the speed of the lid is $M = 0.1$. The computational results are presented in Fig. 8, where also a comparison with the Navier–Stokes reference solution of Ghia et al. [65] is shown. We note a very good agreement between the numerical solution of the HPR model and the solution of the incompressible Navier–Stokes equations. In the bottom panels of Fig. 8, we plot two components of the distortion tensor $\boldsymbol{A}$, which is very useful to visualize the main structures of the flow. We would like to stress that the lid-driven cavity problem is challenging for numerical methods applied to the Navier–Stokes equations, since the

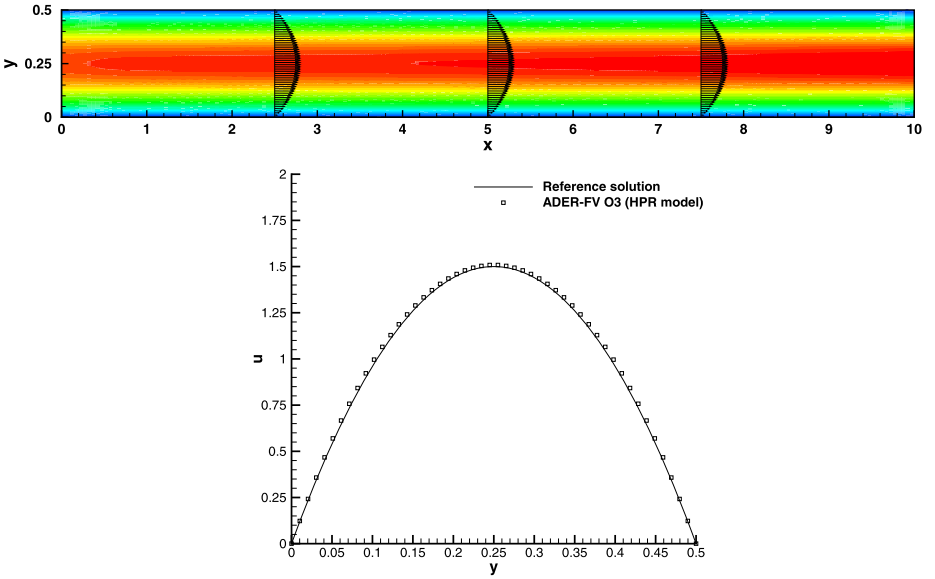

Fig. 7. Steady laminar Hagen–Poiseuille flow in a duct at $\mathrm{Re} = 50$. Exact solution of the Navier–Stokes equations and numerical solution for the hyperbolic model of Peshkov and Romenski (HPR) at a final time of $t = 10.0$ obtained with a third order ADER–WENO finite volume scheme. Axial velocity contours with some velocity profiles (top) and 1D cut along the y axis at $x = 5$ (bottom). (For interpretation of the colors in this figure, the reader is referred to the web version of this article.)

boundary conditions produce a singularity of the velocity gradient in the corners, while the fluxes in the present hyperbolic formulation are well defined even for the corners.

4.7. Double shear layer

The numerical scheme is now applied to a double shear layer benchmark problem, see [14,129], which contains a high initial velocity gradient. The computational domain is defined as $\Omega = [0, 1]^2$ and periodic boundary conditions are imposed everywhere. As initial condition we consider the following perturbed double shear layer profile:

$$u = \begin{cases} \tanh\left(\tilde{\rho}(y - 0.25)\right), & \text{if } y \leq 0.5, \\ \tanh\left(\tilde{\rho}(0.75 - y)\right), & \text{if } y > 0.5, \end{cases} \tag{80}$$

$$v = \delta \sin(2\pi x), \qquad \rho = 1, \qquad p = \frac{100}{\gamma}, \tag{81}$$

where $\tilde{\rho}$ is a parameter that determines the slope of the shear layer; and δ is the amplitude of the initial perturbation. For the present test we set $\delta = 0.05$; $\tilde{\rho} = 30$; $\nu = \mu/\rho_0 = 2 \cdot 10^{-4}$. The other parameters are $\gamma = 1.4$, $\rho_0 = 1$, $c_v = 1$, $c_s = 8$, $\boldsymbol{A} = \mathbf{I}$, $\mathbf{J} = 0$, $\alpha = \kappa = 0$. Simulations are carried out up to a final time of $t = 1.8$ using a fourth order ADER–WENO finite volume scheme ($N = 0$, $M = 3$) on a grid composed of 200×200 cells. In Fig. 9 the computational results obtained with the HPR model are compared with a numerical reference solution based on the solution of the incompressible Navier–Stokes equations. We can note an excellent agreement between the two. The reference solution has been obtained with the staggered space–time discontinuous Galerkin finite element method recently proposed in [129]. In both models, the two thin shear layers evolve into several vortices, as observed in [14], and overall the small flow structures seem to be relatively well resolved also at the final time $t = 1.8$. In Fig. 10 we plot the time evolution of the distortion tensor component A_{12}. One can again observe that the components of the tensor $\boldsymbol{A}$ are excellent candidates for *flow visualization*, since they reveal even more details of the flow structures than the vorticity plotted in the previous Fig. 9. The main advantage here is that in the framework of the HPR model, the tensor $\boldsymbol{A}$ is one of the main variables already contained in the state vector $\mathbf{Q}$ of the governing PDE system, while vorticity needs to be computed from the velocity field via some post-processing technique.

4.8. Von Karman vortex street

In this section, we solve a test problem used in [101] and [37] in the context of sound generation by a von Karman vortex street that is shed behind a circular cylinder. The circular obstacle has a diameter of $d = 1$, the Reynolds number based on the diameter is $\mathrm{Re} = \frac{\rho_0 u_0 d}{\mu} = 150$ and the Mach number of the flow is $M_0 = u_0/c_0 = 0.2$. We use $\gamma = 1.4$, $c_v = 1$, $\rho_0 = 1$, $c_s = 0.8$ and $\alpha = \kappa = 0$. The initial condition for the HPR model is $\rho = \rho_0$, $u = u_0 = 0.2$, $v = 0$, $p = p_0 = 1/\gamma$, $\boldsymbol{A} = \mathbf{I}$ and $\mathbf{J} = 0$. Computations are performed with a third order ADER WENO finite volume scheme ($N = 0$, $M = 2$) on an unstructured

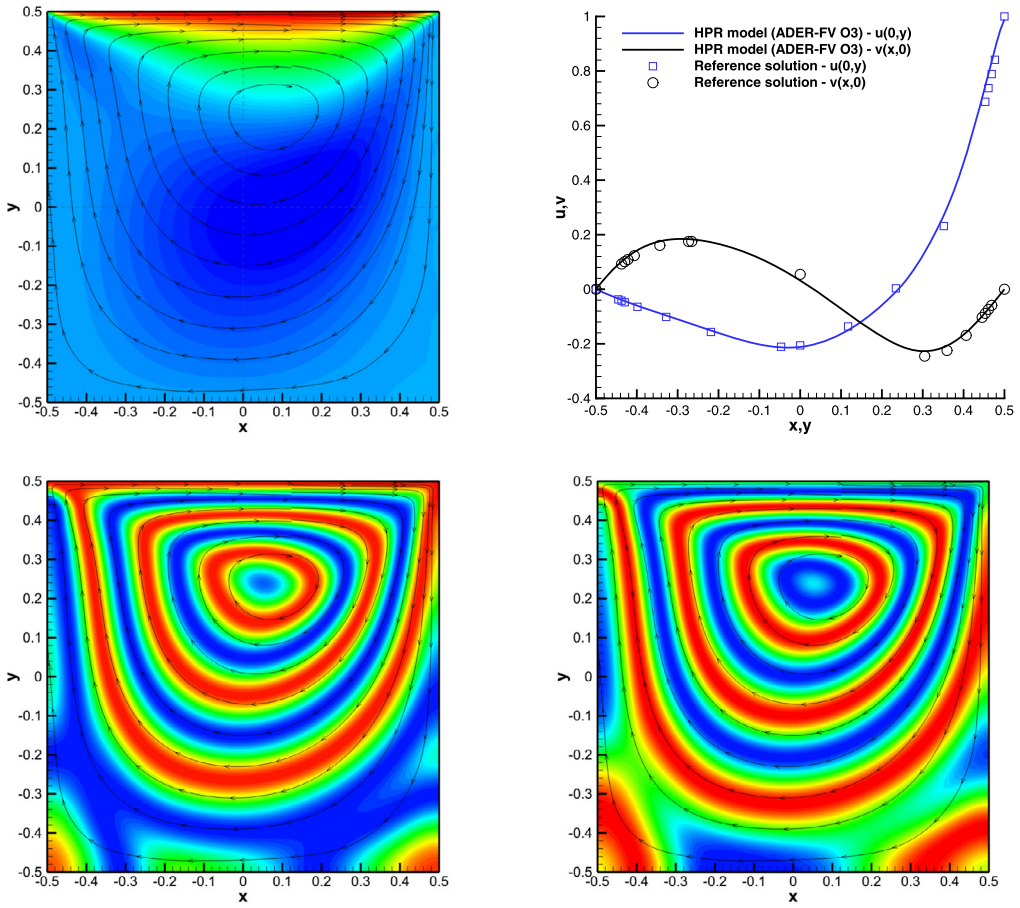

Fig. 8. Lid driven cavity at $\mathrm{Re} = 100$. Reference solution by Ghia et al. [65] and numerical solution for the hyperbolic model of Peshkov and Romenski (HPR) at a final time of $t = 10.0$ obtained with a third order ADER–WENO finite volume scheme. Streamlines and u velocity contours (top left) and 1D cuts along the x and the y axis (top right). The components of the distortion tensor are shown in the bottom row, with 41 equidistant contour colors in the interval $[-1, 1]$: A_{11} (bottom left) and A_{12} (bottom right). (For interpretation of the references to color in this figure legend, the reader is referred to the web version of this article.)

triangular mesh [47,48,52] that consists of 145 646 triangles. The computational domain is a circle with diameter $D = 200$ and the simulation is run until a final time of $t = 950$. A plot of the distortion tensor component A_{12} in the vicinity of the cylinder is depicted in Fig. 11. As already stated in the previous examples, the tensor $\boldsymbol{A}$ turns out to be very useful for *flow visualization*, since all details of the flow structure can be easily recognized in Fig. 11. An instantaneous plot at $t = 500$ of the sound pressure field generated by this unsteady flow is illustrated in Fig. 12 and agrees reasonably well with those computed in [101,37]. The time history of the sound pressure level (SPL) at the point $x = (0, 50)$ is also presented in Fig. 12. From the analysis of the SPL signal of our numerical simulations we obtain a Strouhal number of $\mathrm{St} = \frac{fd}{u_0} = 0.175$, which is in reasonable agreement with the value of $\mathrm{St} = 0.183$ found by Müller [101] and with the value of $\mathrm{St} = 0.182$ reported in [37].

4.9. Compressible mixing layer

Next, we simulate the behavior of an unsteady compressible mixing layer, following partially the setup presented in [33,2,62,37]. For $y \to \infty$ the limit of the axial flow velocity is $u_\infty = 0.5$, while for $y \to -\infty$ the axial velocity component tends to $u_{-\infty} = 0.25$. Here, we use the simplified initial condition for the flow velocity

$$u_0 = \frac{1}{8}\tanh(2y) + \frac{3}{8}, \qquad v_0 = 0, \tag{82}$$

while the initial condition for the other flow variables is simply given by $\rho = 1$, $p = p_0 = 1/\gamma$, $\boldsymbol{A} = \mathbf{I}$ and $\mathbf{J} = 0$. The vorticity thickness at the inflow, with respect to which all lengths are made dimensionless, is

$$\theta = \frac{u_\infty - u_{-\infty}}{\max\left(\left.\frac{\partial u}{\partial y}\right|_{x=0}\right)} := 1, \tag{83}$$

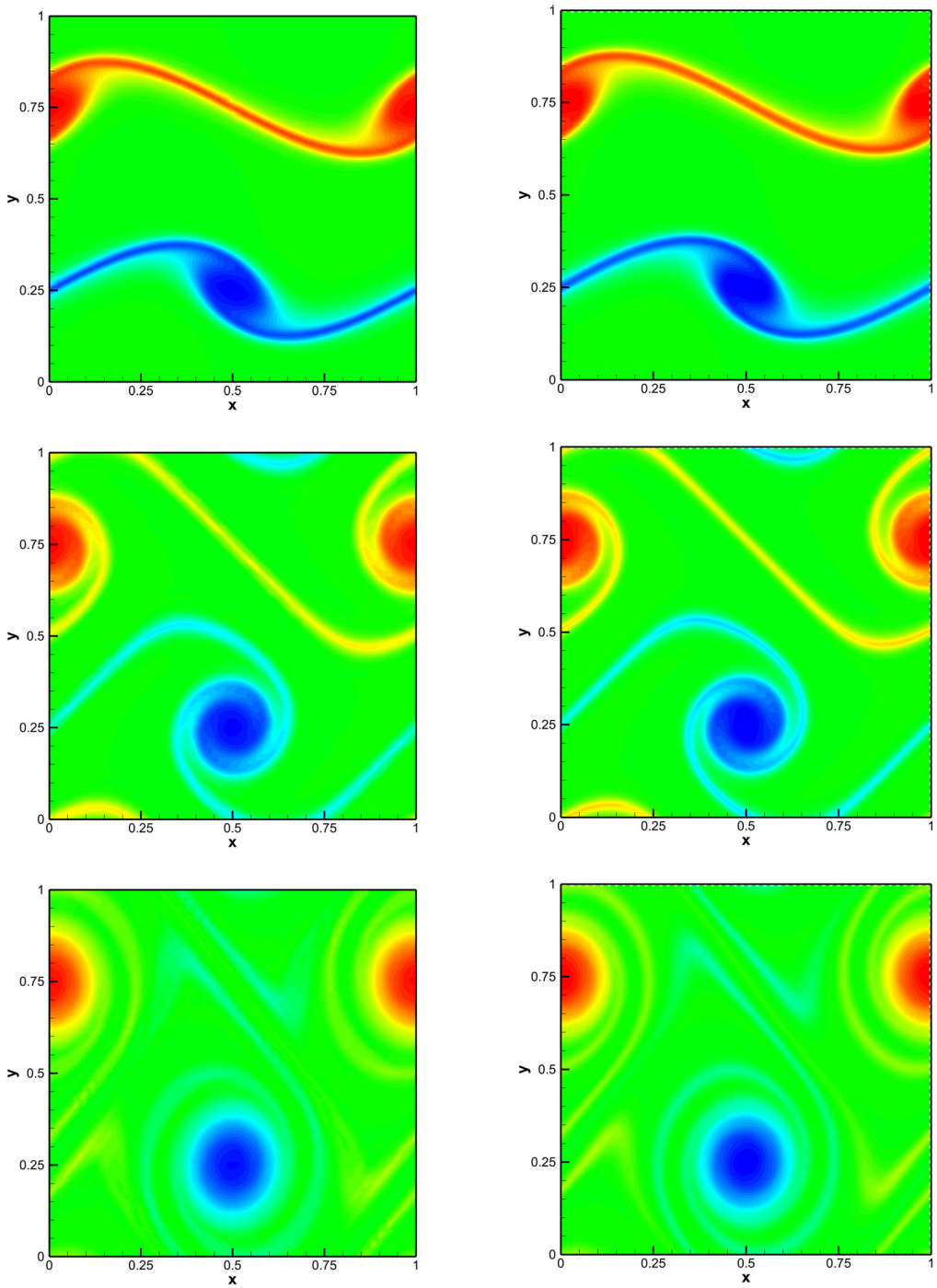

Fig. 9. Vorticity contours for the double shear layer with a viscosity of $\nu = 2 \cdot 10^{-4}$. Right: numerical solution of the incompressible Navier–Stokes equations obtained with the staggered semi-implicit space–time DG scheme of Tavelli and Dumbser [128,129]. Left: numerical solution for the hyperbolic model of Peshkov and Romenski (HPR) at times $t = 0.8$, $t = 1.2$, $t = 1.8$ from top to bottom obtained with a fourth order ADER–WENO finite volume scheme. (For interpretation of the colors in this figure, the reader is referred to the web version of this article.)

and the Reynolds number based on this vorticity thickness is

$$\mathrm{Re}_\theta = \frac{\rho_0 u_\infty \theta}{\mu} = 500. \tag{84}$$

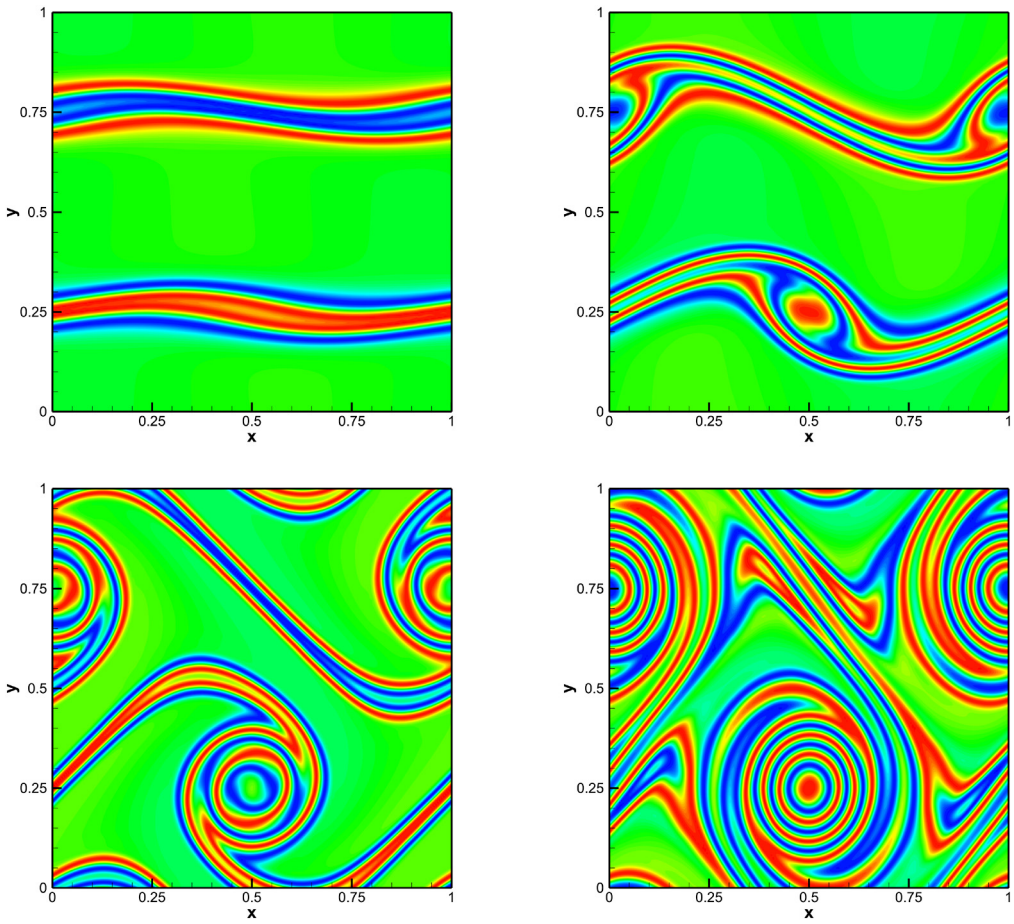

Fig. 10. Double shear layer: 41 equidistant contour colors in the interval $[-1, 1]$ for component A_{12} of the distortion tensor of the HPR model at times $t = 0.4$, $t = 0.8$, $t = 1.2$ and $t = 1.8$. (For interpretation of the references to color in this figure legend, the reader is referred to the web version of this article.)

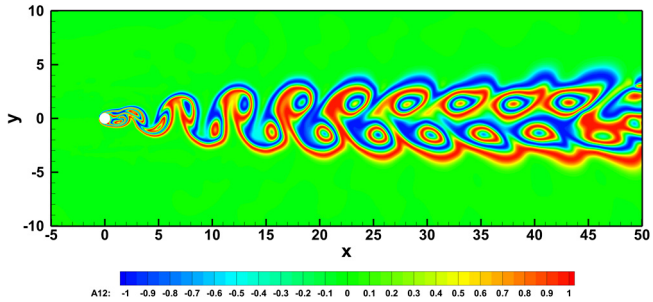

Fig. 11. Flow around a circular cylinder ($\mathrm{Re} = 150$) at time $t = 500$. The quantity A_{12} is shown via 41 equidistant contour levels in the interval $[-1, 1]$. The typical von Karman vortex street is clearly visible. (For interpretation of the colors in this figure, the reader is referred to the web version of this article.)

Thus, the parameters of the HPR model are set to $\gamma = 1.4$, $c_v = 2.5$, $\rho_0 = 1$, $c_s = 0.8$, $\mu = 10^{-3}$, $\alpha = \kappa = 0$, i.e. heat conduction is again neglected in this example. At the inflow ($x = 0$), the flow quantities ρ, u, v and p are perturbed as follows: $\rho(0, y, t) = \rho_0 + 0.05\,\delta$, $u(0, y, t) = u_0 + \delta$, $v(0, y, t) = v_0 + 0.6\,\delta$ and $p(0, y, t) = p_0 + 0.2\,\delta$, with

$$\delta = -10^{-3} \exp(-0.25 y^2) \left(\cos(\omega t) + \cos\left(\frac{1}{2}\omega t - 0.028\right) + \cos\left(\frac{1}{4}\omega t + 0.141\right) + \cos\left(\frac{1}{8}\omega t + 0.391\right)\right) \tag{85}$$

and the fundamental frequency of the mixing layer $\omega = 0.3147876$. The computational domain is defined by $\Omega = [0, 400] \times [-50, 50]$ and is covered by a Cartesian grid of 1600×800 elements. The final simulation time is set to $t = 1596.8$. The computational results obtained with the HPR model are depicted in Fig. 13, where also two numerical reference solutions based on the solution of the compressible Navier–Stokes equations, see [33,37], are shown. Overall, we observe a reasonable

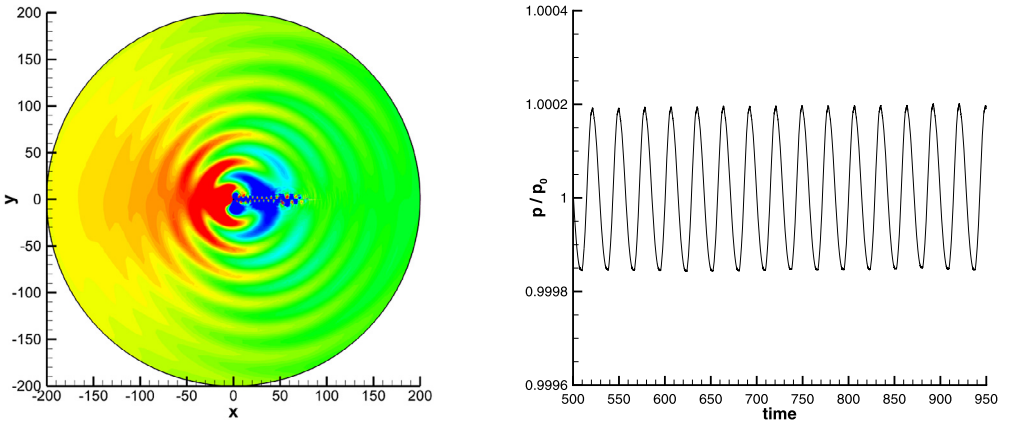

Fig. 12. Flow around a circular cylinder at Re = 150. Pressure color contours at $t = 500$, indicating the sound field generated by the unsteady vortex street (left) and sound pressure level (SPL) p/p_0 registered at the point $x = (0, 50)$ (right). The corresponding Strouhal number of the signal is St = 0.175. (For interpretation of the references to color in this figure legend, the reader is referred to the web version of this article.)

qualitative agreement between the HPR model and the Navier–Stokes reference solution. In the last row of Fig. 13 we show again a component of the tensor $\boldsymbol{A}$, which seems to reveal the vortex flow structures of the mixing layer even better and in a clearer way than the usual vorticity. This underlines again the potential of using $\boldsymbol{A}$ for the purpose of *flow visualization*.

4.10. 2D Taylor–Green vortex

Another typical test problem used for the verification of numerical methods for the incompressible Navier–Stokes equations is the Taylor–Green vortex problem, which is another one of the rare examples where an exact analytical solution of the unsteady Navier–Stokes equations is known. In two space dimensions, the solution reads

$$u(x, y, t) = \sin(x)\cos(y)e^{-2\nu t}, \tag{86}$$

$$v(x, y, t) = -\cos(x)\sin(y)e^{-2\nu t}, \tag{87}$$

$$p(x, y, t) = C + \frac{1}{4}(\cos(2x) + \cos(2y))e^{-4\nu t}. \tag{88}$$

The computational domain is $\Omega = [0, 2\pi]^2$ with four periodic boundaries everywhere. We carry out the numerical simulations based on the HPR model up to a final time of $t = 10$, using a fourth order ADER-DG P_3P_3 scheme ($N = M = 3$) on a computational grid composed of 50×50 elements. For the HPR model, the following set of parameters has been chosen: $\gamma = 1.4$, $\rho_0 = 1$, $\mu = 10^{-2}$, $c_v = 1$, $c_s = 10$, $\alpha = \kappa = 0$. The initial conditions for the velocity and the pressure are given by (86)–(88), where the additive constant in the pressure field is set to $C = 100/\gamma$. The distortion tensor and the heat flux are initialized as usual with $\boldsymbol{A} = \mathbf{I}$ and $\mathbf{J} = 0$.

The computational results are depicted in Fig. 14, where also a comparison with the exact solution of the incompressible Navier–Stokes equations is shown. Overall, one can note an excellent agreement between the HPR model and the reference solution, both for velocity and pressure. The distortion tensor component A_{11} is also drawn in Fig. 14 and reveals the vortex structures of the flow.

4.11. 3D Taylor–Green vortex

We now solve the Taylor–Green vortex problem again, but this time in three space dimensions. The computational domain is the box $\Omega = [-\pi, \pi]^3$, with six periodic boundary conditions. For large times and large Reynolds numbers, the 3D Taylor–Green vortex is a classical example for the development of flow structures with smaller and smaller spatial scales, up to the onset of turbulence. The problem has been widely studied in literature and a reference solution is available via a direct numerical simulation (DNS) provided in the paper of Brachet et al. [22]. To obtain a low Mach number compressible flow, the following initial condition is chosen, see also [124]: $\rho = \rho_0 = 1$, $p_0 = 10^2/\gamma$, $\boldsymbol{A} = \mathbf{I}$, $\mathbf{J} = 0$, and

$$u(\mathbf{x}, 0) = \sin(x)\cos(y)\cos(z),$$

$$v(\mathbf{x}, 0) = -\cos(x)\sin(y)\cos(z),$$

$$z(\mathbf{x}, 0) = 0,$$

$$p(\mathbf{x}, 0) = p_0 + \frac{\rho_0}{16}\left((\cos(2z) + 2)(\cos(2x) + \cos(2y)) - 2.0\right). \tag{89}$$

With the choice of p_0, the maximum Mach number of the flow at the initial time is $M = 0.1$. The numerical simulations are carried out for two different Reynolds numbers with the full HPR model in three space dimensions up to a final time of

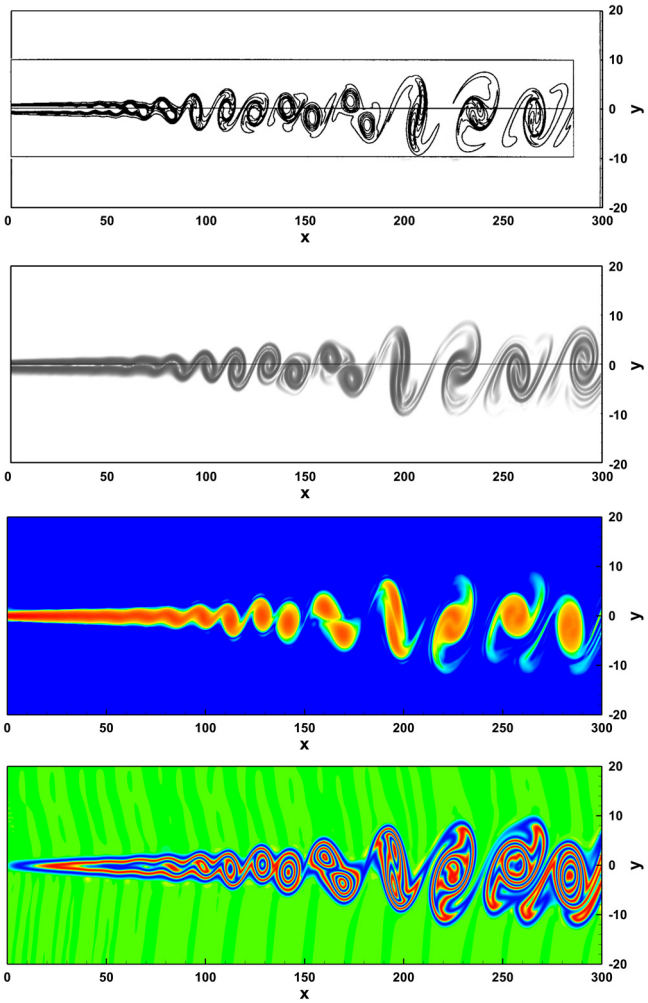

Fig. 13. Compressible mixing layer at $\mathrm{Re} = 500$ at a final time of $t = 1596.8$. The reference solutions have been obtained by solving the compressible Navier–Stokes equations with a compact finite difference scheme, see Colonius and Moin [33] (top row) and with a sixth order $P_N P_M$ scheme ($P_3 P_5$), see Dumbser [37] (second row). The numerical solution obtained with a third order ADER–WENO finite volume scheme ($N = 0$, $M = 2$) for the hyperbolic model of Peshkov and Romenski (HPR) is shown at the bottom. In rows 1–3 the vorticity magnitude is plotted, while in the fourth row (for the HPR solution) the quantity A_{12} is shown via 41 equidistant contour levels in the interval $[-1, 1]$. (For interpretation of the colors in this figure, the reader is referred to the web version of this article.)

$t = 10$, using a third order ADER–WENO finite volume scheme ($N = 0$, $M = 2$), on a computational grid composed of 224^3 elements. For the HPR model, the following set of parameters has been chosen: $\gamma = 1.4$, $\rho_0 = 1$, $\mu = 1/\mathrm{Re}$, $c_v = 2.5$, $c_s = 8$, $\alpha = 1$, $T_0 = 1$, $\kappa = \gamma c_v \mu$, hence the resulting Prandtl number is $\mathrm{Pr} = 1$. An important quantity for the comparison with existing DNS data is the kinetic energy dissipation rate

$$\frac{dk}{dt} = \frac{d}{dt}\left(\frac{1}{|\Omega|} \int_{\Omega} \frac{1}{2} \rho \mathbf{v}^2 d\mathbf{x} \right). \tag{90}$$

The computational results obtained for the kinetic energy dissipation rate are depicted in Fig. 15 for two Reynolds numbers, $\mathrm{Re} = 100$ and $\mathrm{Re} = 200$, where we can note a good agreement with the DNS reference data of Brachet et al. for $\mathrm{Re} = 100$, while the employed third order ADER–WENO finite volume scheme seems to be too dissipative for $t > 6$ in the case $\mathrm{Re} = 200$. Further systematic studies of this important test problem will be carried out in the future, using substantially refined grids and higher order polynomial degrees in the numerical scheme in order to identify the cause for the observed deviation of the HPR model from the Navier–Stokes reference solution for higher Reynolds numbers. A 3D view of the time evolution of the developing small-scale flow structures is shown in Fig. 16 at the aid of the component A_{11} of the distortion tensor $\boldsymbol{A}$, while all elements of $\boldsymbol{A}$ are depicted at the final time $t = 10$ in Fig. 17.

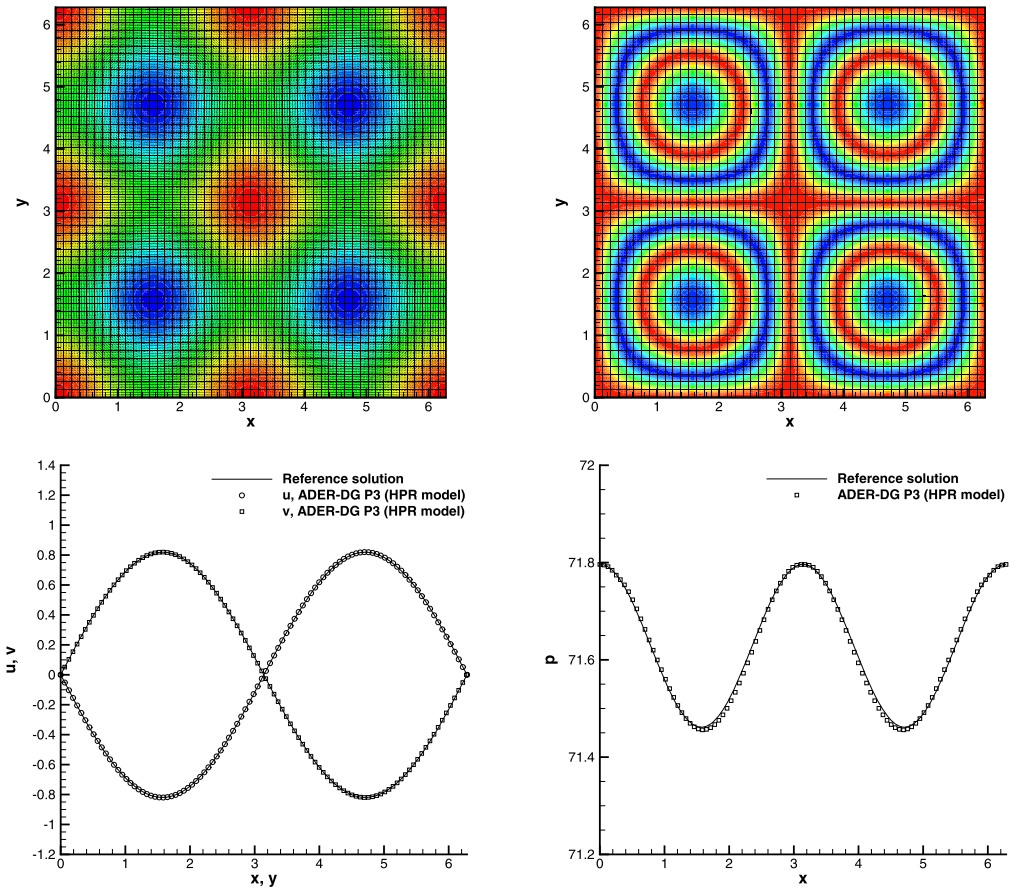

Fig. 14. Taylor–Green vortex with a viscosity of $\nu = 10^{-2}$. Exact solution of the Navier–Stokes equations and numerical solution for the hyperbolic model of Peshkov and Romenski (HPR) at a final time of $t = 10.0$ obtained with an ADER-DG P_3P_3 scheme ($N = M = 3$). Pressure contours and velocity vectors (top left). 41 color contours in the interval $[-1, 1]$ of the distortion tensor component A_{11} (top right). 1D cuts along the x and the y axis for velocity components u and v (bottom left) and 1D cut along the x-axis for the pressure p. (For interpretation of the references to color in this figure legend, the reader is referred to the web version of this article.)

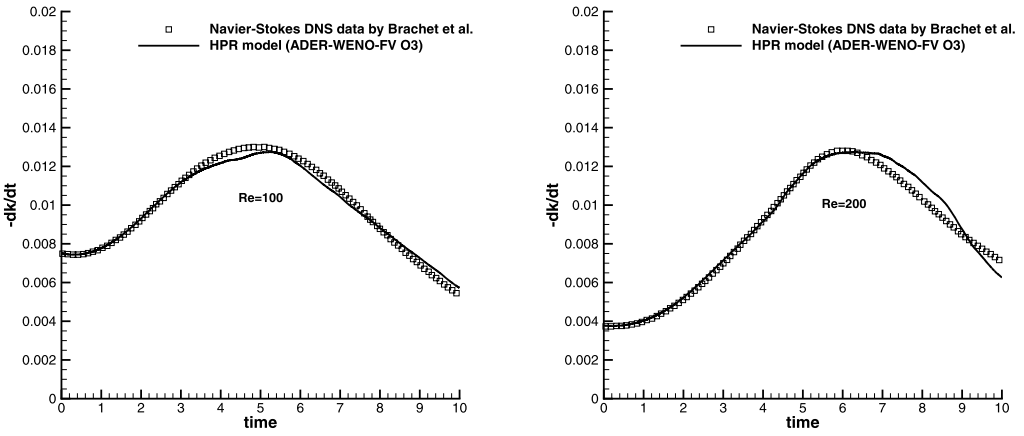

Fig. 15. Time evolution of the kinetic energy dissipation rate for the 3D Taylor–Green vortex obtained at a Reynolds number of $\mathrm{Re} = 100$ (left) and $\mathrm{Re} = 200$ (right). The reference solution is given by the DNS data of Brachet et al. [22] for the incompressible Navier–Stokes equations, which is compared with the numerical solution for the hyperbolic model of Peshkov and Romenski (HPR) until a final time of $t = 10$ using a third order P_0P_2 ADER–WENO finite volume scheme ($N = 0$, $M = 2$) on a Cartesian grid of 224^3 elements.

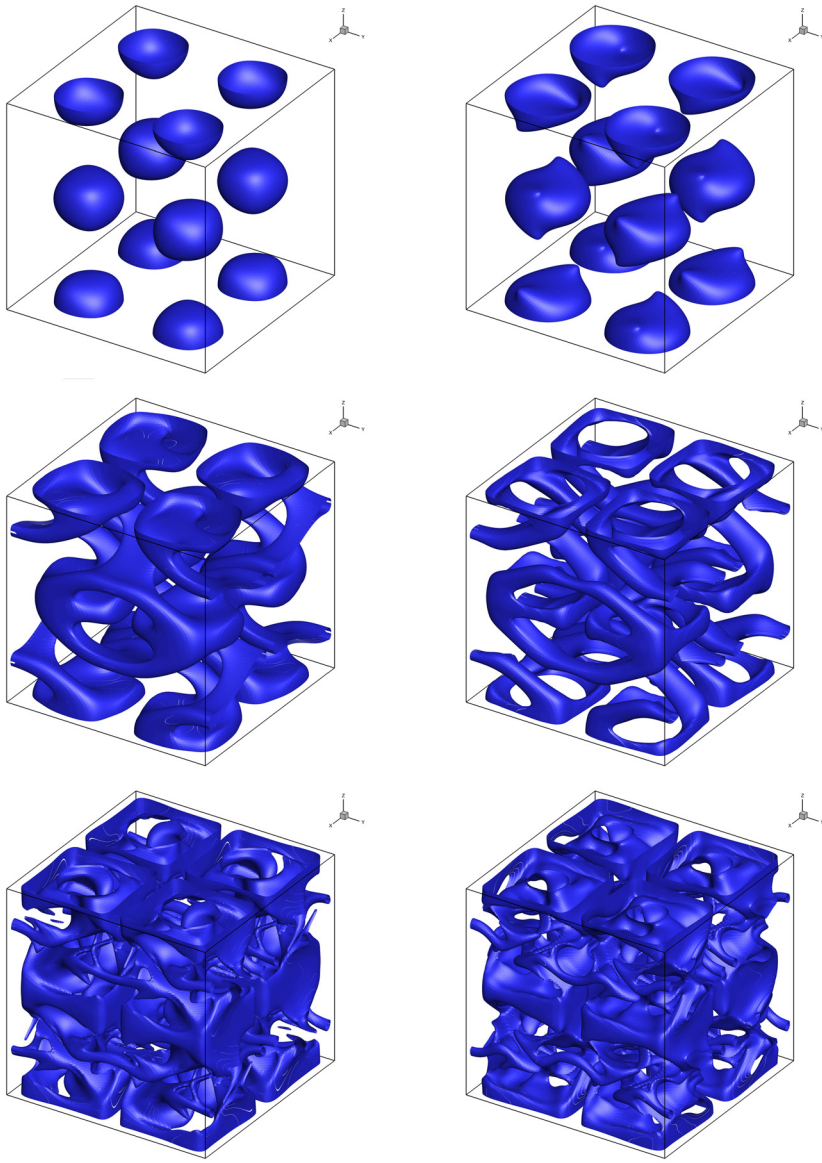

Fig. 16. Isocontour surfaces of the tensor component A_{11} obtained with the first order hyperbolic model of Peshkov and Romenski for the 3D Taylor–Green vortex (Re = 200) for different intermediate times: $t = 1$ (top left), $t = 2$ (top right), $t = 3$ (center left) and $t = 4$ (center right), $t = 8$ (bottom left) and $t = 10$ (bottom right).

4.12. Heat conduction in a gas

Here, we solve a simple test problem dominated by the effect of heat conduction. The initial condition for the flow variables is $\rho = 2$ for $x < 0$ and $\rho = 0.5$ for $x \geq 0$, while $u = v = 0$ and $p = 1$ everywhere. Furthermore, $\boldsymbol{A} = \mathbf{I}$ and $\mathbf{J} = 0$ at the initial time. The parameters of the HPR model are defined by $\gamma = 1.4$, $\rho_0 = 1$, $c_v = 2.5$, $c_s = 1$, $\mu = 10^{-2}$, $\alpha = 2$, $T_0 = 1$ and $\kappa = 10^{-2}$. The computational domain is $\Omega = [-0.5, 0.5] \times [-0.1, 0.1]$ and simulations are carried out with an ADER-DG P_3P_3 scheme ($N = M = 3$) until $t = 1.0$ on a grid composed of 100×5 elements. In Fig. 18 a 1D cut through the computational results at $y = 0$ is shown for the first order HPR model, together with a Navier–Stokes reference solution computed with an ADER-DG scheme [37] on the same grid. We note an excellent agreement between the two models. Furthermore, in Table 2 we list the computational time (wallclock time) and the number of time steps needed to reach the final simulation time in the context of ADER finite volume and ADER-DG schemes using two different grid resolutions for both, the HPR model and for the compressible Navier–Stokes equations. With the above parameters, the explicit discretization of the compressible Navier–Stokes equations already runs into the parabolic time step restriction, which leads to a quadratic decrease of the time step size with mesh refinement and thus to a significant increase in computational time. Compared to the finite volume case, the situation is even worse for DG methods, where the discretization of the HPR model does not only require

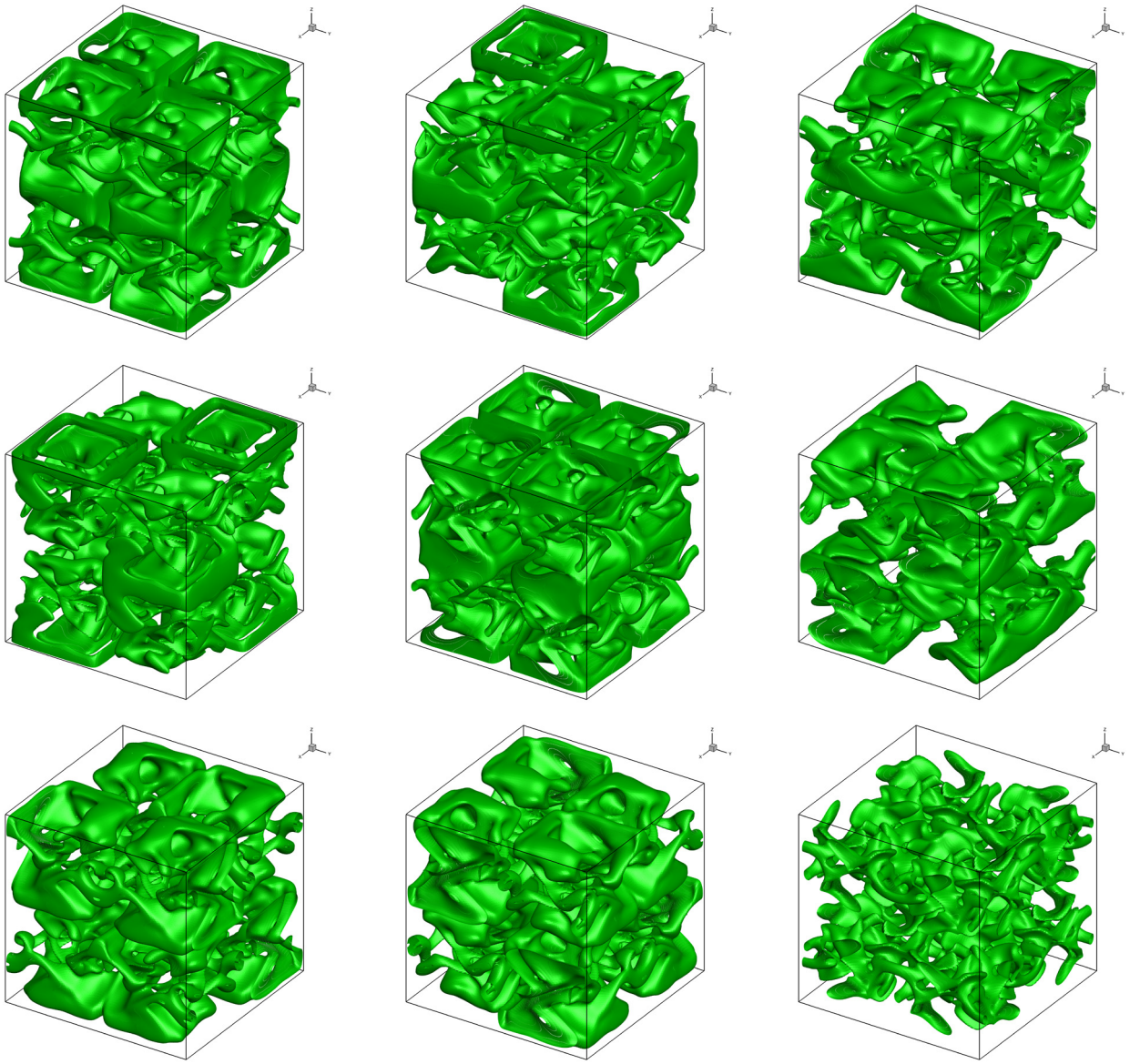

Fig. 17. Isocontour surfaces of value −0.5 of all components of the tensor $\boldsymbol{A}$ obtained with the first order hyperbolic model of Peshkov and Romenski for the 3D Taylor–Green vortex (Re = 200) at the final time $t = 10$. Component A_{ik} is shown in row i and column j of this figure.

Table 2
CPU time comparison for the heat conduction problem using the Navier–Stokes equations and the first order HPR model.

Mesh	Navier–Stokes equations		HPR model	
	Time steps	CPU time	Time steps	CPU time
ADER–WENO finite volume scheme (P_0P_2)				
100	1587	18.7	461	42.7
200	5535	112.2	922	144.8
ADER-DG scheme (P_3P_3)				
100	87 080	2317.2	4554	651
200	340 646	18 476	9104	2437

much less time steps, but also less CPU time than the discretization of the compressible Navier–Stokes equations. We think that these results might be relevant for those readers who are interested in the discretization of viscous compressible flows with heat conduction using explicit time integration schemes.

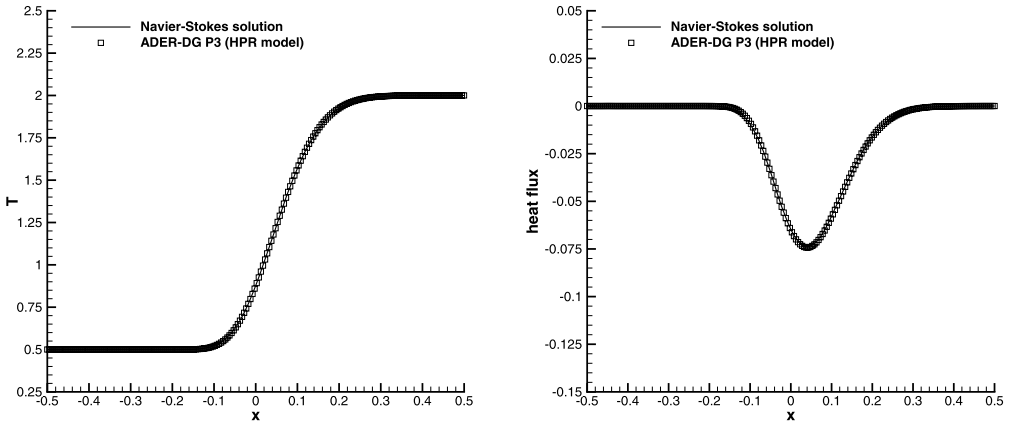

Fig. 18. Heat conduction test problem at a final time of $t = 1.0$. Temperature distribution (left) and heat flux (right). For the Navier–Stokes solution, the classical Fourier heat flux $q_1 = -\kappa T_x$ is shown, while for the first order HPR model, we plot $q_1 = \alpha^2 J_1 T$.

4.13. Viscous shock profile

The numerical test problems solved so far considered only either low Mach number flows, or at most weakly compressible flows. However, the first order HPR model is also valid in the case of supersonic viscous flows. Therefore, in this section we solve the problem of an isolated viscous shock wave propagating into a medium at rest with a shock Mach number of $M_s > 1$. In the case of a Prandtl number of $\mathrm{Pr} = 0.75$, there exists an exact traveling wave solution of the compressible Navier–Stokes equation that was first found by Becker [13] in 1923. In the following, we briefly recall the exact solution of Becker, where the indices "0" and "1" denote the upstream and the post-shock states, respectively.

For the special case of a *stationary shock wave* at Prandtl number $\mathrm{Pr} = 0.75$ and constant viscosity, the compressible Navier–Stokes equations can be reduced to one single ordinary differential equation (ODE) that can be solved analytically. The exact solution for the dimensionless velocity $\bar{u} = \frac{u}{M_s c_0}$ of this stationary shock wave is then given by the root of the following equation, see [13,20]:

$$\frac{|\bar{u}-1|}{|\bar{u}-\lambda^2|^{\lambda^2}} = \left|\frac{1-\lambda^2}{2}\right|^{(1-\lambda^2)} \exp\left(\frac{3}{4}\mathrm{Re}_s \frac{M_s^2-1}{\gamma M_s^2} x\right), \tag{91}$$

with

$$\lambda^2 = \frac{1+\frac{\gamma-1}{2}M_s^2}{\frac{\gamma+1}{2}M_s^2}. \tag{92}$$

From eqn. (91) one obtains the dimensionless velocity $\bar{u}$ as a function of x. The form of the viscous profile of the dimensionless pressure $\bar{p} = \frac{p-p_0}{\rho_0 c_0^2 M_s^2}$ is given by the relation

$$\bar{p} = 1 - \bar{u} + \frac{1}{2\gamma}\frac{\gamma+1}{\gamma-1}\frac{(\bar{u}-1)}{\bar{u}}(\bar{u}-\lambda^2). \tag{93}$$

Finally, the profile of the dimensionless density $\bar{\rho} = \frac{\rho}{\rho_0}$ is found from the integrated continuity equation: $\bar{\rho}\bar{u} = 1$. In order to obtain an unsteady shock wave traveling into a medium at rest, it is sufficient to superimpose a constant velocity field $u = M_s c_0$ to the solution of the stationary shock wave found in the previous steps. We setup our computation with the exact solution of a shock wave (initially centered at $x = 0.25$), traveling at $M_s = 2.0$ to the right into a medium at rest. The values of the unperturbed fluid in front of the shock wave are chosen as $\rho_0 = 1$ (which also serves as reference density for the HPR model), $u_0 = v_0 = 0$ and $p_0 = 1/\gamma$, hence $c_0 = 1$. The Reynolds number based on the shock speed and a unitary reference length ($L = 1$) is defined as $\mathrm{Re}_s = \frac{\rho_0 c_0 M_s L}{\mu}$. The parameters of the first order HPR model are chosen as $\gamma = 1.4$, $c_v = 2.5$, $c_s = 50$, $\mu = 2 \cdot 10^{-2}$, $\alpha = 50$, $T_0 = 1$ and $\kappa = 9\frac{1}{3} \cdot 10^{-2}$. The resulting shock Reynolds number is $\mathrm{Re}_s = 100$. The distortion tensor is initialized with $\boldsymbol{A} = \sqrt[3]{\rho}\,\mathbf{I}$ and the initial heat flux is set to $\mathbf{J} = 0$, so that the system is started out of equilibrium. Simulations are carried out with an ADER-DG P_3P_3 scheme ($N = M = 3$) up to a final time of $t = 0.2$, by which the shock wave has traveled a distance of 0.4 to the right. The computational domain is given by $\Omega = [-0.5, 0.5] \times [-0.1, 0.1]$ and the mesh contains 100×5 elements. The comparison between the numerical solution of the first order HPR model and the exact solution of the compressible Navier–Stokes equations (91) and (93) is presented in Figs. 19 and 20. One observes an excellent agreement of the viscous shock profile, apart from a small spurious wave at the left of the shock, which could be due to a small start-up error resulting from the non-equilibrium initial condition in the variables $\boldsymbol{A}$ and $\mathbf{J}$.

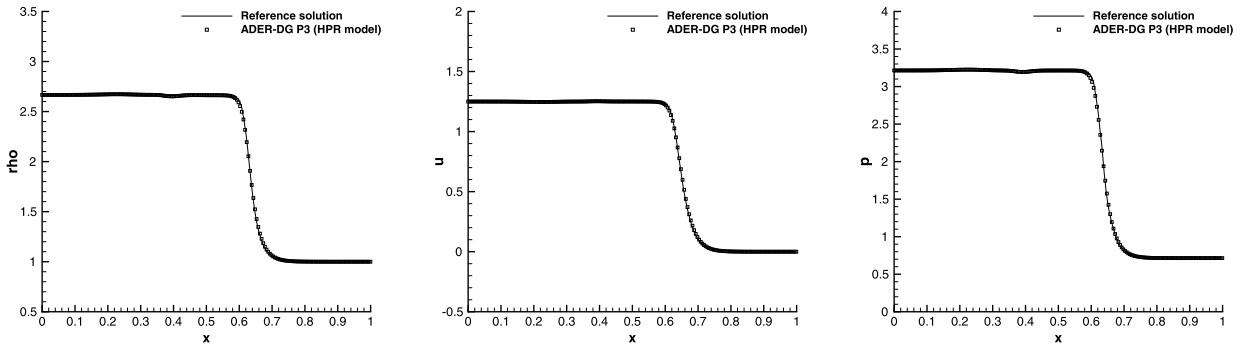

Fig. 19. Viscous shock with shock Mach number $M_s = 2$ and Prandtl number $\mathrm{Pr} = 0.75$ at a final time of $t = 0.2$. Comparison of the exact solution of the compressible Navier–Stokes equations according to Becker [13] with the HPR model. Density profile (left) velocity profile (middle) and pressure profile (right).

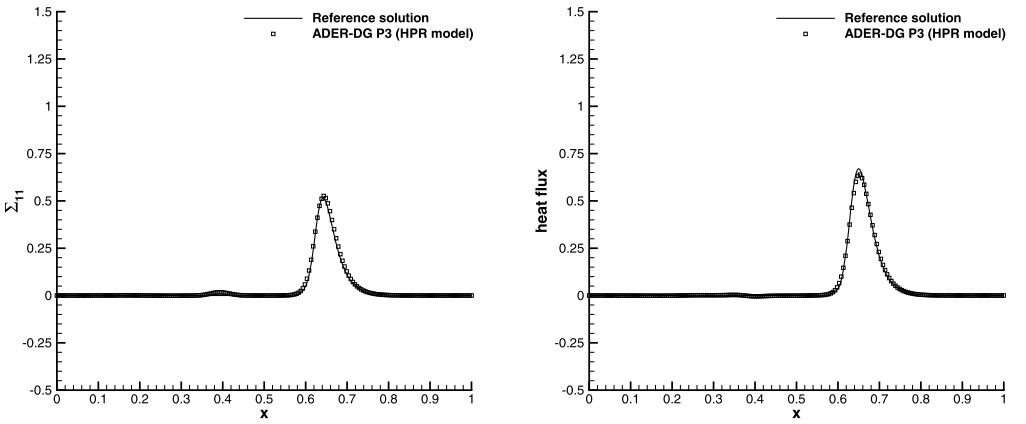

Fig. 20. Viscous shock with shock Mach number $M_s = 2$ and Prandtl number $\mathrm{Pr} = 0.75$ at a final time of $t = 0.2$. Viscous stress tensor component σ_{11} (left) and heat flux (right). For the Navier–Stokes solution, the classical Fourier heat flux $q_1 = -\kappa T_x$ is shown, while for the HPR model, we plot $q_1 = \alpha^2 T J_1$.

4.14. Viscous double Mach reflection problem

In this section we run a viscous version of the 2D double Mach reflection problem of a strong shock, which has been originally proposed for the compressible Euler equations by Woodward and Colella in [143]. This test problem involves a Mach 10 shock that hits a 30° ramp. Using the Rankine–Hugoniot conditions of the compressible Euler equations we can deduce the initial conditions for the flow variables in front of and behind the shock wave as

$$(\rho, u, v, p)(\mathbf{x}, t = 0) = \begin{cases} \frac{1}{\gamma}(8.0, 8.25, 0.0, 116.5), & \text{if} \quad x' < 0.1, \\ (1.0, 0.0, 0.0, \frac{1}{\gamma}), & \text{if} \quad x' \geq 0.1, \end{cases} \tag{94}$$

where x' is the coordinate in a rotated coordinate system. Reflecting slip wall boundary conditions are prescribed on the bottom and the exact solution of an isolated moving oblique shock wave with shock Mach number $M_s = 10$ is imposed on the upper boundary. Inflow and outflow boundary conditions are prescribed on the left side and the right side, respectively.

The computational domain is given by $\Omega = [0; 3.5] \times [0; 1]$ and the computational grid uses a characteristic length of $h = 1/400$, leading to 1400×400 computational cells. We solve this problem with a third order P_0P_2 ADER–WENO finite volume scheme ($N = 0$, $M = 2$). The parameters of the HPR model are: $\gamma = 1.4$, $c_v = 2.5$, $\rho_0 = 1$, $c_s = 20$, $\alpha^2 = 200$, $T_0 = 1$ and $\kappa = \gamma c_v \mu / \mathrm{Pr}$ with a Prandtl number of $\mathrm{Pr} = 0.75$. The initial condition for the distortion tensor is chosen as $\boldsymbol{A} = \sqrt[3]{\rho}\,\mathbf{I}$ and the heat flux is initialized with $\mathbf{J} = 0$. The computational results are depicted in Fig. 21 for the density variable at a final time of $t = 0.2$ using two different values for the viscosity coefficient: $\mu = 10^{-1}$, which corresponds to a shock Reynolds number of $\mathrm{Re}_s = 100$, and $\mu = 10^{-2}$, corresponding to $\mathrm{Re}_s = 1000$. An inviscid reference calculation of the compressible Euler equations with the same ADER–WENO scheme on the same grid is also provided in Fig. 21, to show that the missing flow features in the HPR model are actually due to the presence of physical viscosity and not due to the effect of numerical diffusion. Overall one can observe that the typical flow structures like the incident shock wave, the reflected shock wave and the Mach stem are well reproduced. Furthermore, the typical mushroom-type flow structure close to the x-axis is also present in the viscous computations carried out with the HPR model. However, in this test problem, a rather large physical viscosity has been added, hence preventing the development of any unstable small-scale flow structures as observed in

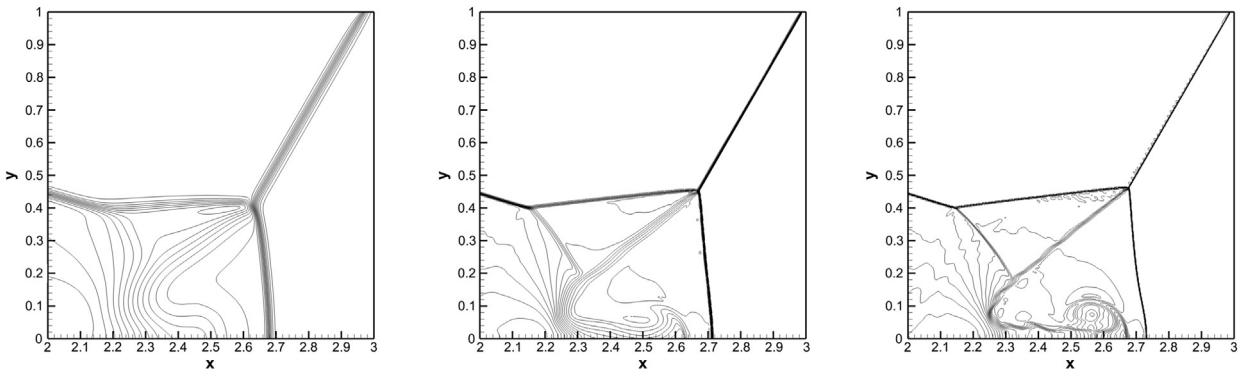

Fig. 21. Zoom into the viscous double Mach reflection problem at various shock Reynolds numbers at a final time of $t = 0.2$ computed with a third order ADER–WENO finite volume method solving the HPR model. Left: $\mu = 10^{-1}$ ($\mathrm{Re}_s = 100$). Middle: $\mu = 10^{-2}$, ($\mathrm{Re}_s = 1000$). Right: Inviscid Euler reference calculation ($\mathrm{Re}_s \to \infty$). 41 density contour levels in the interval [1.5, 17.5].

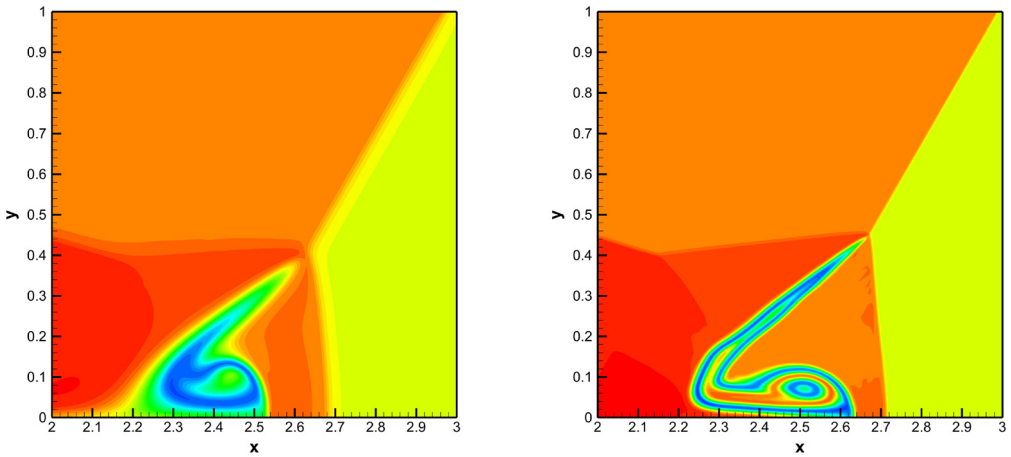

Fig. 22. Distortion tensor component A_{11} of the HPR model for the viscous double Mach reflection problem at a final time of $t = 0.2$, computed with a third order ADER–WENO finite volume method. Left: $\mu = 10^{-1}$ ($\mathrm{Re}_s = 100$). Right: $\mu = 10^{-2}$, ($\mathrm{Re}_s = 1000$). 31 contour levels are shown in the interval $[-2.25, +2.25]$. (For interpretation of the colors in this figure, the reader is referred to the web version of this article.)

[3,54,149] and as obtained in the inviscid reference calculation. For other numerical results concerning the viscous double Mach reflection problem, see [37]. In Fig. 22 we also provide a visualization of the distortion tensor component A_{11}, which clearly indicates the presence of the shear layers and the mushroom-type flow feature, underpinning just once more the value of $\boldsymbol{A}$ for the purpose of flow visualization.

4.15. Application to solid mechanics

The main key advantage of the HPR model (1a)–(2) is its capability to describe in *one single PDE system* the two main branches of **continuum mechanics**, namely **fluid mechanics** *and* **solid mechanics**. We explicitly stress here that the test problem proposed in this section **cannot** be solved with the conventional Navier–Stokes equations, since it is a typical test problem of *solid mechanics*! Here we consider a typical benchmark problem used in computational seismology [88,87,85], consisting in the propagation of a wave in a linear elastic solid with free surface. The problem was first discussed and solved by Lamb in 1904, see [90] and is therefore often called *Lamb's problem* in the literature. The problem consists in a point force acting on an elastic solid, perpendicular to a free surface. In our particular setup, the computational domain is given by $\Omega = [-2000, 2000] \times [-2000, 0]$ and we add the following point source to the right hand side of the momentum equation (1b):

$$\mathbf{S}(\mathbf{x}, t) = \rho_0 a_1 \left(\frac{1}{2} + a_2 (t - t_D)^2 \right) \exp\left(a_2 (t - t_D)^2 \right) \delta(\mathbf{x} - \mathbf{x}_s) \mathbf{e}_y, \tag{95}$$

with the Dirac delta distribution $\delta(\mathbf{x})$, the unit vector pointing in y-direction $\mathbf{e}_y = (0, 1)$, and the following source parameters: $t_D = 0.08$, $a_1 = -2000$, $a_2 = -(\pi f_c)^2$, $fc = 14.5$. The source is located in $\mathbf{x}_s = (0, -1)$, hence slightly below the free surface, which is located at $y = 0$. At the free surface, the shear stresses $\sigma_{12} = \sigma_{21}$ and the normal stress σ_{22} vanish. The parameters of the HPR model with stiffened gas EOS are $\rho_0 = 2200$, $c_v = 1$, $\gamma = 2$, $c_0 = 2385.160721$,

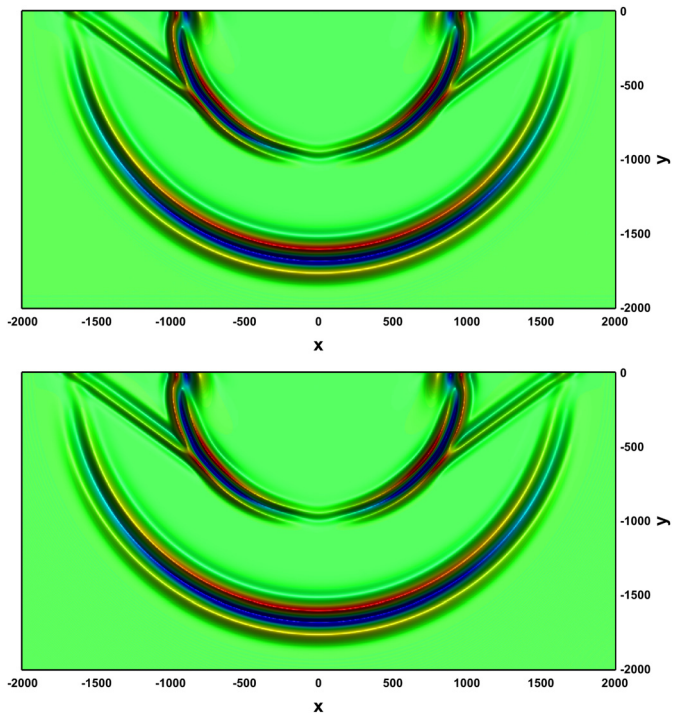

Fig. 23. Lamb's problem in 2D at a final time of $t = 0.6$ computed with an ADER-DG P4 method. Contour colors of v for the HPR model (top) and the reference solution based on the equations of linear elasticity (bottom). (For interpretation of the references to color in this figure legend, the reader is referred to the web version of this article.)

$c_s = 1847.5$, $\alpha = 0$, $\tau_1 \to \infty$ and $\tau_2 \to \infty$. In practice, we set $\tau_1 = \tau_2 = 10^{20}$. The initial condition is chosen as $\rho = \rho_0$, $u = v = 0$, $p = 0$, $\boldsymbol{A} = \mathbf{I}$ and $\mathbf{J} = 0$. With the previous parameters, the resulting sound speed of longitudinal pressure waves is $c_L = \sqrt{c_0^2 + 4/3 c_s^2} = 3200$. Simulations are performed with a P_4P_4 ADER-DG scheme ($N = M = 4$) up to a final time of $t = 1.3$ using a grid composed of 200×100 elements.

In order to have a direct comparison with classical theory of linear elasticity, we solve the problem again with the same ADER-DG scheme on the same grid, but in the second run we directly solve the classical equations of linear elasticity in velocity-stress formulation [88,87,85],

$$
\begin{aligned}
&\frac{\partial}{\partial t}\sigma_{xx} - (\lambda + 2\mu)\frac{\partial}{\partial x}u - \lambda\frac{\partial}{\partial y}v = 0,\\
&\frac{\partial}{\partial t}\sigma_{yy} - \lambda\frac{\partial}{\partial x}u - (\lambda + 2\mu)\frac{\partial}{\partial y}v = 0,\\
&\frac{\partial}{\partial t}\sigma_{xy} - \mu\frac{\partial}{\partial x}v - \mu\frac{\partial}{\partial y}u = 0,\\
&\rho\frac{\partial}{\partial t}u - \frac{\partial}{\partial x}\sigma_{xx} - \frac{\partial}{\partial y}\sigma_{xy} = 0,\\
&\rho\frac{\partial}{\partial t}v - \frac{\partial}{\partial x}\sigma_{xy} - \frac{\partial}{\partial y}\sigma_{yy} = 0.
\end{aligned}
\tag{96}
$$

The two Lamé constants in (96) $\lambda = 7.509672500 \cdot 10^9$ and $\mu = 7.509163750 \cdot 10^9$ (not to be confused with the viscosity μ) are chosen in order to obtain the same wave propagation speeds as in the HPR model, i.e. $c_p = \sqrt{(\lambda + 2\mu)/\rho} = 3200$ for longitudinal pressure waves and $c_s = \sqrt{\mu/\rho} = 1847.5$ for shear waves. The density is, of course, also set to $\rho = 2200$. The same point source (95) as in the HPR model is added to the right hand side of the last equation of (96). The computational results obtained with both models are compared against each other in Fig. 23, where we note an excellent agreement of the two computed wave fields. In Fig. 24 we compare the velocity signal v at an observation point located at $x = (990, 0)$, where also a very good agreement between the nonlinear HPR model and the reference solution based on the linear elastic wave equations can be observed.

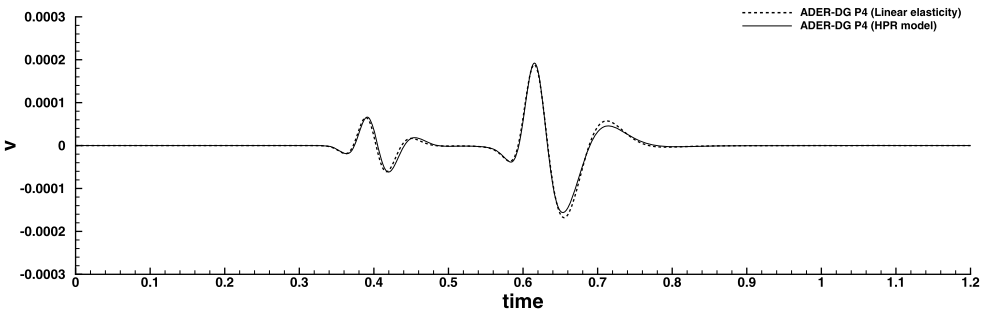

Fig. 24. Time signal of the velocity component v recorded at $(990, 0)$ for Lamb's problem in 2D. Comparison between the HPR model and the reference solution based on the equations of linear elasticity.

5. Conclusion

To the knowledge of the authors, this is the first time that a numerical method has been applied to the full first order hyperbolic Peshkov–Romenski model [110] with heat conduction, see Eqns. (1)–(2). The proposed family of high order one-step ADER finite volume and ADER discontinuous Galerkin finite element schemes is able to discretize rather general hyperbolic systems of partial differential equations with non-conservative products and stiff source terms and has been applied in the frame of the HPR model to a large set of different test problems, ranging from viscous compressible fluids to elastic solids. We have shown numerical convergence results, as well as detailed comparisons with different analytical and numerical reference solutions. It is very important to stress again that the first order HPR model is able to represent the basic equations of continuum mechanics in a unified manner, including *fluid mechanics* and *solid mechanics* as two special limiting cases of the *same* mathematical model. The nonlinear material behavior is entirely governed by the equation of state and by the strain relaxation mechanism $\boldsymbol{\psi}$. To the knowledge of the authors, such a universal formulation of continuum mechanics in a first order hyperbolic system is *unique* and has never been tackled before with high order shock capturing methods for hyperbolic conservation laws.

Future applications will concern the extension of the numerical method to moving unstructured meshes in the frame of ADER–WENO–ALE schemes [40,21], as well as to non-Newtonian fluids and complex visco-plastic solids. The use of high order schemes for hyperbolic PDE on space–time adaptive meshes, as outlined in [53,46,149], might also become useful in near future in combination with the HPR model in the context of crack generation and crack propagation in nonlinear solid mechanics, following the ideas proposed in [57,58].

Since the HPR model has already *finite wave speeds* for all involved physical processes, i.e. heat and mass transport, as well as viscous momentum transport, future research will be carried out in order to extend it also to the *relativistic regime*, following the promising investigations by [79].

Acknowledgements

The authors would like to thank Sergey Gavrilyuk for very fruitful discussions about the model and the results presented in this paper. We also would like to thank Sergei Konstantinovich Godunov for his groundbreaking and very inspiring seminal ideas that are at the basis of both the theoretical as well as the numerical framework employed in this paper. Last but not least, we would like to thank the two anonymous referees for their constructive comments that helped to improve the clarity and the quality of this paper.

The research presented in this paper has been financed by the European Research Council (ERC) under the European Union's Seventh Framework Programme (FP7/2007–2013) with the research project *STiMulUs*, ERC Grant agreement No. 278267. M.D. and O.Z. have further received funding from the European Union's Horizon 2020 Research and Innovation Programme under the project *ExaHyPE*, Grant agreement number No. 671698 (call FETHPC-1-2014).

We would also like to acknowledge PRACE for awarding access to the SuperMUC supercomputer based in Munich, Germany, at the Leibniz Rechenzentrum (LRZ).

Appendix A. Eigenvalues of the matrices $\mathcal{A}_k$

In this section, we give the formulas for the eigenvalues of matrices $\mathcal{C}_k$ of the viscous subsystem of (1). Thus, if the heat conducting effect is ignored, then matrices $\mathcal{C}_k$ look as follows

$$\mathcal{C}_k(\mathbf{V}) = \begin{pmatrix} v_k & 0 & z_1 & z_2 & z_3 & 0 & 0 & 0 \\ 0 & v_k & Z_1 & Z_2 & Z_3 & 0 & 0 & 0 \\ R_1 & P_1 & v_k & 0 & 0 & X_{11} & X_{12} & X_{13} \\ R_2 & P_2 & 0 & v_k & 0 & X_{21} & X_{32} & X_{23} \\ R_3 & P_3 & 0 & 0 & v_k & X_{31} & X_{32} & X_{33} \\ 0 & 0 & A_{11} & A_{12} & A_{13} & v_k & 0 & 0 \\ 0 & 0 & A_{21} & A_{22} & A_{23} & 0 & v_k & 0 \\ 0 & 0 & A_{31} & A_{32} & A_{33} & 0 & 0 & v_k \end{pmatrix}, \tag{A.1}$$

where (no summation over repeated index k)

$$\rho R_i = \frac{\partial \sigma_{ik}}{\partial \rho}, \quad \rho P_i = \delta_{ik} + \frac{\partial \sigma_{ik}}{\partial p}, \quad \rho X_{ij} = \frac{\partial \sigma_{ik}}{\partial A_{jk}}$$

$$z_k = \rho, \quad z_m = z_n = 0, \quad m \neq k, n \neq k,$$

$$Z_k \frac{\partial \rho E_1}{\partial p} = \rho E_1 + \rho E_2 - \rho \frac{\partial \rho E_1}{\partial \rho} + p + \sigma_{kk}, \quad Z_m \frac{\partial \rho E_1}{\partial p} = \sigma_{mk}, \quad Z_n \frac{\partial \rho E_1}{\partial p} = \sigma_{nk}, \quad m \neq k, n \neq k.$$

The eigenvalues of the matrix $\mathcal{C}_k(\mathbf{V})$ are given by the formulas

$$v_k - \lambda_3, \;\; v_k - \lambda_2, \;\; v_k - \lambda_1, \;\; v_k, \;\; v_k, \;\; v_k + \lambda_1, \;\; v_k + \lambda_2, \;\; v_k + \lambda_3, \tag{A.2}$$

where $\lambda_1 \leq \lambda_2 < \lambda_3$ are three eigenvalues of the 3-by-3 matrix

$$\mathbf{W} = \mathbf{W}_1 \mathbf{W}_2,$$

where

$$\mathbf{W}_1 = \begin{pmatrix} R_1 & P_1 & X_{11} & X_{12} & X_{13} \\ R_2 & P_2 & X_{21} & X_{22} & X_{23} \\ R_3 & P_3 & X_{31} & X_{32} & X_{33} \end{pmatrix}, \quad \mathbf{W}_2 = \begin{pmatrix} z_1 & z_2 & z_3 \\ Z_1 & Z_2 & Z_3 \\ A_{11} & A_{12} & A_{13} \\ A_{21} & A_{22} & A_{23} \\ A_{31} & A_{32} & A_{33} \end{pmatrix}.$$

Because of that the EOS is assumed to be a convex function of the state variables $\mathbf{V}$ [110] and hence the HPR model is symmetric hyperbolic, the eigenvalues are thus assumed to be real, and can be found by analytical formulas as the roots of the cubic polynomial $\det(\mathbf{W} - \lambda \mathbf{I}) = 0$. They are

$$\lambda_k = \sqrt{\beta_k + \mathrm{tr}(\mathbf{W})/3},$$

where $\beta_k = 2\sqrt{-a/3}\cos((\phi + 2(k-1)\pi))/3)$ and

$$\phi = \begin{cases} \mathrm{acos}(-\sqrt{-27b^2/(4a^3)}), & \text{if } b > 0 \\ \mathrm{acos}(\sqrt{-27b^2/(4a^3)}), & \text{if } b < 0 \end{cases}$$

Here, $a = (I_1^2 - 3I_2)/6$ and $b = \left(5I_1^3/9 - I_1 I_2 - 6\det(\mathbf{W})\right)/6$, $I_1 = \mathrm{tr}(\mathbf{W})$ and $I_2 = \mathrm{tr}(\mathbf{W}^2)$.

References

[1] D.N. Arnold, F. Brezzi, B. Cockburn, L.D. Marini, Unified analysis of discontinuous Galerkin methods for elliptic problems, SIAM J. Numer. Anal. 39 (2002) 1749–1779.

[2] A. Babucke, M. Kloker, U. Rist, DNS of a plane mixing layer for the investigation of sound generation mechanisms, Comput. Fluids 37 (2008) 360–368.

[3] D. Balsara, C.W. Shu, Monotonicity preserving weighted essentially non-oscillatory schemes with increasingly high order of accuracy, J. Comput. Phys. 160 (2000) 405–452.

[4] D.S. Balsara, T. Rumpf, M. Dumbser, C.-D. Munz, Efficient, high accuracy ADER–WENO schemes for hydrodynamics and divergence-free magnetohydrodynamics, J. Comput. Phys. 228 (2009) 2480–2516.

[5] D.S. Balsara, M. Dumbser, Divergence-free MHD on unstructured meshes using high order finite volume schemes based on multidimensional Riemann solvers, J. Comput. Phys. 299 (2015) 687–715.

[6] D.S. Balsara, C. Meyer, M. Dumbser, H. Du, Z. Xu, Efficient implementation of ADER schemes for Euler and magnetohydrodynamical flows on structured meshes – speed comparisons with Runge–Kutta methods, J. Comput. Phys. 235 (2013) 934–969.

[7] P.T. Barton, R. Deiterding, D. Meiron, D. Pullin, Eulerian adaptive finite-difference method for high-velocity impact and penetration problems, J. Comput. Phys. 240 (2013) 76–99.

[8] P.T. Barton, D. Drikakis, E. Romenski, V.A. Titarev, Exact and approximate solutions of Riemann problems in non-linear elasticity, J. Comput. Phys. 228 (18) (2009) 7046–7068.

[9] P.T. Barton, D. Drikakis, E.I. Romenski, An Eulerian finite-volume scheme for large elastoplastic deformations in solids, Int. J. Numer. Methods Eng. 81 (4) (2010) 453–484.
[10] F. Bassi, S. Rebay, A high-order accurate discontinuous finite element method for the numerical solution of the compressible Navier–Stokes equations, J. Comput. Phys. 131 (1997) 267–279.
[11] C.E. Baumann, J.T. Oden, A discontinuous hp finite element method for convection–diffusion problems, Comput. Methods Appl. Mech. Eng. 175 (3–4) (1999) 311–341.
[12] C.E. Baumann, J.T. Oden, A discontinuous hp finite element method for the Euler and Navier–Stokes equations, Int. J. Numer. Methods Fluids 31 (1) (1999) 79–95.
[13] R. Becker, Stosswelle und Detonation, Physik 8 (1923) 321.
[14] J.B. Bell, P. Coletta, H.M. Glaz, A second-order projection method for the incompressible Navier–Stokes equations, J. Comput. Phys. 85 (1989) 257–283.
[15] M. Ben-Artzi, J. Li, G. Warnecke, A direct Eulerian GRP scheme for compressible fluid flows, J. Comput. Phys. 218 (2006) 19–43.
[16] J.F. Besseling, A thermodynamic approach to rheology, in: H. Parkus, L.I. Sedov (Eds.), Irreversible Aspects of Continuum Mechanics and Transfer of Physical Characteristics in Moving Fluids, IUTAM Symposia, Springer, Vienna, 1968, pp. 16–53.
[17] H. Blasius, Grenzschichten in Flüssigkeiten mit kleiner Reibung, Z. Math. Phys. 56 (1908) 1–37.
[18] D. Bolmatov, V.V. Brazhkin, K. Trachenko, Thermodynamic behaviour of supercritical matter, Nat. Commun. 4 (2013).
[19] D. Bolmatov, M. Zhernenkov, D. Zav'yalov, S. Stoupin, Y.Q. Cai, A. Cunsolo, Revealing the mechanism of the viscous-to-elastic crossover in liquids, J. Phys. Chem. Lett. 6 (15) (2015) 3048–3053.
[20] A. Bonnet, J. Luneau, Aérodynamique. Théories de la dynamique des fluides, Cepadues Editions, Toulouse, ISBN 2854282183, 1989.
[21] W. Boscheri, M. Dumbser, A direct arbitrary-Lagrangian–Eulerian ADER–WENO finite volume scheme on unstructured tetrahedral meshes for conservative and nonconservative hyperbolic systems in 3D, J. Comput. Phys. 275 (2014) 484–523.
[22] M.E. Brachet, D.I. Meiron, S.A. Orszag, B.G. Nickel, R.H. Morf, U. Frisch, Small-scale structure of the Taylor–Green vortex, J. Fluid Mech. 130 (1983) 411–452.
[23] V.V. Brazhkin, Yu.D. Fomin, A.G. Lyapin, V.N. Ryzhov, K. Trachenko, Two liquid states of matter: a dynamic line on a phase diagram, Phys. Rev. E 85 (3) (2012) 031203.
[24] C.C. Castro, E.F. Toro, Solvers for the high-order Riemann problem for hyperbolic balance laws, J. Comput. Phys. 227 (2008) 2481–2513.
[25] M.J. Castro, J.M. Gallardo, A. Marquina, Approximate Osher–Solomon schemes for hyperbolic systems, Appl. Math. Comput. 272 (2016) 347–368.
[26] M.J. Castro, J.M. Gallardo, C. Parés, High-order finite volume schemes based on reconstruction of states for solving hyperbolic systems with nonconservative products. Applications to shallow-water systems, Math. Comput. 75 (2006) 1103–1134.
[27] M.J. Castro, P.G. LeFloch, M.L. Muñoz-Ruiz, C. Parés, Why many theories of shock waves are necessary: convergence error in formally path-consistent schemes, J. Comput. Phys. 227 (2008) 8107–8129.
[28] C. Cattaneo, Sulla conduzione del calore, Atti Semin. Mat. Fis. Univ. Modena 3 (1948).
[29] J. Cesenek, M. Feistauer, J. Horacek, V. Kucera, J. Prokopova, Simulation of compressible viscous flow in time-dependent domains, Appl. Math. Comput. 219 (2013) 7139–7150.
[30] E.D. Chisolm, D.C. Wallace, Dynamics of monatomic liquids, J. Phys. Condens. Matter 13 (37) (2001) R739.
[31] B. Cockburn, C.W. Shu, The local discontinuous Galerkin method for time-dependent convection diffusion systems, SIAM J. Numer. Anal. 35 (1998) 2440–2463.
[32] B. Cockburn, C.W. Shu, Runge–Kutta discontinuous Galerkin methods for convection-dominated problems, J. Sci. Comput. 16 (2001) 173–261.
[33] T. Colonius, S.K. Lele, P. Moin, Sound generation in a mixing layer, J. Fluid Mech. 330 (1997) 375–409.
[34] R. Courant, K. Friedrichs, H. Lewy, Über die partiellen Differenzengleichungen der mathematischen Physik, Math. Ann. 100 (1) (1928) 32–74.
[35] C.M. Dafermos, Hyperbolic Conservation Laws in Continuum Physics, Springer-Verlag, Berlin, 2005.
[36] M. Dubiner, Spectral methods on triangles and other domains, J. Sci. Comput. 6 (1991) 345–390.
[37] M. Dumbser, Arbitrary high order PNPM schemes on unstructured meshes for the compressible Navier–Stokes equations, Comput. Fluids 39 (2010) 60–76.
[38] M. Dumbser, D. Balsara, E.F. Toro, C.D. Munz, A unified framework for the construction of one-step finite-volume and discontinuous Galerkin schemes, J. Comput. Phys. 227 (2008) 8209–8253.
[39] M. Dumbser, D.S. Balsara, A new, efficient formulation of the HLLEM Riemann solver for general conservative and non-conservative hyperbolic systems, J. Comput. Phys. 304 (2016) 275–319.
[40] M. Dumbser, W. Boscheri, High-order unstructured Lagrangian one-step WENO finite volume schemes for non-conservative hyperbolic systems: applications to compressible multi-phase flows, Comput. Fluids 86 (2013) 405–432.
[41] M. Dumbser, M. Castro, C. Parés, E.F. Toro, ADER schemes on unstructured meshes for non-conservative hyperbolic systems: applications to geophysical flows, Comput. Fluids 38 (2009) 1731–1748.
[42] M. Dumbser, V. Casulli, A conservative, weakly nonlinear semi-implicit finite volume scheme for the compressible Navier–Stokes equations with general equation of state, Appl. Math. Comput. 272 (2016) 479–497.
[43] M. Dumbser, C. Enaux, E.F. Toro, Finite volume schemes of very high order of accuracy for stiff hyperbolic balance laws, J. Comput. Phys. 227 (2008) 3971–4001.
[44] M. Dumbser, M. Facchini, A local space–time discontinuous Galerkin method for Boussinesq-type equations, Appl. Math. Comput. 272 (2016) 336–346.
[45] M. Dumbser, A. Hidalgo, M. Castro, C. Parés, E.F. Toro, FORCE schemes on unstructured meshes II: non-conservative hyperbolic systems, Comput. Methods Appl. Mech. Eng. 199 (2010) 625–647.
[46] M. Dumbser, A. Hidalgo, O. Zanotti, High order space–time adaptive ADER–WENO finite volume schemes for non-conservative hyperbolic systems, Comput. Methods Appl. Mech. Eng. 268 (2014) 359–387.
[47] M. Dumbser, M. Käser, Arbitrary high order non-oscillatory finite volume schemes on unstructured meshes for linear hyperbolic systems, J. Comput. Phys. 221 (2007) 693–723.
[48] M. Dumbser, M. Käser, V.A. Titarev, E.F. Toro, Quadrature-free non-oscillatory finite volume schemes on unstructured meshes for nonlinear hyperbolic systems, J. Comput. Phys. 226 (2007) 204–243.
[49] M. Dumbser, C.D. Munz, Building blocks for arbitrary high order discontinuous Galerkin schemes, J. Sci. Comput. 27 (2006) 215–230.
[50] M. Dumbser, E.F. Toro, On universal Osher-type schemes for general nonlinear hyperbolic conservation laws, Commun. Comput. Phys. 10 (2011) 635–671.
[51] M. Dumbser, E.F. Toro, A simple extension of the Osher Riemann solver to non-conservative hyperbolic systems, J. Sci. Comput. 48 (2011) 70–88.
[52] M. Dumbser, O. Zanotti, Very high order PNPM schemes on unstructured meshes for the resistive relativistic MHD equations, J. Comput. Phys. 228 (2009) 6991–7006.
[53] M. Dumbser, O. Zanotti, A. Hidalgo, D.S. Balsara, ADER–WENO finite volume schemes with space–time adaptive mesh refinement, J. Comput. Phys. 248 (2013) 257–286.
[54] M. Dumbser, O. Zanotti, R. Loubère, S. Diot, A posteriori subcell limiting of the discontinuous Galerkin finite element method for hyperbolic conservation laws, J. Comput. Phys. 278 (December 2014) 47–75.

[55] B. Einfeldt, On Godunov-type methods for gas dynamics, SIAM J. Numer. Anal. 25 (1988) 294–318.
[56] B. Einfeldt, C.D. Munz, P.L. Roe, B. Sjögreen, On Godunov-type methods near low densities, J. Comput. Phys. 92 (1991) 273–295.
[57] N. Favrie, S.L. Gavrilyuk, R. Saurel, Solid–fluid diffuse interface model in cases of extreme deformations, J. Comput. Phys. 228 (16) (2009) 6037–6077.
[58] N. Favrie, S.L. Gavrilyuk, Diffuse interface model for compressible fluid – compressible elastic–plastic solid interaction, J. Comput. Phys. 231 (2012) 2695–2723.
[59] P. Le Floch, L. Tatsien, A global asymptotic expansion for the solution of the generalized Riemann problem, Ann. Inst. Henri Poincaré, C Anal. Non Linéaire 3 (1991) 321–340.
[60] J. Frenkel, Kinetic Theory of Liquids, Dover, 1955.
[61] G. Gassner, M. Dumbser, F. Hindenlang, C.D. Munz, Explicit one-step time discretizations for discontinuous Galerkin and finite volume schemes based on local predictors, J. Comput. Phys. 230 (2011) 4232–4247.
[62] G. Gassner, F. Lörcher, C.D. Munz, A discontinuous Galerkin scheme based on a space–time expansion II. Viscous flow equations in multi dimensions, J. Sci. Comput. 34 (2008) 260–286.
[63] G. Gassner, F. Lörcher, C.D. Munz, A contribution to the construction of diffusion fluxes for finite volume and discontinuous Galerkin schemes, J. Comput. Phys. 224 (2007) 1049–1063.
[64] S.L. Gavrilyuk, N. Favrie, R. Saurel, Modelling wave dynamics of compressible elastic materials, J. Comput. Phys. 227 (2008) 2941–2969.
[65] U. Ghia, K.N. Ghia, C.T. Shin, High-Re solutions for incompressible flow using Navier–Stokes equations and multigrid method, J. Comput. Phys. 48 (1982) 387–411.
[66] E. Godlewski, P.A. Raviart, Numerical Approximation of Hyperbolic Systems of Conservation Laws, Springer, 1996.
[67] Sergei Konstantinovich Godunov, The problem of a generalized solution in the theory of quasilinear equations and in gas dynamics, Russ. Math. Surv. 17 (3) (1962) 145–156.
[68] S.K. Godunov, An interesting class of quasilinear systems, Dokl. Akad. Nauk SSSR 139 (3) (1961) 521–523.
[69] S.K. Godunov, Symmetric form of the magnetohydrodynamic equation, Numer. Methods Mech. Contin. Medium 3 (1) (1972) 26–34.
[70] S.K. Godunov, Elements of Mechanics of Continuous Media, Nauka, 1978 (in Russian).
[71] S.K. Godunov, Equations of Mathematical Physics, Nauka, Moscow, 1979 (in Russian).
[72] S.K. Godunov, T.Yu. Mikhailova, E.I. Romenski, Systems of thermodynamically coordinated laws of conservation invariant under rotations, Sib. Math. J. 37 (4) (1996) 690–705.
[73] S.K. Godunov, I.M. Peshkov, Thermodynamically consistent nonlinear model of elastoplastic Maxwell medium, Comput. Math. Math. Phys. 50 (8) (2010) 1409–1426.
[74] S.K. Godunov, E.I. Romenski, Nonstationary equations of nonlinear elasticity theory in Eulerian coordinates, J. Appl. Mech. Tech. Phys. 13 (6) (1972) 868–884.
[75] S.K. Godunov, E.I. Romenski, Thermodynamics, conservation laws and symmetric forms of differential equations in mechanics of continuous media, Comput. Fluid Dyn. Rev. 95 (1995) 19–31.
[76] S.K. Godunov, E.I. Romenski, Symmetric forms of thermodynamically compatible systems of conservation laws in continuum mechanics, in: ECCOMAS Conference on Numerical Methods in Engineering, 1996, pp. 54–57.
[77] S.K. Godunov, E.I. Romenski, Elements of Mechanics of Continuous Media, Nauchnaya Kniga, 1998 (in Russian).
[78] S.K. Godunov, E.I. Romenski, Elements of Continuum Mechanics and Conservation Laws, Kluwer Academic/Plenum Publishers, 2003.
[79] C. Gundlach, I. Hawke, S.J. Erickson, A conservation law formulation of nonlinear elasticity in general relativity, Class. Quantum Gravity 29 (1) (January 2012) 015005.
[80] R. Hartmann, P. Houston, Symmetric interior penalty DG methods for the compressible Navier–Stokes equations I: method formulation, Int. J. Numer. Anal. Model. 3 (2006) 1–20.
[81] R. Hartmann, P. Houston, An optimal order interior penalty discontinuous Galerkin discretization of the compressible Navier–Stokes equations, J. Comput. Phys. 227 (2008) 9670–9685.
[82] A. Hidalgo, M. Dumbser, ADER schemes for nonlinear systems of stiff advection–diffusion–reaction equations, J. Sci. Comput. 48 (2011) 173–189.
[83] C. Hu, C.W. Shu, Weighted essentially non-oscillatory schemes on triangular meshes, J. Comput. Phys. 150 (1999) 97–127.
[84] G.E. Karniadakis, S.J. Sherwin, Spectral/hp Element Methods in CFD, Oxford University Press, 1999.
[85] M. Käser, M. Dumbser, An arbitrary high order discontinuous Galerkin method for elastic waves on unstructured meshes I: the two-dimensional isotropic case with external source terms, Geophys. J. Int. 166 (2006) 855–877.
[86] C. Klaij, J.J.W. Van der Vegt, H. Van der Ven, Space–time discontinuous Galerkin method for the compressible Navier–Stokes equations, J. Comput. Phys. 217 (2006) 589–611.
[87] D. Komatitsch, J. Tromp, Introduction to the spectral-element method for 3-d seismic wave propagation, Geophys. J. Int. 139 (1999) 806–822.
[88] D. Komatitsch, J.P. Vilotte, The spectral-element method: an efficient tool to simulate the seismic response of 2d and 3d geological structures, Bull. Seismol. Soc. Am. 88 (1998) 368–392.
[89] A.G. Kulikovskii, N.V. Pogorelov, A.Yu. Semenov, Mathematical Aspects of Numerical Solution of Hyperbolic Systems, CRC Press, 2000.
[90] H. Lamb, On the propagation of tremors over the surface of an elastic solid, Philos. Trans. R. Soc. Lond. Ser. A 203 (1904) 1–42.
[91] L.D. Landau, E.M. Lifshitz, Fluid Mechanics, Course of Theoretical Physics, vol. 6, Elsevier Butterworth–Heinemann, Oxford, 2004.
[92] D. Levy, C.W. Shu, J. Yan, Local discontinuous Galerkin methods for nonlinear dispersive equations, J. Comput. Phys. 196 (2004) 751–772.
[93] R. Loubère, M. Dumbser, S. Diot, A new family of high order unstructured MOOD and ADER finite volume schemes for multidimensional systems of hyperbolic conservation laws, Commun. Comput. Phys. 16 (2014) 718–763.
[94] H. Luo, L. Luo, R. Nourgaliev, V.A. Mousseau, N. Dinh, A reconstructed discontinuous Galerkin method for the compressible Navier–Stokes equations on arbitrary grids, J. Comput. Phys. 229 (2010) 6961–6978.
[95] H. Luo, Y. Xia, S. Spiegel, R. Nourgaliev, Z. Jiang, A reconstructed discontinuous Galerkin method based on a hierarchical WENO reconstruction for compressible flows on tetrahedral grids, J. Comput. Phys. 236 (2013) 477–492.
[96] A.N. Malyshev, E.I. Romenski, Hyperbolic equations for heat transfer. Global solvability of the Cauchy problem, Sib. Math. J. 27 (5) (1986) 734–740.
[97] G. Dal Maso, P.G. LeFloch, F. Murat, Definition and weak stability of nonconservative products, J. Math. Pures Appl. 74 (1995) 483–548.
[98] A. Meister, S. Ortleb, A positivity preserving and well-balanced DG scheme using finite volume subcells in almost dry regions, Appl. Math. Comput. 272 (2016) 259–273.
[99] G.I. Montecinos, L.O. Müller, E.F. Toro, Hyperbolic reformulation of a 1D viscoelastic blood flow model and ADER finite volume schemes, J. Comput. Phys. 266 (2014) 101–123.
[100] G.I. Montecinos, E.F. Toro, Reformulations for general advection–diffusion–reaction equations and locally implicit ADER schemes, J. Comput. Phys. 275 (2014) 415–442.
[101] B. Müller, High order numerical simulation of aeolian tones, Comput. Fluids 37 (2008) 450–462.
[102] L.O. Müller, C. Parés, E.F. Toro, Well-balanced high-order numerical schemes for one-dimensional blood flow in vessels with varying mechanical properties, J. Comput. Phys. 242 (2013) 53–85.
[103] L.O. Müller, E.F. Toro, Well-balanced high-order solver for blood flow in networks of vessels with variable properties, Int. J. Numer. Methods Biomed. Eng. 29 (12) (2013) 1388–1411.

[104] A. Muracchini, T. Ruggeri, L. Seccia, Dispersion relation in the high frequency limit and non linear wave stability for hyperbolic dissipative systems, Wave Motion 15 (2) (1992) 143–158.
[105] S. Ndanou, N. Favrie, S. Gavrilyuk, Criterion of hyperbolicity in hyperelasticity in the case of the stored energy in separable form, J. Elast. 115 (1) (2014) 1–25.
[106] H. Nishikawa, A first-order system approach for diffusion equation. I: second-order residual-distribution schemes, J. Comput. Phys. 227 (1) (2007) 315–352.
[107] H. Nishikawa, A first-order system approach for diffusion equation. II: unification of advection and diffusion, J. Comput. Phys. 229 (11) (2010) 3989–4016.
[108] C. Parés, Numerical methods for nonconservative hyperbolic systems: a theoretical framework, SIAM J. Numer. Anal. 44 (2006) 300–321.
[109] I. Peshkov, M. Grmela, E. Romenski, Irreversible mechanics and thermodynamics of two-phase continua experiencing stress-induced solid–fluid transitions, Contin. Mech. Thermodyn. 27 (6) (November 2015) 905–940.
[110] I. Peshkov, E. Romenski, A hyperbolic model for viscous Newtonian flows, Contin. Mech. Thermodyn. 28 (2016) 85–104, http://dx.doi.org/10.1007/s00161-014-0401-6.
[111] L. Prandtl, Über Flüssigkeitsbewegung bei sehr kleiner Reibung, in: Verhandlg. III. Intern. Math. Kongr., Heidelberg, 1904, pp. 484–491.
[112] J. Qiu, M. Dumbser, C.W. Shu, The discontinuous Galerkin method with Lax–Wendroff type time discretizations, Comput. Methods Appl. Mech. Eng. 194 (2005) 4528–4543.
[113] S. Rhebergen, O. Bokhove, J.J.W. van der Vegt, Discontinuous Galerkin finite element methods for hyperbolic nonconservative partial differential equations, J. Comput. Phys. 227 (2008) 1887–1922.
[114] E. Romenski, D. Drikakis, E. Toro, Conservative models and numerical methods for compressible two-phase flow, J. Sci. Comput. 42 (1) (2010) 68–95.
[115] E. Romenski, A.D. Resnyansky, E.F. Toro, Conservative hyperbolic model for compressible two-phase flow with different phase pressures and temperatures, Q. Appl. Math. 65 (2) (2007) 259–279.
[116] E.I. Romenski, Hyperbolic equations of maxwell's nonlinear model of elastoplastic heat-conducting media, Sib. Math. J. 30 (4) (1989) 606–625.
[117] E.I. Romenski, Hyperbolic systems of thermodynamically compatible conservation laws in continuum mechanics, Math. Comput. Model. 28 (10) (1998) 115–130.
[118] E.I. Romenski, Thermodynamics and hyperbolic systems of balance laws in continuum mechanics, in: E.F. Toro (Ed.), Godunov Methods, Springer, 2001, pp. 745–761.
[119] V.V. Rusanov, Calculation of interaction of non-steady shock waves with obstacles, J. Comput. Math. Phys. USSR 1 (1961) 267–279.
[120] Z. Xin, S. Jin, The relaxation schemes for systems of conservation laws in arbitrary space dimensions, Commun. Pure Appl. Math. 48 (1995) 235–277.
[121] H. Schlichting, K. Gersten, Grenzschichttheorie, Springer Verlag, 2005.
[122] T. Schwartzkopff, C.D. Munz, E.F. Toro, ADER: a high order approach for linear hyperbolic systems in 2d, J. Sci. Comput. 17 (1–4) (2002) 231–240.
[123] D. Sette, A. Busala, J.C. Hubbard, Energy transfer by collisions in vapors of chlorinated methanes, J. Chem. Phys. 23 (1955) 787–793.
[124] C.W. Shu, W.S. Don, D. Gottlieb, O. Schilling, L. Jameson, Numerical convergence study of nearly incompressible, inviscid Taylor–Green vortex flow, J. Sci. Comput. 24 (2005) 1–27.
[125] M. Sonntag, C.D. Munz, Shock capturing for discontinuous Galerkin methods using finite volume subcells, in: J. Fuhrmann, M. Ohlberger, C. Rohde (Eds.), Finite Volumes for Complex Applications VII, Springer, 2014, pp. 945–953.
[126] A.H. Stroud, Approximate Calculation of Multiple Integrals, Prentice–Hall Inc., Englewood Cliffs, New Jersey, 1971.
[127] A. Taube, M. Dumbser, D. Balsara, C.D. Munz, Arbitrary high order discontinuous Galerkin schemes for the magnetohydrodynamic equations, J. Sci. Comput. 30 (2007) 441–464.
[128] M. Tavelli, M. Dumbser, A staggered semi-implicit discontinuous Galerkin method for the two dimensional incompressible Navier–Stokes equations, Appl. Math. Comput. 248 (2014) 70–92.
[129] M. Tavelli, M. Dumbser, A staggered space–time discontinuous Galerkin method for the incompressible Navier–Stokes equations on two-dimensional triangular meshes, Comput. Fluids 119 (2015) 235–249.
[130] V.A. Titarev, E.I. Romenski, E.F. Toro, MUSTA-type upwind fluxes for non-linear elasticity, Int. J. Numer. Methods Eng. 73 (2008) 897–926.
[131] V.A. Titarev, E.F. Toro, ADER: arbitrary high order Godunov approach, J. Sci. Comput. 17 (1–4) (December 2002) 609–618.
[132] V.A. Titarev, E.F. Toro, ADER schemes for three-dimensional nonlinear hyperbolic systems, J. Comput. Phys. 204 (2005) 715–736.
[133] V.A. Titarev, P. Tsoutsanis, D. Drikakis, WENO schemes for mixed-element unstructured meshes, Commun. Comput. Phys. 8 (2010) 585–609.
[134] E.F. Toro, V.A. Titarev, Derivative Riemann solvers for systems of conservation laws and ADER methods, J. Comput. Phys. 212 (1) (2006) 150–165.
[135] E.F. Toro, Riemann Solvers and Numerical Methods for Fluid Dynamics, third edition, Springer, 2009.
[136] E.F. Toro, A. Hidalgo, ADER finite volume schemes for nonlinear reaction–diffusion equations, Appl. Numer. Math. 59 (2009) 73–100.
[137] E.F. Toro, R.C. Millington, L.A.M. Nejad, Towards very high order Godunov schemes, in: E.F. Toro (Ed.), Godunov Methods. Theory and Applications, Kluwer/Plenum Academic Publishers, 2001, pp. 905–938.
[138] E.F. Toro, G.I. Montecinos, Advection–diffusion–reaction equations: hyperbolization and high-order ADER discretizations, SIAM J. Sci. Comput. 36 (5) (2014) A2423–A2457.
[139] E.F. Toro, G.I. Montecinos, Implicit, semi-analytical solution of the generalized Riemann problem for stiff hyperbolic balance laws, J. Comput. Phys. 303 (2015) 146–172.
[140] E.F. Toro, V.A. Titarev, Solution of the generalized Riemann problem for advection–reaction equations, in: Proc. Roy. Soc. London, 2002, pp. 271–281.
[141] P. Tsoutsanis, V.A. Titarev, D. Drikakis, WENO schemes on arbitrary mixed-element unstructured meshes in three space dimensions, J. Comput. Phys. 230 (2011) 1585–1601.
[142] Duane C. Wallace, Statistical mechanics of monatomic liquids, Phys. Rev. E 56 (4) (1997) 4179.
[143] P. Woodward, P. Colella, The numerical simulation of two-dimensional fluid flow with strong shocks, J. Comput. Phys. 54 (1984) 115–173.
[144] J. Yan, C.W. Shu, A local discontinuous Galerkin method for KdV-type equations, SIAM J. Numer. Anal. 40 (2002) 769–791.
[145] J. Yan, C.W. Shu, Local discontinuous Galerkin methods for partial differential equations with higher order derivatives, J. Sci. Comput. 17 (1–4) (2002) 27–47.
[146] O. Zanotti, M. Dumbser, A high order special relativistic hydrodynamic and magnetohydrodynamic code with space–time adaptive mesh refinement, Comput. Phys. Commun. 188 (2015) 110–127.
[147] O. Zanotti, M. Dumbser, Efficient conservative ADER schemes based on WENO reconstruction and space–time predictor in primitive variables, Comput. Astrophys. Cosmol. 3 (2016) 1–32.
[148] O. Zanotti, F. Fambri, M. Dumbser, Solving the relativistic magnetohydrodynamics equations with ADER discontinuous Galerkin methods, a posteriori subcell limiting and adaptive mesh refinement, Mon. Not. R. Astron. Soc. 452 (2015) 3010–3029.
[149] O. Zanotti, F. Fambri, M. Dumbser, A. Hidalgo, Space–time adaptive ADER discontinuous Galerkin finite element schemes with a posteriori subcell finite volume limiting, Comput. Fluids 118 (2015) 204–224.